

Theoretical Study of Pulled Polymer Loops as a Model for Fission Yeast Chromosome

DISSERTATION

zur Erlangung des akademischen Grades

Doctor rerum naturalium
(Dr. rer. nat.)

vorgelegt

der Fakultät Mathematik und Naturwissenschaften
der Technischen Universität Dresden

von

Wenwen Huang

geboren am 16. September 1987 in China



MAX-PLANCK-INSTITUT FÜR PHYSIK KOMPLEXER SYSTEME

Dresden, 2017

Eingereicht am 29. September 2017.
Verteidigt am 17. January 2018.

1. Gutachter: Prof. Dr. Frank Jülicher
2. Gutachter: Associate Prof. Dr. Nenad Pavin

This thesis is dedicated to my loving daughter Xin Huang and wife Qiuxia Cai.

Acknowledgments

First of all, I would like to thank my supervisor Vasily Zaburdeav and Frank Jülicher for offering me the opportunity to work as a Ph.D. student in MPI-PKS. I thank them for the guidance along my whole Ph.D. project. I was influenced by the prudent scientific attitude from both Frank and Vasily. Thank for the uncountable and invaluable advice during my Ph.D. study. Besides science, I also want to thank them for building up an enjoyable atmosphere for daily life in the MPI-PKS.

I would like to thank my cooperators who help me a lot during my Ph.D. project. Especially, I would like to thank Yen-Ting Lin, who worked with me since the beginning of the project. As a former postdoc in our group, he taught me many useful knowledge and skills. As a good friend, he shared me a lot of his experiences. There are so many joys working together with him. I also want to express my deep thanks to Daniela Froemberg and Jaeoh Shin, who directly cooperated with me on my Ph.D. project. I would like to thank Somrita Ray, she spent a lot of time to help me polish the language of this thesis. Thanks to Prof. Sergey Denisov who helped me to initialize the Brownian Dynamic simulations. Thanks to our experimental cooperators Mariola Chacón, Petrina Delivani and Iva Tolić in Max Planck Institute of Molecular Cell Biology and Genetics for proposing such an interesting biological problem and all the support from biological side. I also want to thank Yu Zhou, as a good friend and cooperator, we enjoyed all our time together in MPI-PKS. Thanks to all the other wonderful group members in Biophysics Division of MPI-PKS, Wolfram Poenisch, Lennart Hilbert, Hui-Shun Kuan, Christoph A. Weber, Jens Karschau, André Scholich, Marko Popović, Alexander Mietke et al. for all the fruitful discussions.

Finally, I would like to thank my families. Without their support, my study in MPI-PKS is not even possible to happen. Also, I want to thank all the Chinese colleges in MPI-PKS. The life of study abroad is enjoyable with them together.

Abstract

In this thesis, we study the physics of the pulled polymer loops motivated by a biological problem of chromosome alignment during meiosis in fission yeast. During prophase I of meiotic fission yeast, the chromosomes form a loop structure by binding their telomeres to the Spindle Pole Body (SPB). SPB nucleates the growth of microtubules in the cytoplasm. Molecular motors attached to the cell membrane can exert the force on the microtubules and thus pull the whole nucleus. The nucleus performs oscillatory motion from one to the other end of the elongated zygote cell. Experimental evidence suggests that these oscillations facilitate homologous chromosome alignment which is required for the gene recombination. Our goal is to understand the physical mechanism of this alignment. We thus propose a model of pulled polymer loops to represent the chromosomal motion during oscillations.

Using a freely-jointed bead-rod model for the pulled polymer loop, we solve the equilibrium statistics of the polymer configurations both in 1D and 3D. In 1D, we find a peculiar mapping of the bead-rod system to a system of particles on a lattice. Utilizing the wealth of tools of the particle system, we solve exactly the 1D stationary measure and map it back to the polymer system. To address the looping geometry, the Brownian Bridge technique is employed. The mean and variance of beads position along the loop are discussed in detail both in 1D and 3D. We then can calculate the three-dimensional statistics of the distance between corresponding beads from a pair of loops in order to discuss the pairing problem of homologous chromosomes. The steady-state shape of a three-dimensional pulled polymer loop is quantified using the descriptors based on the gyration tensor.

Beyond the steady state statistics, the relaxation dynamics of the pinned polymer loop in a constant external force field is discussed. In 1D we show the mapping of polymer dynamics to the well-known Asymmetric Simple Exclusion Process (ASEP) model. Our pinned polymer loop is mapped to a half filled ASEP with reflecting boundaries. We solve the ASEP model exactly by using the generalized Bethe ansatz method. Thus with the help of the ASEP theory, the relaxation time of the polymer problem can be calculated analytically. To test our theoretical predictions, extensive simulations are performed. We find that our theory of relaxation time fit very well to the relaxation time of a 3D polymer in the direction of the external force field.

Finally, we discuss the relevance of our findings to the problem of chromosome alignment in fission yeast.

Contents

1	Introduction	1
1.1	Nuclear oscillations in fission yeast	2
1.1.1	Fission yeast	2
1.1.2	Basis of meiosis	3
1.1.3	Nuclear oscillations	4
1.1.4	The role of nuclear oscillations for chromosome alignment	5
1.2	Polymer models and DNA	7
1.2.1	Models of chromosomal DNA	7
1.2.2	Polymer loop and pulled polymer	8
1.2.3	Equilibrium vs non-equilibrium	12
1.3	ASEP and Bethe ansatz	14
1.3.1	Brief introduction of ASEP	14
1.3.2	Bethe ansatz	16
1.4	Outline	17
1.4.1	Research goals	17
1.4.2	Overview of the thesis	17
2	Theoretical Model and Numerical Simulation Methods	19
2.1	Stochastic models of polymer loops	19
2.1.1	Coordinate transformation	19
2.1.2	Bead-rod model	21
2.1.3	Bead-spring model	24
2.2	Brownian Dynamics simulations	26
2.2.1	BD simulation of the bead-rod model	26
2.2.2	BD simulation of the bead-spring model	29
2.3	Monte Carlo simulation of the bead-rod model	30
2.4	Summary	32
3	Equilibrium Statistics of the Forced Pinned Polymer Loop	33
3.1	Pinned polymer loop in a constant force field	33
3.2	Pinned Polymer Loop in 1D	34
3.2.1	Mapping to a particle system on 1D lattice	34
3.2.2	Grand canonical ensemble solution	36
3.2.3	Canonical ensemble solution	41

3.3	Equilibrium statistics in 3D	45
3.3.1	Partition function	45
3.3.2	Mean and variance of the bead position	46
3.3.3	The pairing of loops	47
3.3.4	Intersecting loops	48
3.3.5	Excluded volume effect	51
3.4	Characterizing the shape of pinned polymer loops	53
3.4.1	The gyration tensor	54
3.4.2	Asphericity and the nature of asphericity	57
3.5	Summary	57
4	Relaxation Dynamics of the Forced Pinned Polymer Loop	61
4.1	Rouse theory of the pinned bead-spring loop	61
4.1.1	Dynamical equation	62
4.1.2	The normal modes	63
4.1.3	Relaxation time	65
4.1.4	Comparison to the bead-rod model	65
4.2	1D pinned bead-rod loop can be mapped to ASEP	67
4.2.1	The mapping to ASEP	67
4.2.2	Some numerical results	70
4.3	The Bethe ansatz solution of ASEP	72
4.3.1	Solution of single particle	73
4.3.2	Solution of two particles	76
4.3.3	Solution of general N particles	82
4.3.4	Relaxation time	86
4.4	Dynamics of 3D bead-rod polymer loop	89
4.4.1	Relaxation time of 3D pinned bead-rod loop	89
4.4.2	Stretch coil relaxation	92
4.5	Summary	94
5	Discussions and Outlook	95
5.1	Discussions	95
5.1.1	Chromosome paring and alignment	95
5.1.2	The blob theory of pulled polymer	97
5.2	Summary and outlook	99
	Appendices	101
A	An efficient algorithm to compute pseudo force of bead-rod loop	103
B	Monte Carlo simulation of 1D particle-lattice model	105
C	The Toeplitz matrix	107

D Derivation of the exclusion condition	109
E Bethe equations of the periodic ASEP	111
F Single-file diffusion with reflecting boundaries	113
G The blob theory of pinned polymer loop	119
Bibliography	123

Chapter 1

Introduction

Many biological processes can be described by classic models of statistical physics. For example, random walk models [1, 2] were applied to describe the transcription of mRNA [3–5] as well as the spatially distributed ecological systems [6–8]. The corresponding length scale spreads from microns to kilometers. Analysis of these idealized models provides important insights on the governing mechanism in the respective biological processes. This thesis is yet another example of application of statistical physics modeling to a fundamental biological process.

The segregation of chromosome pairs is a crucial process during cell division. Its malfunction is related to many diseases such as the Down Syndrome [9]. Dramatic chromosome movements during that stage, which has been observed across broadly divergent eukaryotic phyla from yeast to human, have been suggested to be important for the segregation [10, 11]. In addition, experimental evidence shows that chromosomes cannot segregate properly when the movements are inhibited [11, 12]. However, the exact role of these movements and the mechanism to ensure proper segregation is still ambiguous [10, 11].

This thesis focuses on modeling the motion of chromosomes in fission yeast during meiotic cell division [13–15]. In meiosis, two fission yeast cells merge to form a zygote cell with a “banana” shape [14] and then the nuclei of the two cells also merge together. During Prophase I of meiotic fission yeast, the nucleus, which contains three pairs of chromosomes, moves from one pole of the elongated zygote to the other. These oscillations last for about two hours [12]. The period of the oscillation is $\sim 10 - 15$ minutes [12]. The cell proceeds to division after the oscillations stop. It is believed that the oscillations are required for the alignment of homologous chromosomes which is required for proper gene recombination [12, 16, 17].

This thesis presents quantitative description of the chromosomal movements with the chromosomes represented by polymer models [18, 19]. The results we obtain from the model provide relevant information about the chromosome alignment as necessary for gene recombination [20].

In this chapter, we introduce the biological background and some previous related studies about modeling chromosomes as polymers. Our research goals and the overview of the thesis are given at the end of the chapter.

1.1 Nuclear oscillations in fission yeast

In this section, we introduce the biological basis of nuclear oscillations in fission yeast. We firstly introduce our model organism, fission yeast, followed by an overview of meiosis. Next, we go into the nuclear structure of fission yeast and the movements of chromosomes, specifically during meiosis, followed by the discussion about biological processes like chromosome alignment and recombination. In the last subsection, we discuss some experimental findings about the biological role of the nuclear oscillations.

1.1.1 Fission yeast

Fission yeast (*Schizosaccharomyces pombe*) is a model organism that is widely used in the study of molecular and cellular biology [21, 22]. It is a unicellular eukaryote and has a rod-like shape. The typical size of fission yeast is 3-4 micrometres in diameter and 7-14 micrometres in length [21, 22]. Fig. 1.1 presents a microscopic image of fission yeast cells.

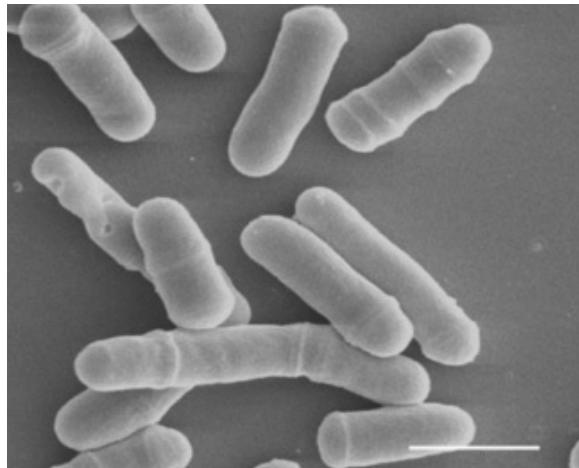


Figure 1.1: Microscopic view of a fission yeast culture. The scalar bar indicates 10 μm . Image reprinted from [23] with permission.

Fission yeast is widely used in traditional brewing and baking. It was first discovered in 1893 in the sediment of millet beer [22]. As a single-celled fungus, fission yeast has a simple genome with three chromosomes [24]. The genome of fission yeast is fully sequenced and the three chromosomes contain about 14Mb of DNA [25]. With a rapid growth rate and plenty of mutants, fission yeast has become a model organism for genetic studies [24].

Fission yeast is normally a haploid cell [23, 26]. The growth of the fission yeast begins with the elongation at the ends. After mitosis, division occurs by the formation a cell plate that cleaves the cell at its midpoint [21]. However, when put under stressful

conditions, such as nitrogen deficiency, two cells can conjugate to form a diploid and then form four spores via meiosis [26]. This is observed experimentally and this stage is exactly when the interesting nuclear oscillations happen [13]. In the next subsection, some basis of the meiosis in fission yeast are explained.

1.1.2 Basis of meiosis

Meiosis is a process of cell division that reduces the number of chromosomes in the parent cell by half and produces four genetically distinct gamete cells. This process occurs in all the sexually reproducing organisms, including human [23, 27].

Meiosis begins with a parent cell with two copies of each chromosome, followed by two rounds of cell divisions which produce four potential daughter cells, each has half number of chromosomes as their parent cell [27]. The two rounds of cell division are called *Meiosis I* and *Meiosis II*, respectively [27]. It is during Meiosis I that the pair of chromosomes, one from the father and the other from the mother, separates into two offspring cells [27]. Meiosis II is very similar to the mitosis where two sister chromatins contained in one chromosome separate [27, 28]. Fig. 1.2 illustrates an overview of the meiosis process.

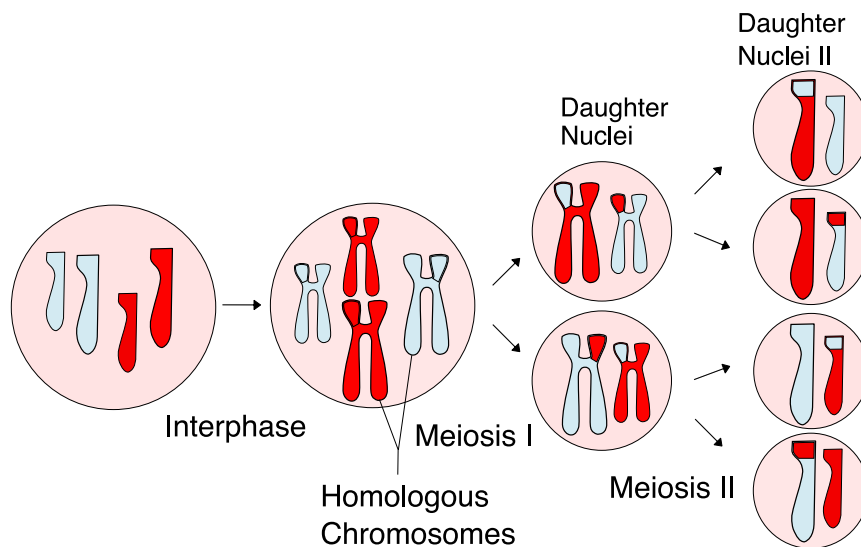


Figure 1.2: Overview of meiosis and an illustration of recombination between homologous chromosomes resulting in four unique daughter cells. Image reprinted from [29] with permission.

As in mitosis, each round of cell division can be divided in prophase, metaphase, anaphase, and telophase [27]. We elaborate Meiosis I in details, especially the Prophase I when the nuclear oscillations take place. Fig. 1.3 shows the time-lapse snapshots of the oscillations.

- *Prophase I*: prophase I is an important stage when many processes happen. Two of the examples are bouquet formation [30] and homologous recombination [17, 31], both occurring in generic organisms. In the early state of Prophase, chromosomes are reorganized spatially [13, 30, 32]. Usually, the telomeres, protein complexes at chromosome ends, are clustered and attached to a small region of the nuclear membrane, forming a bouquet structure. This is called bouquet formation or telomere clustering [32]. Fig 1.4 shows an example of fission yeast during Prophase I. In the process of recombination, the homologous chromosomes, which are paternal and maternal pairs, align and exchange parts of their DNA and usually result in the chromosomal crossover [27]. Homologous recombination is critical for pairing and accurate segregation of the chromosomes in the later stage of Meiosis I and also plays an important role for genetic diversity in nature [23, 27]. More interestingly, this stage is the exact period when the nuclear oscillations happen in fission yeast [33, 34]. We explain this part in the next subsection.

- *Metaphase I*: at this stage, homologous pairs move together along the middle plate, and the microtubules from centrosomes attach to their respective chromosomes, the paired homologous chromosomes align along an equatorial plane that bisects the spindle [27]. However, in fission yeast, the centromere is replaced by a functional equivalent organelle called Spindle Pole Body (SPB) [31].

- *Anaphase I*: at this stage, the microtubules shorten, pulling homologous chromosomes to opposite poles. Notice here, chromosomes still consist of a pair of sister chromatids. The cell body elongates, preparing for cell division [27].

- *Telophase I*: at the last stage of Meiosis I, chromosomes arrive at the poles. The microtubules network of spindle disappears. New nuclear membrane appears. The two daughter cells now only have half the number of chromosomes [27].

After Meiosis I, Meiosis II occurs without DNA replication in between [23, 27]. The process is similar to Meiosis I except the sister chromatids segregate instead of homologous chromosomes [27]. Four unique daughter cells are formed after the completion of Meiosis.

1.1.3 Nuclear oscillations

As mentioned in the previous subsection, nuclear oscillations take place during prophase I of meiosis, and so as the important processes of homologous chromosomes alignment and recombination [33]. Because of the peculiar nuclear shape during this stage, nuclear oscillations are also often mentioned as *horse-tail* movements [10, 31, 34]. Fig. 1.3 shows a time-lapse sequence of the nuclear oscillations.

The looping structure of chromosomes

Before the nuclear oscillations, chromosomes are reorganized and the bouquet formation happens [23, 27]. In fission yeast, the SPB is anchored in the nuclear envelope,

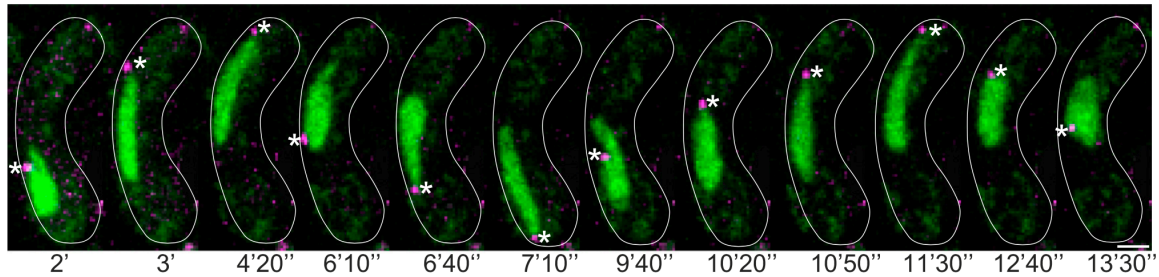


Figure 1.3: Time-lapse experiments of nuclear oscillations in fission yeast, DNA marker in green (Rec8-GFP) and SPB marker in magenta (Sid4-mCherry) also indicated by asterisk. Reprinted from [11] with permission.

telomeres of chromosomes are clustered to the SPB region of the inner nuclear membrane [28, 30]. The chromosomes are condensed to be the rod-like chain. There are two sister chromatins contained in one chromosome [28]. With all the telomeres bond to the SPB, chromosomes form the loop structure [35], illustrated in Fig. 1.4.

Redistribution of dynein motors drives the nuclear oscillations

While the inner side of SPB bonds the chromosome telomeres, the outer side is attached to the microtubules in the cytoplasm [12, 14]. During the oscillation, dynein motors generate the force [14]. As one motor is not enough for the oscillation, the collective behavior of motors is observed to drive the nucleus motion [14]. The spatial distribution of motor molecules varies during the oscillation. Motors accumulate in the side of fission yeast that the nucleus moves toward to. It was found that the dynein pulling force is the main contribution that drives the oscillation [14]. Fig. 1.5 shows the redistribution of dynein motors during the oscillation.

Related biological parameters of nuclear oscillations

For construction of the quantitative model, we found the values of most relevant parameters in the available experimental literature. These parameters are summarized in table 1.1.

1.1.4 The role of nuclear oscillations for chromosome alignment

Although the nuclear oscillations in fission yeast can be observed clearly in the experiments, the biological role of it is not thoroughly understood. One intuitive hypothesis is that the movement facilitates the pairing of homologous chromosomes [12, 37]. However, Koszul et al. proposed that the chromosome movement might play other roles than pairing, such as to resolve homologous entanglements or non-homologous connections [10]. Also, Chacón et al. stated a dual role for the nuclear oscillations, promoting

Meiotic prophase

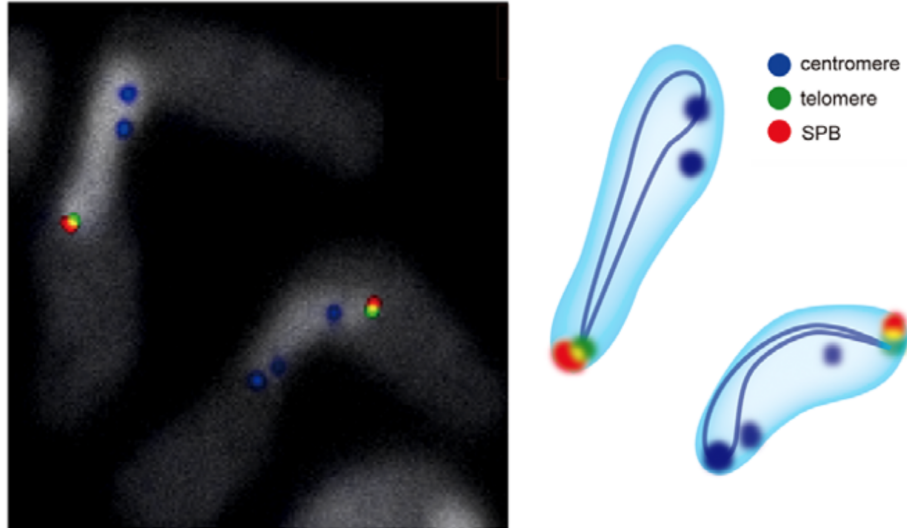


Figure 1.4: The meiotic prophase I of fission yeast. Telomeres are clustered to form a bouquet structure. Location of centromeres and telomeres is determined by FISH analysis [35] using specific probes. The SPB is detected by indirect immunofluorescence. Right figures are schematic models of spatial organization of the nucleus. Image modified and reprinted from [35] with permission.

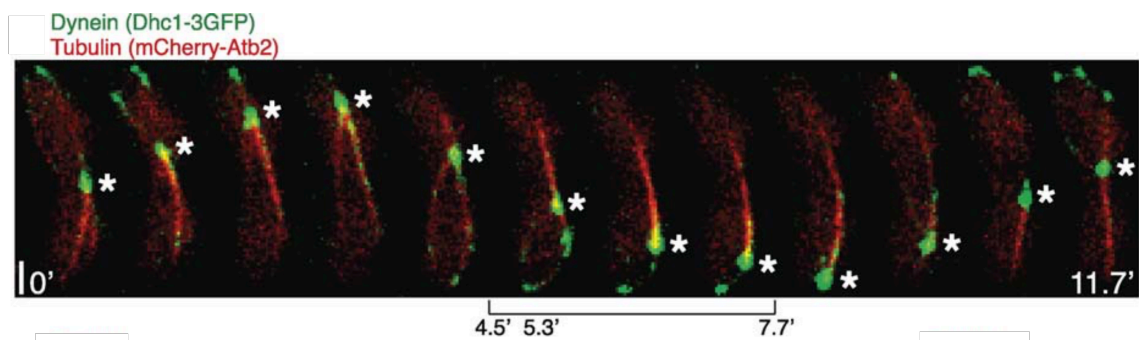


Figure 1.5: Distribution of dynein motors during nuclear oscillations. Dyneins are labeled as green and tubulins are labeled as red. The position of SPB is indicated by asterisk. Time point scales in minutes. Image reprinted from [14] with permission.

Table 1.1: Parameters of fission yeast during meiosis

Parameter	Value
Typical size of the nucleus	$3\mu\text{m}$ [14, 36]
Number of chromosomes	Three pairs [14, 36]
Compaction ratio of the chromatin	10^2bp/nm [36]
Kuhn length of the chromatin	$200 \sim 300\text{nm}$ [37, 38]
Duration of the nuclear oscillations	~ 2 hours [14]
Period of the nuclear oscillations	~ 10 min [14]
Moving speed of the nucleus	$2.5\mu\text{m/min}$ [14]
Viscosity of the nucleoplasm	$\sim 1000 \times \mu_{\text{water}}$ [39, 40]
Length of Chromosome I	5.58 Mb [25]
Length of Chromosome II	4.54 Mb [25]
Length of Chromosome III	2.45 Mb [25]

initial pairing and restricting the time of chromosome associations to ensure proper segregation [11].

Experimental evidence suggests the nuclear oscillations plays an important role for the chromosome alignment [10, 11]. However, it seems that there is no study using the mathematical modelling to test the hypothesis that is otherwise not possible to do in the experiments. One of the aims of this thesis is to propose a quantitative model for this specific problem in fission yeast. By studying the statistical and dynamical details of the model, the machinery of chromosome pairing and the role of chromosome movements can be understood in a more quantitative way.

1.2 Polymer models and DNA

In this section, we briefly introduce the theoretical models used to quantify the DNA. These models are characterized by beads connected by rods or springs, which composes a significant portion of models in polymer physics. More specifically, we discuss the model we used for the chromosomal DNA during nuclear oscillations and summarize previous works of applying the polymer models to the chromosomal DNA [41–44]. The theoretical models about looped polymer and pulled polymer are discussed. Finally, we discuss the conditions that allow us to use the equilibrium setting to study the intrinsically non-equilibrium biological polymer problems.

1.2.1 Models of chromosomal DNA

To quantitatively describe the chromosome, it is natural to view it as a polymer. In fact, there are already many examples in this direction [41–44]. However, depending on the scenario, different polymer models may apply.

In physics, a polymer model is described by beads connected by massless springs or rods [19, 45]. The interactions, usually characterized as different types of potentials, specify the setting of the model [19]. As our aim is to model the chromosome during nuclear oscillations in fission yeast, there are two major factors we need to take into account. First, the topology of the chromosome is a loop structure as shown in Fig. 1.4. Second, all chromosomes are bound to the SPB and pulled by an external force. Combining these biological facts and the experimental observations, like shown in Fig. 1.4, we propose a pulled polymer loop model for the chromosomes. Fig. 1.6 shows a sketch of the model. We leave the discussion of the model details to Chapter 2.

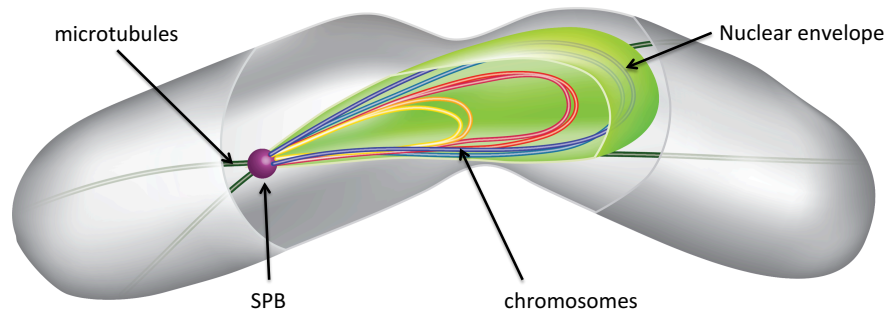


Figure 1.6: The sketch of pulled chromosomes in meiotic fission yeast. Three pairs of chromosomes with all ends bound to SPB (shown in magenta) in the nucleus are indicated by different colors. The SPB is pulled by multiple dynein motors (not shown) walking along microtubules (dark green). The SPB is anchored to the nuclear envelope (light green) and entrains the whole nucleus.

To the best of our knowledge, there are not many works which focus on both the looping geometry of the polymer and the polymer being pulled by an external force. In the following subsections, we discuss previous works related to this problem.

1.2.2 Polymer loop and pulled polymer

Polymer loop

Polymers forming a loop structure are ubiquitous in chemistry and biology [43, 46]. The study of ring polymer dates back to the years when polymer physics was first established [47, 48]. Kramers developed an equilibrium theory of macromolecules that possesses branch points and rings of the dilute polymer solution in 1946 [47]. Zimm calculated the statistics of mean square radii of molecules containing branches and rings in 1949 [48]. However, comparing to the simplest polymer chain model, research focus on polymer loop are far less than the former. We review here some interesting and most relevant results.

Since Kramers and Zimm, there is a number of works trying to study the static and dynamical properties of the ring polymer from the theoretical point of view. In 1965,

Casassa derived some statistical properties of flexible ring polymers, including mean square radius, the second Virial coefficient and angular distribution of scattering [49]. In 1980, Burchard and Schmidt calculated the static and dynamical structure factors of flexible ring polymers [50]. Baumgärtner considered the self-avoiding effect of ring polymers in 1984 and found that the asymptotic scaling exponents of gyration radius and structure function are the same as linear polymers [51]. In 1986, Cates et al. studied the non-concatenated ring polymer melt and found the size of polymer R scaled with the polymerization index N as $R \sim N^{2/5}$ and the diffusion constant D scaled as $D \sim N^{-2}$ [52]. In 1994, Obukhov et al. considered the dynamics of a ring polymer in a gel and obtained the diffusion coefficient to scale with the molecular weight M as $D \sim M^{-2}$ and the longest relaxation time T as $T \sim M^{5/2}$ [53]. Carl investigated the configurational and rheological properties of multiple-twisted ring polymers using a long cyclic finitely extensible bead-spring model in 1995 [54]. He also presented a study on bead-spring chains in steady flows, various properties such as the power spectrum, the autocorrelation functions of configurational quantities were discussed in [55]. In 2001, Panyukov and Rabin studied the effects of thermal fluctuations on elastic rings. Analytical expressions were derived for correlation function of Euler angles, mean-square distance between points on the ring contour, radius of gyration, and probability distribution of writhe fluctuations [56]. Mukherji et al. studied a polymer ring or chain diffusing near attractive surfaces. They found the diffusion constant scaling as $D \sim N^{-3/2}$ for a linear chain and solid strong adsorbing surfaces, and $D \sim N^{-1}$ for a ring polymer and soft surfaces [57]. Sakaue proposed a simple mean-field theory for the structure of ring polymer melts which takes into account the many-body effects [58, 59]. In 2012, Kim et al. presented a self-consistent field theory formalism of topologically unconstrained ring polymers [60]. In 2013, Reigh performed lattice Monte Carlo simulations to investigate the dependence of ring polymer conformation to the concentration, where the scaling of gyration radius R_g with the concentration ϕ that $R_g \sim \phi^{-0.59}$ was found [61]. In 2014, Lang et al. studied the tumbling dynamics of semiflexible ring polymers as a model of the cytoskeletal filament in a shear flow. They found the tumbling frequency f_c to scale with the Weissenberg number Wi as $f_c \sim Wi^{3/4}$ in contrast to the prediction of the classical theory of both flexible polymers and rigid rods that $f_c \sim Wi^{2/3}$ [62].

A looped polymer with high concentration, like polymer melts, are often used in modeling interphase chromosomes. Interestingly, it is found that during interphase, the spatial organization of the multiple chromosomes in the nucleus is neither homogeneous nor well mixed. Instead, each chromosome forms its own “territory” [43]. Many interesting works can be found discussing this problem. For example, in 2008, Rosa and Everaers used the simulation results of polymer rings to explain the existence and stability of territories of interphase chromosomes in yeast, *Drosophila*, and human [63]. In general, the computation power required to simulate the whole genome is huge, they also developed an efficient multiscale numerical approach to study the conformational statistics of ring polymers melts [64]. Dorier employed a very simple

non-permeable freely jointed polymer model and recovered the chromosomal territories in crowded nuclei [65]. This part of work is nicely reviewed in Ref. [43].

It is possible that looping structures of the polymer are formed temporarily in chromosomes. This could be caused by the DNA replication process or binding proteins connecting two loci of chromosomes. In 1995, Sachs used a looping random walk model to study the interphase chromosomes and compared the results with the fluorescence labeled data, showing that “giant” loops as large as 3 Mbp can be formed [66]. Marko considered a model of two polymer loops tethered together and its application to chromosome segregation [67]. The looping probabilities of interphase chromosomes were also discussed in Ref. [68]. In 2011, Zhang et al. modeled the mitotic chromosomes as polymers that could form internal loops by binding proteins. They found the loops play an important role in the mechanical properties of the polymer [69]. Wong set up a polymer model and used it to predict the whole nuclear architecture of fission yeast [70]. Dekker and Giorgetti employed the computational polymer model to explain the 3C/HiC data [71, 72]. In 2014, Youngren employed thermodynamic ring polymer model to study the duplication and segregation of *E. coli* chromosomes, the chromosome organization and structure dynamics were explained in Ref. [73].

The confinement such as the nuclear membrane or cell wall could also play an important role in chromosome dynamics. One of the examples is Fritsche’s work in 2011, where they studied the influence of confinement on the spatial organization of semiflexible ring polymers [74]. They found the elongated confinement induced a pronounced ordering with respect to the long axis while the spherical confinement induced no such preferred orientational axis. The studies of the polymers (including chains and rings) under confinements were reviewed by Ha et al. in [75].

There is also many experimental work related to polymer loops. In 1992, Tead et al. used polystyrene molecules to compare the diffusion of linear and ring polymers and found the diffusion coefficients of deuterated linear chains in ring matrices were nearly identical to those in linear chain matrices [76]. Kapnistos et al. found the stress relaxation of entangled ring polymer follows a power-law, see Ref. [77]. Structure and dynamics of polymer loops by neutron scattering were studied by Brás et al. in [78] where it was found that the Rouse model was violated by the fast diffusion. Witz et al. employed the atomic force microscopy to study 2D circular DNA and confirmed that the topologically invariant exponent $\nu = 3/4$, where the gyration radius $R_g \sim L^{2\nu}$ [79, 80]. Gooßen et al. studied dynamics of polymer loops using neutron spin echo spectroscopy which allows one to observe the space-time evolution of segmental motion [81, 82].

Besides what we have mentioned above, the shape of ring polymers is studied in [83–86]. Also, there are a series of works considering the ring polymer with entanglements and topological knots [87–95]. Thus, the investigation of polymer loops is quite intensive and draws the attention of many researchers nowadays.

Pulled polymer

As we mentioned above, in order to model the nuclear oscillations of fission yeast, we have to consider the pulling dynamics. After the change of coordinate system to the one co-moving with the SPB (see Section 2.1), a pulled polymer can be mapped to a pinned polymer in an external force field. In this section, we review some previous works in this direction. Most of them are about pulled polymer chain. Nevertheless, we think it is still helpful to know what have been done about pulled polymers or tethered polymers in an external field.

A polymer chain with one end free and the other end pulled by an external force was discussed by de Gennes, he found that the internal friction was negligible for a polymer chain with large monomer number [18]. Pincus considered the pulled polymer as a sequence of independent “blobs”, and calculated the extension of the pulled polymer [96, 97]. Brochard-Wyart further developed the “trumpet” and the “stem-flower” pictures of pulled polymer chain [98–101]. When the pulling force is not too strong, the polymer can be presented as a series of independent blobs with increasing size, i.e. the portion of polymer near to the free end fluctuates more. As the pulling force further increases to a strong force regime, the polymer portion near to the fixed end is completely stretched, forming a “stem-flower” like picture, see Fig. 1.7. Using fluorescence microscopy and optical tweezers, Perkins et al. performed the pulling experiments on single DNA molecule and measured the relaxation time of the polymer during the stretch-coil transition [102, 104]. They obtained the relaxation time τ scaling with the polymer contour length L as $\tau \sim L^{1.66}$ [104]. Wirtz measured transport properties of a single DNA molecule in [105] and found results consistent with the blob theory.

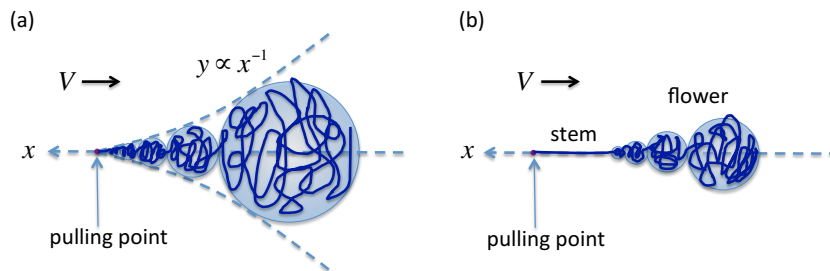


Figure 1.7: Illustration of “stem-flower” picture for pulled polymer chain. (a) Trumpet picture at moderate pulling force; (b) Stem-flower picture at strong pulling force.

Rzehak et al. considered pinned polymer in a uniform flow with hydrodynamic interaction and found neither the free-draining nor the non-draining models can describe

the polymer-flow interaction appropriately, so an f-shell blob model was proposed to describe the partial draining situation [106]. Larson et al. performed Brownian Dynamics simulation for a DNA in an external flow field and found the unraveling processes were consistent with the experimental findings [107]. In 2000, Doyle measured the cyclic and stretching dynamics of a tethered DNA molecule in the shear flow and found temporal fluctuations could be enhanced by the shear flow [108, 109]. Sebastian studied theoretically the dynamics of pulling a polymer chain out of a potential well and found that the time t_{po} required to pull out a polymer of N segments scales as $t_{po} \sim N^2$ [110]. Cui performed the stretching and releasing experiment by pulling a single chicken erythrocyte chromatin fiber with the optical tweezers, where the persistence length of 30 nm and a stretch modulus of 5 pN are calculated [111]. Rzehak found that the blob theory can describe the conformation fluctuation and relaxation of a tethered polymer in uniform flow only when the finite extensibility of the polymer was unimportant [112]. In 2007, Mohan et al. employed Rouse theory to study the unraveling dynamics of tethered semiflexible polymer in uniform solvent flow whereas a convective mechanism of tension propagation in wormlike chains under conditions of strong flow was demonstrated [113]. Sing et al. studied flexible and semiflexible tethered polymers in the limit of high shear flows and consequently near-full extension of the chains and observed an universal “tether kink” geometry that is independent of the shear rates [114]. Sakaue et al. studied the conformation and dynamics of a single flexible polymer chain that is pulled by a constant force applied at its one end. The generalized dynamical equations describing the extension and friction laws in steady-state were elucidated and the propagation of tension in the transient process were discussed [115]. Varghese et al. derived the force fluctuations relation in stretching a tethered polymer [116]. In 2013, Dai and Doyle found in [117] that the scenario of a pulled polymer is very similar to a polymer confined in a cylinder with proper radius.

To the best of our knowledge, the discussion of pulled polymer loops is missing except for our own work [20]. So we have reviewed here two classes of works: the works on polymer loops and that on pulled polymers. In next subsection, we discuss the equilibrium and non-equilibrium situations of a pulled polymer loop.

1.2.3 Equilibrium vs non-equilibrium

Usually, a system of pulled polymer in solution is referred as a non-equilibrium system [18, 19]. However, the equilibrium statistics can be applied under certain conditions. As it is usually easier to derive the equilibrium theory, these conditions are discussed in this subsection.

In prophase I of meiotic fission yeast, chromosomes oscillate in the cell [14]. Here, we simplify the picture of one oscillation period to two pieces of steady pulling motion with opposite moving direction. Experimental evidence suggested that the moving velocity of SPB during nuclear oscillations is nearly constant when moving in one direction, as shown in Fig. 1.8 [14]. We do not consider the turning process of the oscillations and

only discuss chromosomes pulled with a constant velocity in one direction.

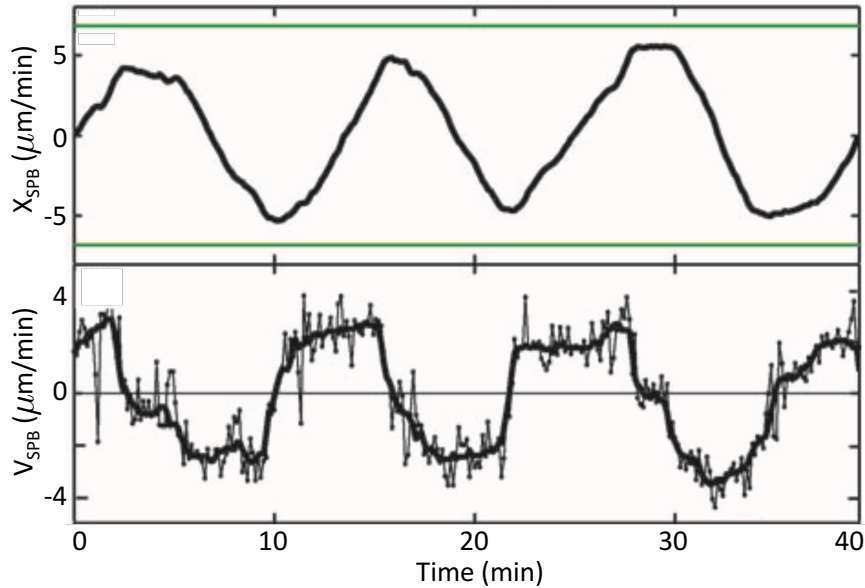


Figure 1.8: Experimental trajectory and velocity of the SPB measured by fluorescence microscopy. The upper panel shows the trajectory of the SPB along the cell main axis. The green line is the boundary of the cell. The lower panel shows the corresponding velocity of the SPB. Image reprinted and modified from [14] with permission.

Steadily pulled chromosomes in solution still cannot be classified as an equilibrium system. One reason is the active processes in the biological environment [118]. Various proteins are involved in the nuclear oscillations [14]. Moreover, the thermal fluctuations are important in the length scale of the chromosomes (several microns) [14, 19]. However, we assume all these activities together with the thermal fluctuations can be represented by an effective temperature of the system. It means that a homogeneous fluctuating environment is assumed, although the effective temperature could be different from the real laboratory temperature. This is a key assumption that allows us to apply the equilibrium theory on the system.

In order to apply the equilibrium theory of the pulled polymer loops, additional assumptions should be made. We ignore the hydrodynamic interactions between monomers can in our model. In other words, the system is a free-draining system [18, 19]. With all these assumptions mentioned above, the equilibrium statistics of pulled polymer loops can be applied to the chromosome movements in fission yeast.

In physics, the criterion to classify a system as equilibrium or non-equilibrium system is whether the detailed balance is satisfied or not [119, 120]. Non-equilibrium

system in stationary state violates the detailed balance, but there exists an invariant probability measure of the system. The moving chromosomes under assumptions can be considered as an equilibrium system, which means the detailed balance is fulfilled. However, the dynamics of the system can be discussed in the situation of the system approaching equilibrium. An example of non-equilibrium system breaking the detailed balance is the Asymmetric Simple Exclusion Process (ASEP) with open or periodic boundaries. Interestingly, we found a peculiar mapping from the pulled polymer loop model to ASEP system with reflecting boundaries. The ASEP model is discussed in next section.

1.3 ASEP and Bethe ansatz

ASEP is a 1D lattice model with many particles hopping on the lattice. The number of particles sitting on one lattice site cannot be larger than one, which means the particles are exclusive to each other. Normally, the hopping rates of the particle to right and left are not the same, which brings asymmetry. It is one of the simplest models for the systems out of equilibrium. In this thesis, we found a very peculiar mapping from the polymer dynamics to the ASEP model. With this mapping, using advanced tools such as Bethe ansatz, we can solve the problem of polymer dynamics. In this section, we briefly introduce the history of the ASEP model and the Bethe ansatz method we used to find the exact solution of the model.

1.3.1 Brief introduction of ASEP

ASEP model is said to be a minimal non-equilibrium model similar to the Ising model in equilibrium statistical physics [121, 122]. Interestingly, it was first proposed for the study of a biological problem. In 1968, MacDonald et al. proposed a mathematical model for the kinetics of protein synthesis by ribosomes, which is essentially the ASEP model [3]. However, the name of ASEP was introduced later in 1970 by Spitzer with the aim of rigorously deriving macroscopic hydrodynamic behavior from a microscopic model of particles [123]. This task was accomplished by Varadhan et al. on this specific simple model [124]. ASEP model has numerous applications besides those mentioned above. Other examples ranging from the motion of motor molecules along the microtubules to the traffic systems, see review [4, 125].

The simplest ASEP model is ASEP with periodic boundaries [122], see a schematic in Fig. 1.9 (a). The stationary measure of periodic ASEP is simply a uniform distribution. If the hopping rate is asymmetric, then a steady current can be induced in the stationary measure. This is one of the simplest examples where the detailed balance is not satisfied in the stationary state. The full dynamics in this case can be solved by the Bethe ansatz method [126], which we discuss later.

ASEP on an infinite line is also an interesting case [5, 127, 128]. For example, one

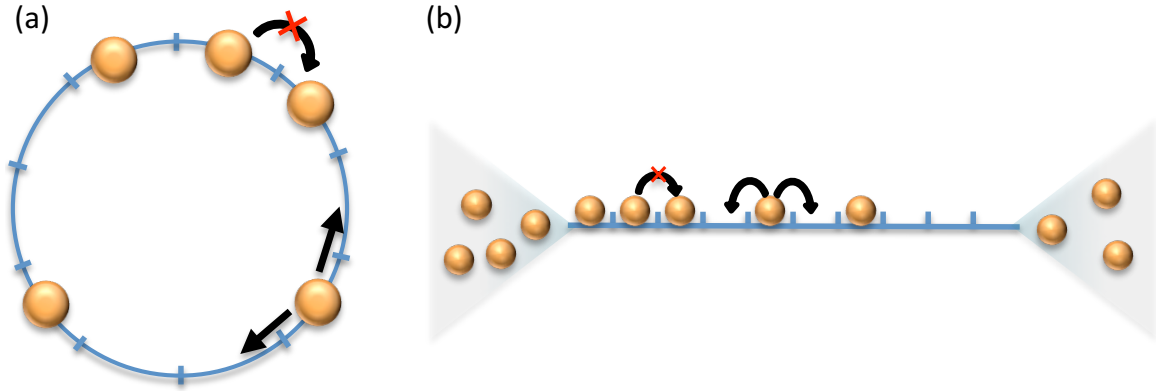


Figure 1.9: Schematics of ASEP model. (a) ASEP with periodic condition. (b) ASEP with open boundary condition.

can rigorously describe the diffusion of a tagged particle for the special case of the symmetric hopping rate:

$$\langle x^2 \rangle = 2 \frac{1-\rho}{\rho} \sqrt{\frac{t}{\pi}}, \quad (1.1)$$

where ρ is the density of particles. As we can see it is a sub-diffusion process with a mean squared displacement scaling $t^{1/2}$ as long as $\rho \neq 0$. The sub-diffusive behavior has been demonstrated in various experimental realizations [129–132].

ASEP with open boundaries is considered to be the minimal discrete microscopic model of transportation [122, 133], see Fig. 1.9 (b). In this model, the two ends of the lattice are connected to two different reservoirs. The rate of insertion and removal at the two ends are not the same in general. For instance, in the simplest case, particles can only be inserted at one end and removed at the other end. A current can be induced by the bias of hopping rates. In 1991, Krug et al. studied the ASEP with open boundaries and discovered the boundary induced phase transitions in the model [134]. Depending on the insertion or removal rates at the ends, the stationary state of the system can be in high density, low density or maximum current phase. The phase transition can occur by adjusting the boundary conditions [134].

In order to solve the stationary state of the open ASEP, Derrida et al. proposed an approach which is now called Matrix Product Ansatz. It is a brilliant method far more useful than it was thought to be at the beginning. Interested readers are referred to the review paper for more details [121]. The work of Derrida and co-workers significantly boosted the research on ASEP. Many significant contributions were made to the field of ASEP. For example, De Gier found the exact solution of open ASEP with certain special constraints in 2005 [135]. Spohn et al. constructed an exact solution of the KPZ equation using the ASEP in 2010 [136].

Despite the simplicity of the ASEP model, the way to find the solution of general

open ASEP system is still an open question [122, 133]. Although the Matrix Product Ansatz is widely used in the study of the stationary state ASEP, the Bethe ansatz method is more powerful when it comes to the dynamics.

Besides the periodic ASEP and open ASEP, the model we discuss in this work is the ASEP with reflecting boundaries. There are not so many results for this case. One of the exceptions is the work of Schütz et al. in 1994. They investigated the reflecting ASEP using the $U_q(SU(2))$ quantum group approach [137]. The exact stationary solution was found but not the dynamics. The reason for the lack of study on this specific case might be the inanimate steady state. There is no current in the stationary state, which makes the system looks less interesting to explore. However, we show that it is actually quite intriguing especially when we notice the mapping from ASEP to polymer dynamics.

The reflecting ASEP can be solved completely by using the Bethe ansatz method, which we briefly introduce below.

1.3.2 Bethe ansatz

Bethe ansatz is a method proposed by Hans Bethe in 1931 in order to solve the Heisenberg spin chain model with periodic boundary conditions [138]. At that time, he probably did not realize his great work would open a new branch of physics which is now called the integrability theory [126]. In 1963, Lieb-Liniger used the Bethe ansatz method to solve the dynamics of Bose gas with δ interaction potential [139, 140].

Another important application of the Bethe ansatz is the six-vertex model which was also solved by Lieb [141–143]. The next big step was the discovery of the Yang-Baxter equation, which was introduced independently by Chen-Ning Yang and Rodney Baxter [144, 145]. The Yang-Baxter equation provides a criterion to find out whether a model is integrable or not [126]. The investigation of the Yang-Baxter equation led to the introduction of quantum group theory and the theory of topological knot invariants [126].

During the 1970s and 1980s, advanced Bethe ansatz methods like functional Bethe ansatz and algebraic Bethe ansatz were developed [122]. After the introduction of the ASEP model, these Bethe ansatz methods were quickly adopted to find the solution of these many particle systems because of the intrinsic connection from ASEP to a spin chain system. For example, the solution of the periodic ASEP is almost identical to the Heisenberg spin chain with periodic boundary conditions [122]. The study of ASEP and Bethe ansatz is still a very active field. There are a lot of references one can refer to [121, 122, 146–148].

1.4 Outline

With the introduction of the biological problem and the background of polymer modeling as well as ASEP in previous sections, we are ready to go into the details of our study. But before that, our research goals and the overview for the organisation of this thesis are discussed.

1.4.1 Research goals

The research goals of this thesis are as follows:

- To propose a polymer model in order to describe the chromosomes in fission yeast during nuclear oscillations. We will refer to it as a pulled polymer loop model.
- To develop the quantitative theory for our pulled polymer loop model and to find the analytic solution for the steady state and dynamics of the model with a simple setting.
- To perform numerical simulations for the polymer model. These numerical results verify our analytic theory. Also, by performing more realistic simulations, the results can be used to justify the assumptions of our simplified model.
- To understand the biological processes such as chromosome alignment through the physical insight gained by the above studies. Understanding the biology of this process is our ultimate goal.

In short, we want to quantitatively model the chromosome dynamics during the nuclear oscillations. We will critically discuss the relevance of our results to the biological process.

1.4.2 Overview of the thesis

A brief outline of the thesis is as follows:

In chapter 2, we discuss the details of our pulled polymer loop model. Two realizations of the model, i.e. bead-rod model and bead-spring model are introduced. By introducing a coordinate transformation, it is shown that the pulled polymer loop can be transferred to the pinned polymer loop in an external force field. We then discuss the simulation techniques of the polymer model, including the Brownian Dynamics simulation and the Monte Carlo simulation specifically for the bead-rod model.

In chapter 3, we solve the equilibrium statistics of pinned polymer loop in a constant external force field. The system is solved firstly in 1D by two different methods. The mapping from polymer loop to a particle system on a lattice is illustrated. Then we extend our solution to the three-dimensional setting. To address the alignment of homologous chromosomes we consider the statistics of the distance between two identical loops. We also show how this distance changes if additional contact points between loops are introduced to mimic recombination contacts between chromosomes.

Based on the solution of equilibrium statistics, we also quantify the shape of the pinned polymer loops in the external force field.

In chapter 4, we investigate the relaxation dynamics of the pinned polymer loop in an external force field. First we show that within the Rouse theory of pinned polymer loop, the relaxation time is independent of the external force. This is clearly not what we see in numerical experiments. To understand the relaxation dynamics we introduce the mapping from polymer dynamics to the particle hopping of ASEP. The pinned polymer loop model is mapped to reflecting ASEP system with exactly half of the lattice sites occupied. The Bethe ansatz method is employed to find the exact solution of the ASEP system. Results from ASEP are mapped back to the polymer loop model to discuss the relaxation dynamics of the polymer where we recover the relaxation time dependence on external force. The dynamics of stretch and coil transition is discussed briefly.

In the last chapter, chapter 5, we first summarize our results and discuss their relevance to the problem of chromosome alignment in fission yeast. Finally, we conclude with an outlook in the final section.

Chapter 2

Theoretical Model and Numerical Simulation Methods

To model the chromosome movements during nuclear oscillation in fission yeast, we begin with a single chromosome modeled by a single polymer loop. This chapter presents the details of the polymer model for chromosomes and the simulation methods used in the study of the dynamics and statistics of the polymer.

2.1 Stochastic models of polymer loops

There are three pairs of chromosomes in fission yeast [12]. During nuclear oscillation, these three pairs of chromosomes bound to one point, i.e. the spindle pole body (SPB). We begin with the simplest case, neglect the interactions between chromosomes, and consider only a single chromosome. It is a polymer with a loop geometry, and an external force is exerted on the SPB. There are two standard ways to model a polymer, namely the bead-rod model and the bead-spring model. In the bead-spring model, the beads are connected by massless springs, whereas in the bead-rod model, the beads are connected by massless rods with fixed length. We use both models in this thesis but more emphasis will be put on the bead-rod model. Both models have their own benefits and shortcomings. Computationally, it is easier to work with the bead-spring model than with the bead-rod. However, the bead-rod has the intrinsic property of finite extensibility without resorting to some complex nonlinear spring potentials [149, 151]. In fact, we will show that the finite extensibility takes an important role for the polymer dynamics in Chapter 4. In this section, we establish both the bead-rod and bead-spring model for modeling the polymer loop.

2.1.1 Coordinate transformation

Consider a single chromosome pulled at the SPB. Due to the large viscosity of the fission yeast nucleoplasm (1000 times of the viscosity of water) [39], the chromosome can be assumed to be in an overdamped regime [151]. The chromosome is pulled to move with a constant velocity \mathbf{v} , see Fig. 1.8. In our model, the SPB is represented as

one monomer in the polymer loop. Other monomers modelling the rest of the polymer move together to follow the SPB, see Fig. 2.1 (a).

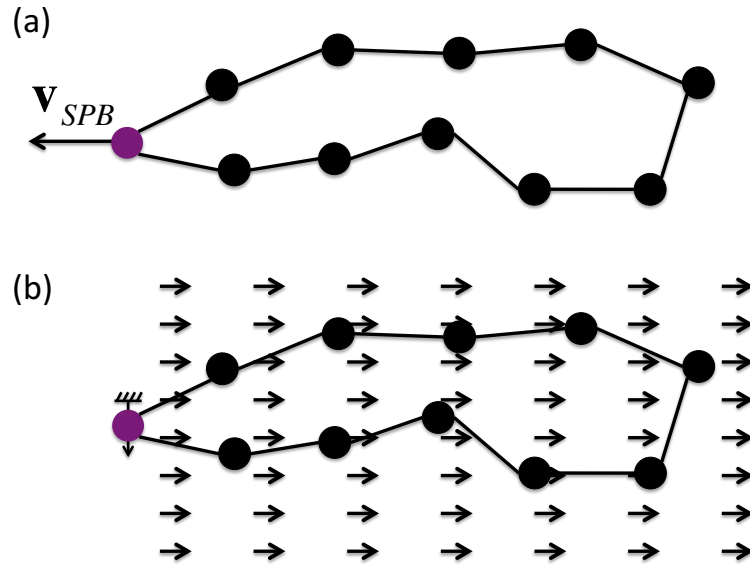


Figure 2.1: Illustration of reference frame transformation. (a) a pulled polymer loop before transformation; (b) pinned polymer loop in an external field after transformation.

Now we perform a change of reference frame to the co-moving frame of the SPB. Then effectively, the SPB is not moving, and the polymer loop is immersed in a fluid flow with a velocity $-\mathbf{v}$ (Fig. 2.1 (b)). Assuming the Stoke's law is valid, there is a force $\mathbf{F}^e = -\xi\mathbf{v}$ acting on every bead. Here ξ is the friction coefficient for the bead in a fluid. The free-draining assumption is applied, which means that there is no hydrodynamic interactions between beads.

Using this co-moving reference frame, the pulled polymer loop model is transformed to the pinned polymer loop in a uniform external force field. In the following, the pinned polymer loop picture is employed for easier numerical and analytical calculations. For example, in simulations, a very large pulling force might be required if the first picture is adopted, that might become a bottleneck for the choice of the integration time step. In theory, the force field picture offers a clean way to calculate the energy of polymer configurations. Thus the pinned picture is used in the following.

2.1.2 Bead-rod model

Now we discuss a concrete polymer model for modeling the chromosomes, namely the bead-rod model. The beads representing chromosome segments are connected by the massless rigid rods. For simplicity, we assume the length of every rod to be identical, and denote it by a . The rigidity of the rod means that the distance between two neighboring beads is fixed.

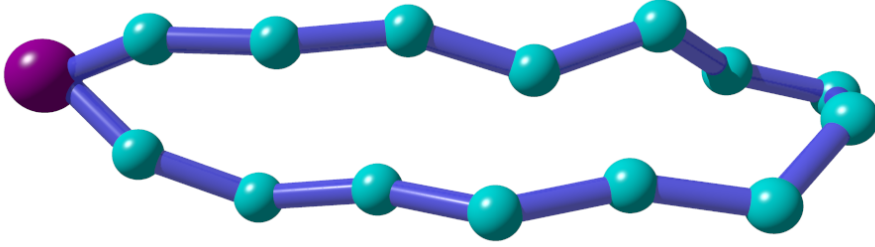


Figure 2.2: Sketch of the bead-rod loop model. The magenta bead represents the SPB and other cyan beads represent the polymer segments.

The dynamics of the polymer is specified by the motion of the beads. We shall first formulate the dynamics equations. The contour length of the polymer loop is La , i.e., there are L beads (including the SPB) and L rods with the length a in the polymer. Denote the beads by their index $i = 0, 1, 2, \dots, L - 1, L$. The periodic indexing is used due to the looping geometry, namely for any indexed quantity x , $x_0 = x_L$. The equation describing the dynamic of the bead i in the overdamped regime reads

$$\xi \frac{d\mathbf{r}_i}{dt} = \mathbf{F}_i^u + \mathbf{F}_i^c + \mathbf{F}_i^{pseudo} + \mathbf{F}_i^e + \mathbf{F}_i^b, \quad (2.1)$$

where ξ is the friction coefficient of the bead in a fluid, \mathbf{r}_i is the bead position, \mathbf{F}_i^u is the interaction force specified by interacting potentials, \mathbf{F}_i^c is the constraint force which keeps the rod length fixed, \mathbf{F}_i^e is the external force, and \mathbf{F}_i^b is the Brownian force caused by fluctuations. \mathbf{F}_i^{pseudo} is a *pseudo* force introduced to the bead-rod model in order to preserve the “correct” statistics under fluctuations (see the next section for more details).

Now we provide several remarks on Eq. (2.1). Firstly, \mathbf{F}_i^b is a random force, so Eq. (2.1) is a stochastic differential equation. Secondly the left-hand side of Eq. (2.1) is just the friction force of the bead in the fluid $-\xi\mathbf{v}_i$. We assumed the fluid is homogeneous so that the friction coefficient is independent of the space and time. Thirdly, the inertia of the bead is neglected which means the polymer is in the overdamped regime. In other words, Eq. (2.1) essentially can be written as $\mathbf{F}_i^{total} = \mathbf{0}$ which is the Newton’s second law with neglected inertia. This kind of dynamics is commonly used

in polymer physics and referred to as Brownian Dynamics [150, 151].

In the following, we explain the terms of the right-hand side of Eq. (2.1) in details.

Brownian force \mathbf{F}_i^b

The Brownian force is a consequence of the instantaneous collisions of the fluid molecules and other interactions between chromosomes and proteins in the nucleus. The level of fluctuation is assumed to be characterized by an effective temperature T . Mathematically, the Brownian force is modelled by a Gaussian process with the zero mean, non-zero second moment and δ -correlated in time, which can be written as:

$$\langle \mathbf{F}_i^b \rangle = \mathbf{0}, \quad (2.2a)$$

$$\langle \mathbf{F}_i^b(t) \mathbf{F}_j^b(t') \rangle = 2k_B T \xi \delta_{ij} \delta(t - t'), \quad (2.2b)$$

here, k_B is the Boltzmann constant. δ_{ij} is the Kronecker delta meaning there is no correlation for the Brownian force exerted on different beads. The second δ is the Dirac delta function.

External force \mathbf{F}_i^e

The external force in our pinned polymer loop model is exerted by the equivalent flow field, which follows from coordinate transformation. In the co-moving frame of reference, $\mathbf{F}_i^e = \xi \mathbf{v}_{\text{SPB}}$. In general, $\mathbf{v}_{\text{SPB}} = \mathbf{v}_{\text{SPB}}(t)$ is a function of time. However, in the simplest case where the chromosome is pulled to move steadily in one direction during half period of one oscillation, \mathbf{v}_{SPB} is considered to be a constant.

Constraint force \mathbf{F}_i^c

The constraint force is the tension and stress applied to the rod to keep its length fixed. Therefore, the direction of the force is along the rod orientation. The rigid rod constraint can be written as

$$|\mathbf{r}_i - \mathbf{r}_{i-1}| - a = 0, \quad (2.3)$$

and $\mathbf{r}_0 = \mathbf{r}_L$ for the periodic indexing. The constraint force is an implicit force that depends on the other forces acting on the beads. We leave the discussion of how to calculate this force to the next section which is devoted to simulations.

Pseudo force $\mathbf{F}_i^{\text{pseudo}}$

The pseudo force is a special virtual force that is added in order to recover the ‘‘correct’’ statistics. If we neglect the bending energy, excluded volume effects, and other complex interactions, the model is essentially the simplest freely jointed polymer model. For such a simple model, the orientation of two consecutive rods is considered to be

independent. In other words, the distribution of the angle between two rods should be uniform. However, we cannot obtain such statistics in the bead-rod model without introducing the pseudo force.

For example, let us consider a simple trimer in 3D. Denote angle between two rods of the trimer as θ . Notice that the 3D spherical uniform distribution can be written as

$$p(\theta) = \frac{1}{2} \sin \theta. \quad (2.4)$$

However, the distribution of rigid bead-rod trimer without pseudo force can be derived using the generalized coordinates [152]

$$p(\theta) = \frac{120}{203} \left(1 - \frac{1}{4} \cos^2 \theta\right)^{1/2} \sin \theta. \quad (2.5)$$

The reason for the discrepancy between Eq. (2.4) and Eq. (2.5) is the rigidity of the rod constraints. Because the constraint is rigid, the phase space of a bead-rod trimer is a 4-dimensional manifold [153]. The simple Brownian force ensures that the probability is uniform among the manifold but not θ .

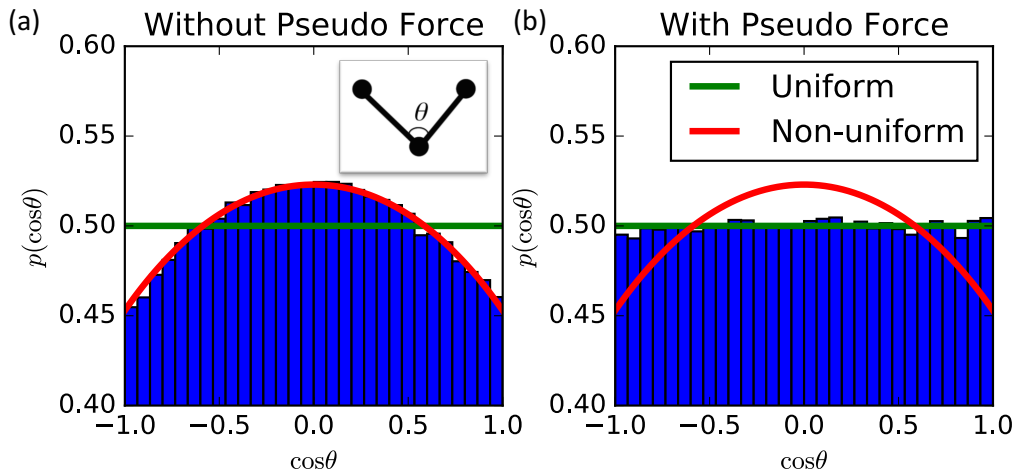


Figure 2.3: The distribution of the angle of a bead-rod trimer. (a) without pseudo force; (b) with pseudo force. The blue bins are from Brownian Dynamics simulation results. Inset of (a) is a sketch for the trimer.

To solve the problem and obtain the statistics of the freely jointed chain, Fixman introduced an effective pseudo potential which depends on the polymer configuration

[154]. The explicit form of the pseudo force can be written as

$$\mathbf{F}_i^{pseudo} = -\frac{\partial U_{met}}{\partial \mathbf{r}_i}, \quad (2.6a)$$

$$U_{met} = \frac{1}{2}k_B T \ln(\det \mathbf{G}), \quad (2.6b)$$

where \mathbf{G} is the metric matrix of the bead-rod system [149]. The details of \mathbf{G} and the calculation of pseudo force are given in the next section.

Other potential forces \mathbf{F}_i^u

Other potential forces account for the forces derived from bending energy, excluded volume effect, hydrodynamic interactions and other interaction potentials. The general form of this force can be written as

$$\mathbf{F}_i^u = -\sum_U \frac{\partial U}{\partial \mathbf{r}_i}, \quad (2.7)$$

where U is a sum over all potentials taken into account. For instance, the bending potential can be calculated as

$$U_{bend} = -\frac{\kappa}{a} \sum_{i=1}^L \mathbf{u}_i \cdot \mathbf{u}_{i-1} \quad (2.8)$$

where $\mathbf{u}_i = (\mathbf{r}_i - \mathbf{r}_{i-1})/a$ is the unit vector of rod orientation, κ is the bending stiffness and a is the rod length.

For the excluded volume effect, the repulsive interactions might be modeled by a pure repulsive Lennard-Jones potential

$$U_{LJ} = \begin{cases} 4\epsilon \left[\left(\frac{\sigma}{r}\right)^{12} - \left(\frac{\sigma}{r}\right)^6 \right], & \text{if } r \leq r_c; \\ 0, & \text{if } r > r_c; \end{cases} \quad (2.9)$$

where r is the distance between two beads and $r_c = 2^{1/6}\sigma$. ϵ and σ are two parameters that specify the repulsive strength and the effective size of the beads, respectively.

One can add more interaction potentials into the model. However, adding more potentials could easily lead to a complex model with many parameters. For simplicity, we ignore these forces in most of our analysis unless otherwise specified.

2.1.3 Bead-spring model

Bead-spring model is another commonly used polymer model [151]. There are several reasons to use the bead-spring model complementary to the bead-rod model. Firstly,

the bead-spring model can serve as a benchmark for the bead-rod model. Unlike the bead-rod model where a pseudo force has to be added to obtain the freely jointed chain statistics, the model of beads connected by Hookean springs naturally exhibits such statistics. Secondly, the role of finite extensibility of the chain can be understood by comparing the inextensible bead-rod model to infinitely extensible bead-spring model. Thirdly, the computation power needed for the bead-spring model simulations is often less than that required for the bead-rod, because we avoid calculating the pseudo force and implicit constraint force.

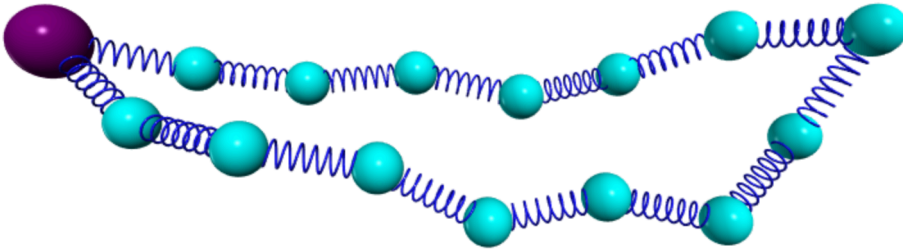


Figure 2.4: Sketch of the bead-spring loop model. The magenta bead represents the SPB and other cyan beads represent the polymer segments.

To model the chromosome in fission yeast during nuclear oscillation, we need to impose a looping structure. The first bead represents the SPB, as shown in Fig. 2.4. The equation of motion is similar to that of the bead-rod model, and can be written as:

$$\xi \frac{d\mathbf{r}_i}{dt} = \mathbf{F}_i^u + \mathbf{F}_i^{spring} + \mathbf{F}_i^e + \mathbf{F}_i^b. \quad (2.10)$$

The notations here are the same as in the bead-rod model. In addition, the Brownian, external and the potential forces also are the same as in the bead-rod model. However, here the pseudo force is not needed and the constraint force is replaced by the spring force \mathbf{F}_i^{spring} . We notice that for a bead in the loop, there are two springs connected to it. Thus

$$\mathbf{F}_i^{spring} = F_{i+1}^s(Q_{i+1})\mathbf{u}_{i+1} - F_i^s(Q_i)\mathbf{u}_i, \quad (2.11)$$

where $F_i^s(Q_i)$ is the tension of the spring i , Q_i is the length of the spring, and \mathbf{u}_i is the unit vector for the orientation of the spring i .

There are different types of springs one can use for this model. Here, we introduce two most commonly used ones.

Hookean spring

Hookean spring is a linear spring, where the tension of the spring depends linearly on its length:

$$F^{Hookean} = H(Q - Q_0), \quad (2.12)$$

where H is the spring constant and Q_0 is the natural length of the spring. In practice, Q_0 is set to a , which equals to the length of the bead-rod model. However, sometimes the zero length springs are also used [150, 151].

Finite Extensible Nonlinear Elastic (FENE) spring

FENE spring is another commonly used spring. The force law of this spring is

$$F^{FENE} = \frac{HQ}{1 - (Q/R_0)^2}, \quad (2.13)$$

where R_0 is the maximal allowed length of the spring. As we can see in Eq. (2.13), $F^{FENE} \rightarrow \infty$ when $Q \rightarrow R_0$ [150, 151].

In this section, we specified the equations describing the dynamics of the polymer in our model. Next we discuss the detail of numerical simulations of used to solve these equations.

2.2 Brownian Dynamics simulations

In Brownian Dynamics (BD) simulations, the governing equation of beads are integrated to deliver their trajectories. Physical quantities are measured by ensemble average over trajectories of monomers. In our case, the governing equations are Eq. (2.1) or Eq. (2.10). Examples quantities in which we are interested are the average spatial distance between any of the two beads, the typical size of the polymer, and the characteristic time scale of the system dynamics. These quantities can be obtained by BD simulations.

In the following subsections, we introduce the algorithms used to perform the bead-rod and bead-spring simulation separately. The simulation code is implemented in C++2011. Most of the simulation are computed in the clusters of MPI-PKS with X86 architecture.

2.2.1 BD simulation of the bead-rod model

The goal of the simulation is to solve the stochastic differential equation Eq. (2.1) numerically. However, the simple integration algorithm such as the Euler-Maruyama algorithm would not work here. This is because of the implicit constraint force \mathbf{F}_i^c . Here we use the predictor-corrector algorithm introduced by Liu [155].

To simplify the illustration of the algorithm, we assume that all complex potential forces and the external force in Eq. (2.1) are zero, i.e. $\mathbf{F}_i^u = \mathbf{F}_i^e = \mathbf{0}$. The dynamic equation is then simplified as

$$\frac{d\mathbf{r}_i}{dt} = \frac{1}{\xi} \left(\mathbf{F}_i^c + \mathbf{F}_i^{pseudo} + \mathbf{F}_i^b \right). \quad (2.14)$$

The predictor-corrector algorithm is a two-step algorithm and can be divided into the prediction step and correction step.

Prediction step

In the prediction step, the estimation of next time step bead position is evaluated without considering the constraints

$$\mathbf{r}_i^*(t + \Delta t) = \mathbf{r}_i(t) + \frac{1}{\xi} (\mathbf{F}_i^{pseudo} + \mathbf{F}_i^b) \Delta t. \quad (2.15)$$

In order to perform the calculation, we need to evaluate the Brownian force and the pseudo force first.

- Evaluation of the Brownian force \mathbf{F}_i^b

The Brownian force is generated by a Gaussian distributed pseudo random number. Eq. (2.15) can be written more practically as

$$\mathbf{r}_i^*(t + \Delta t) = \mathbf{r}_i(t) + \frac{1}{\xi} \mathbf{F}_i^{pseudo} \Delta t + \sqrt{\frac{2k_B T}{\xi} \Delta t} \mathbf{N}_i(0, 1), \quad (2.16)$$

where $\mathbf{N}_i(0, 1)$ is a multi-dimensional Gaussian random number with mean 0 and variance 1.

- Evaluation of the pseudo force \mathbf{F}_i^{pseudo}

The expression for pseudo force is given in Eq. (2.6). However, the evaluation is numerically expensive. To perform, we first write down the metric tensor \mathbf{G} .

$$G_{\alpha\beta} = \sum_i \frac{\partial g^\alpha}{\partial \mathbf{r}_i} \cdot \frac{\partial g^\beta}{\partial \mathbf{r}_i}, \quad (2.17)$$

where g^α is the constraint equation indexed α that can be written as a function of beads position:

$$g^\alpha(\mathbf{r}_1, \mathbf{r}_2, \dots, \mathbf{r}_L) = 0. \quad (2.18)$$

In the case of a bead-rod loop, Eq. (2.3) is the concrete representation of Eq. (2.18).

The $L \times L$ metric tensor takes the form

$$\mathbf{G} = \begin{bmatrix} d_1 & c_1 & 0 & \cdots & c_L \\ c_1 & d_2 & c_2 & \cdots & 0 \\ \vdots & \ddots & \ddots & \ddots & \vdots \\ 0 & \cdots & c_{L-2} & d_{L-1} & c_{L-1} \\ c_L & \cdots & 0 & c_{L-1} & d_L \end{bmatrix}, \quad (2.19)$$

where diagonal elements $d_i = 2$, and the off-diagonal elements

$$c_i = -\mathbf{u}_i \cdot \mathbf{u}_{i-1} \quad (2.20)$$

Again here, the periodic index is applied, i.e. $\mathbf{u}_0 = \mathbf{u}_L$. Now, the pseudo force can be calculated as

$$\begin{aligned} \mathbf{F}_i^{pseudo} &= -\frac{1}{2}k_B T \frac{\partial \ln(\det \mathbf{G})}{\partial \mathbf{r}_i} \\ &= -\frac{1}{2}k_B T \sum_{\alpha, \beta} \frac{1}{\det \mathbf{G}} \frac{\partial \det \mathbf{G}}{\partial G_{\alpha\beta}} \frac{\partial G_{\alpha\beta}}{\partial \mathbf{r}_i} \\ &= -\frac{1}{2}k_B T \sum_{\alpha, \beta} G_{\beta\alpha}^{-1} \frac{\partial G_{\alpha\beta}}{\partial \mathbf{r}_i}. \end{aligned} \quad (2.21)$$

In order to calculate the pseudo force, the matrix \mathbf{G} has to be inverted. This operation is very expensive. Fortunately, the symmetric shape of \mathbf{G} in Eq. (2.19) guarantees an efficient algorithm to do the computation. We use the algorithm developed by Pasquali and Morse in [149], which is invented for the BD simulation of a bead-rod chain. We modified it to adopt the loop geometry and applied it on our BD simulations. See Appendix A for details.

Correction step

The correction step utilizes the result of the prediction, and corrects it with the constraint force to obtain the real next time step bead position.

$$\mathbf{r}_i(t + \Delta t) = \mathbf{r}_i^*(t + \Delta t) + \frac{1}{\xi} \mathbf{F}_i^c \Delta t. \quad (2.22)$$

The rigid rod constraints must be satisfied after the correction. Substitute Eq. (2.22) into Eq. (2.3) and also notice that

$$\mathbf{F}_i^c = \lambda_{i+1} \mathbf{u}_{i+1} - \lambda_i \mathbf{u}_i \quad (2.23)$$

where λ_i is the magnitude of tension on the i^{th} rod. Thus we obtain

$$\begin{aligned} & 2\Delta t \mathbf{b}_i \cdot (\lambda_{i-1} \mathbf{u}_{i-1} - 2\lambda_i \mathbf{u}_i + \lambda_{i+1} \mathbf{u}_{i+1}) \\ = & \xi (a^2 - \mathbf{b}_i \cdot \mathbf{b}_i) - \frac{(\Delta t)^2}{\xi} (\lambda_{i-1} \mathbf{u}_{i-1} - 2\lambda_i \mathbf{u}_i + \lambda_{i+1} \mathbf{u}_{i+1})^2. \end{aligned} \quad (2.24)$$

Here $\mathbf{b}_i = \mathbf{r}_i^*(t + \Delta t) - \mathbf{r}_{i-1}^*(t + \Delta t)$. This is a set of nonlinear algebraic equations. The second term at the right hand side is the nonlinear term. The nonlinear term is small when the time step Δt is small enough. Numerically, it is suitable to use the iteration methods, for example the Picard's method, to solve this set of equations. High order methods such as the Newton's method are also applicable, but require the calculation of Jacobian matrix in every time step. In practice, a small time step is necessary for the convergence of root searching. We use a time step between $10^{-5} - 10^{-3}$ depending on different situations. Once we solve the tension λ_i , plug them in to Eq. (2.23) and then Eq. (2.22), the next time step bead position is obtained.

Finally, we want to remark on how to pin the first bead of the bead-rod model. One has several possible ways to do this. The first one is to use a very stiff zero-length spring attached the first bead at a certain point. This method is straightforward to implement. However, the use of the pinning spring introduces a high-frequency factor into the polymer dynamics, which is not desired for analyzing. Also, the attached spring length is not perfectly zero when the polymer is subjected to a strong force field. Instead, we use another method, i.e. pin the first bead use the zero-length rigid rods. In fact, we need three of this kind of "ghost" rods in 3D, the orientation of the being rods along three axes respectively. This method requires solving the additional constraint forces. The calculation is similar to the way of calculating \mathbf{F}_i^c .

2.2.2 BD simulation of the bead-spring model

The BD simulation of the bead-spring model is more straightforward. Neither implicit constraint force nor complex interaction forces are needed to be evaluated during every time step. Of course, one can also use an implicit algorithm which allows the use of a larger time step [150, 151]. However, we simply use the explicit algorithms [150, 151] here, which are the Euler and the stochastic Runge-Kutta methods.

Euler method

Euler method, also called Euler–Maruyama method, is a 1/2 order integration scheme. In principle, the convergence is only guaranteed when $\Delta t \rightarrow 0$. However, it is still widely used because of its simplicity, especially when the variation of the drift and diffusive term in the stochastic differential equation is not too large. The beads connected by Hookean spring is a good example that fits in this method.

Using this method, the next time step bead position in our simple example can be

calculated as

$$\mathbf{r}_i(t + \Delta t) = \mathbf{r}_i(t) + \frac{1}{\xi} \mathbf{F}_i^{det} \Delta t + \sqrt{\frac{2k_B T}{\xi}} \Delta t \mathbf{N}_i(0, 1), \quad (2.25)$$

where $\mathbf{F}_i^{det} = \mathbf{F}_i^u + \mathbf{F}_i^{spring} + \mathbf{F}_i^e$ is the total deterministic force. Also notice that, the \mathbf{F}_i^{spring} is evaluated by Eq. (2.11) and the spring force law Eq. (2.12) or Eq. (2.13).

Stochastic Runge–Kutta method

Stochastic Runge–Kutta method is a higher order explicit integration scheme than the Euler method. It was proposed by Honeycutt [156]. In this method, the next time step bead position can be calculated as

$$\mathbf{r}_i(t + \Delta t) = \mathbf{r}_i(t) + \frac{1}{\xi} (\mathbf{F}_i^{det} + \tilde{\mathbf{F}}_i^{det}) \frac{\Delta t}{2} + \sqrt{\frac{2k_B T}{\xi}} \Delta t \mathbf{N}_i(0, 1), \quad (2.26)$$

where \mathbf{F}_i^{det} and $\tilde{\mathbf{F}}_i^{det}$ are the total deterministic force evaluated using different bead position.

$$\begin{aligned} \mathbf{F}_i^{det} &= \mathbf{F}_i^{det}(\mathbf{r}_0(t), \mathbf{r}_1(t), \dots, \mathbf{r}_{L-1}(t)), \\ \tilde{\mathbf{F}}_i^{det} &= \tilde{\mathbf{F}}_i^{det}(\mathbf{r}_0^*, \mathbf{r}_1^*, \dots, \mathbf{r}_{L-1}^*), \end{aligned} \quad (2.27)$$

and \mathbf{r}_i^* is the mid-step bead position

$$\mathbf{r}_i^* = \mathbf{r}_i(t) + \frac{1}{\xi} \mathbf{F}_i^{det} \Delta t + \sqrt{\frac{2k_B T}{\xi}} \Delta t \mathbf{N}_i(0, 1). \quad (2.28)$$

Last but not least, in the simulations, the dynamic equations are made dimensionless by rescaling the variable in the following way:

$$\mathbf{r}' \rightarrow \mathbf{r}/a; \quad t' \rightarrow t/(\xi a^2/k_B T); \quad \mathbf{F}' \rightarrow \mathbf{F}/(k_B T/a). \quad (2.29)$$

The rescaled factor $\xi a^2/k_B T$ means the diffusion time of a free immersed bead over a distance of rod length a and $k_B T/a$ is the magnitude of the entropic force. After the rescaling, the length unit is set to the size of the rod. The rescaling is helpful to avoid calculations with too small or too large values, which is prone to higher numerical errors.

2.3 Monte Carlo simulation of the bead-rod model

In the previous section, we presented the BD simulation technique of the bead-rod and bead-spring polymer loop. The algorithm used to simulate the bead-rod model

is quite complex and consequently time-consuming. Sometimes we do not need to do that if we only want to sample the equilibrium properties of the bead-rod system. In this section, a much faster and efficient Monte Carlo algorithm is introduced to obtain the equilibrium statistics of the bead-rod loop model.

Monte Carlo technique has been used to simulate polymer systems for a long time [157–159]. However, there are some special factors one need to take into account for our pinned polymer loop model. Basically, one has to preserve the loop structure and keep the rod length fixed when trying to perform a Monte Carlo flip. Here we give a brief stepwise description of the Monte Carlo simulation method, which has been used in Ref. [85].

- Step I: prepare an initial configuration and compute the energy of this configuration. The way of calculating system energy depends on the setting of the model, whether the excluded volume effect or other interactions are taken into account or not. For example, the energy of a pinned bead-rod loop in a constant external force field can be written as

$$E = U - \sum_{i=1}^L \mathbf{F}^e \cdot \mathbf{r}_i \quad (2.30)$$

where U is other kind of interaction energy such as Lennard-Jones potential. In the simplest case, we assume U to be independent of the configurations. To compare with the later evaluation, we denote the energy calculated here as E_{old} .

- Step II: randomly choose two beads in the polymer loop, use the connecting line between the two beads as a rotation axis.

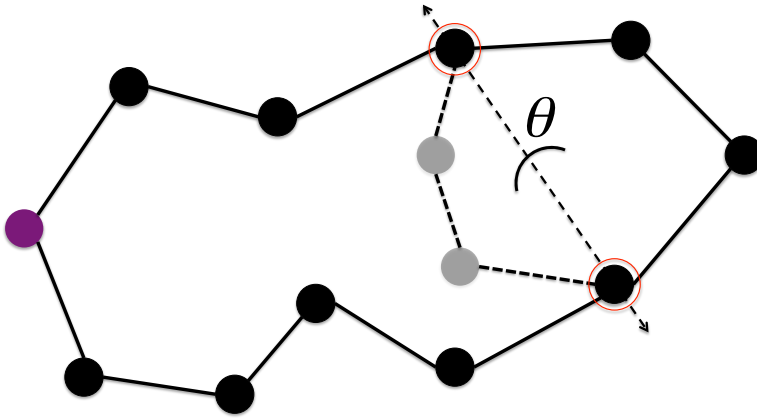


Figure 2.5: Illustration of the Monte Carlo configuration flip.

- Step III: choose the unpinned side of the polymer, and rotate this part of the polymer by a random angle $\theta \in [-\phi, \phi]$. ϕ is a parameter between $[0, \pi]$ and can be tuned to improve the efficiency of the algorithm (see Fig. 2.5). If the pinned bead is selected, then randomly choose one side of the polymer to perform the rotation.
- Step IV: calculate the energy of the configuration after rotation in the same way as E_{old} . Let us denote the new energy as E_{new} .
- Step V: the new configuration is accepted with probability

$$p = \min \left\{ 1, \exp \left(-\frac{\Delta E}{k_B T} \right) \right\}, \quad (2.31)$$

where $\Delta E = E_{new} - E_{old}$. If not accepted, then the polymer returns to the old configuration. Repeat the process with new rotation axis. An efficient sampling algorithm can be tuned by parameter ϕ so that the accept probability is around 0.5.

- Step VI: go back to step I and loop again and again to get enough independent samples. Physical quantities such as the statistical distance between two beads can be calculated by averaging over these samples.

The Monte Carlo method introduced in this section is efficient and fast, we use it to calculate most of the equilibrium quantities in next chapters. On the other hand, the Monte Carlo results also work as a benchmark of the BD simulation and vice-versa.

2.4 Summary

In this chapter, we elaborated the details of our pulled polymer model for the chromosomes in meiotic fission yeast. We have shown that the pulled polymer loop can be transferred to the pinned polymer loop in an external force field after a coordinate transform. The concrete bead-rod and bead-spring polymer loop models were discussed. The BD simulation technique was discussed in details. A Monte Carlo algorithm was introduced to calculate the equilibrium statistics of the bead-rod system and to overcome the disadvantages of heavy computation of the BD simulation.

In the next chapter, we discuss the theory of equilibrium statistics of the pinned polymer loop model.

Chapter 3

Equilibrium Statistics of the Forced Pinned Polymer Loop

In this chapter, we investigate the equilibrium statistics of the model and use the results to understand the chromosome alignment in fission yeast.

In order to treat the model analytically, we neglect the complex interactions such as bending energy, excluded volume effect, and hydrodynamical interactions. In other words, our model for analytical investigation is the simplest freely-jointed polymer loop model. The transformation of coordinates is utilized so that the first bead representing SPB is pinned in space, and an external force field is applied to the rest of the polymer.

We begin with the description of the model in the first section. The equilibrium statistics in 1D and 3D are discussed separately in section two and three, respectively. In the fourth section, we discuss the shape of the steady pinned polymer loop in an external force field. The studies that are described in the Section. 3.2 and Section. 3.3 were done in cooperation with Yen-Ting Lin.

3.1 Pinned polymer loop in a constant force field

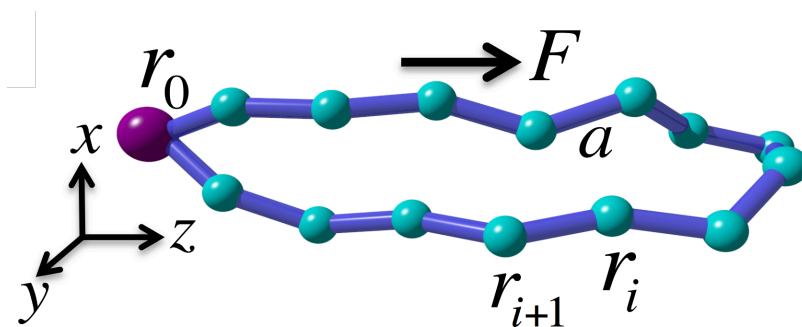


Figure 3.1: Sketch for the pinned bead-rod loop and notations.

We consider a pinned polymer loop in a constant external force field. We first establish the notations. There are L beads (including the SPB) in the loop and the

SPB is denoted by \mathbf{r}_0 or \mathbf{r}_L with periodic indexing. Without loss of generality, we assume that it is pinned to the origin of the coordinate system, $\mathbf{r}_0 = \mathbf{r}_L = \mathbf{0}$. The length of each rod is defined to be a constant a . The constant external force field $\mathbf{F} = F\mathbf{e}_z$ is in the z direction. The potential energy of the pinned polymer loop can be written as:

$$E = E_0 - a \sum_{i=1}^L \mathbf{F} \cdot \mathbf{r}_i, \quad (3.1)$$

where E_0 is assumed to be a constant that denotes configuration independent energy. E_0 is not relevant for the study of equilibrium statistics, but we keep it here for completeness. The orientation of the rod j is denoted by $\mathbf{u}_j = (\mathbf{r}_j - \mathbf{r}_{j-1})/a$. The i^{th} bead position can be written as:

$$\mathbf{r}_i = a \sum_{j=1}^i \mathbf{u}_j. \quad (3.2)$$

By plugging it into Eq. (3.1), we arrive at

$$E = E_0 - a \sum_{i=1}^L \sum_{j=1}^i \mathbf{F} \cdot \mathbf{u}_j. \quad (3.3)$$

Notice that the looping condition indicates

$$\sum_{j=1}^L \mathbf{u}_j = 0. \quad (3.4)$$

In the following two sections, we solve the equilibrium statistics in 1D first and then extend the theory to 3D.

3.2 Pinned Polymer Loop in 1D

The one-dimensional polymer is a theoretical construction where we neglect the exclusion volume effect so that the beads and rods can overlap freely. We will show that there exists a peculiar mapping from the one-dimensional pinned polymer loop to a classical particle-lattice model.

3.2.1 Mapping to a particle system on 1D lattice

The configuration of the one-dimensional polymer can be specified by the orientation of the rods in 1D. There are only two possible orientations, i.e., $+\mathbf{e}_z$ or $-\mathbf{e}_z$. We denote the j^{th} rod orientation by $u_j \in \{-1, +1\}$, where $u_j = +1$ means the rod orientates

along $+\mathbf{e}_z$ and $u_j = -1$ means the rod orientates along $-\mathbf{e}_z$. Again, the i^{th} bead position in 1D is $z_i = a \sum_{j=1}^i u_j$. We introduce a shifted and rescaled variable

$$n_j = (u_j + 1)/2. \quad (3.5)$$

Then $n_j \in \{0, 1\}$, and the configuration of the 1D polymer can be represented by $\{n_1, n_2, \dots, n_L\}$. Since n_j is a binary variable, we can interpret $n_j = 1$ as a lattice site occupied by a particle, and $n_j = 0$ as an empty lattice site. In this way, we find a one-to-one mapping from the configuration of polymers to particles on lattice sites (see in Fig. 3.2). Here, the number of rods equals to the number of lattice sites. Without loss of generality, we set the right-orientated rod corresponding to an occupied site and the left-orientated rod corresponding to an empty site (see in Fig. 3.2).

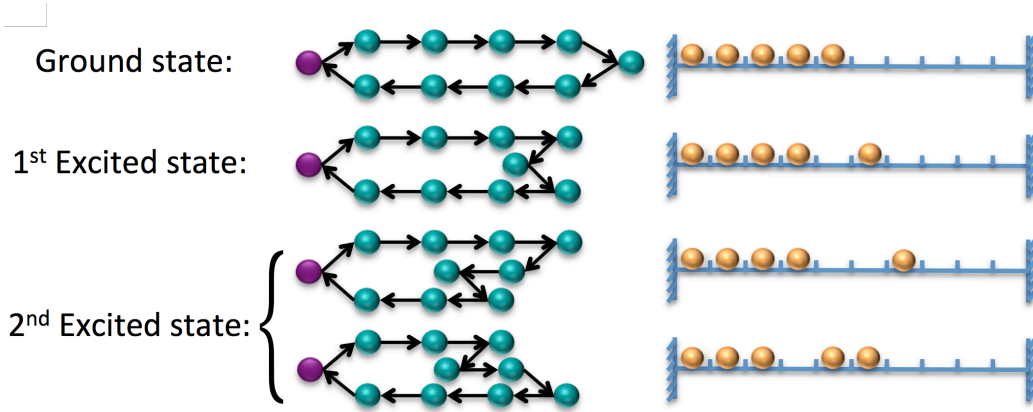


Figure 3.2: Illustration of the mapping of 1D pinned polymer loop to Fermionic particles on 1D lattice sites.

Here are some remarks for the mapping:

- The mapped particles are exclusive to each other. It is not possible for one lattice to be occupied by more than one particles. In other words, these particles are Fermions. This is because the rod points to either right or left.
- According to the looping condition Eq. (3.4), the total number of rods pointing to the right must be exactly $L/2$. Similarly, the total number of particles also must be exactly $L/2$:

$$\sum_{j=1}^L n_j = \frac{L}{2}. \quad (3.6)$$

Furthermore, the number of particles must be conserved for all possible configurations.

- The dynamics of a 1D polymer can be mapped to the particle hopping process on the 1D lattice. We leave the discussion of this part to Chapter 4.
- The mapping is essentially from a two-state system to a two-state system. One can also interpret the two states as spin up and spin down or any other two-state

systems. We use the particle-lattice interpretation in this thesis.

Rewriting the energy Eq. (3.3) in 1D we get

$$E = E_0 - Fa \sum_{i=1}^L \sum_{j=1}^i u_j. \quad (3.7)$$

Exchanging the summation order in Eq. (3.7) and utilizing the loop condition $\sum_{j=1}^L u_j = 0$ we obtain

$$E = E_0 + Fa \sum_{j=1}^L j u_j. \quad (3.8)$$

Let us look at the energy from the particle-lattice perspective. Substituting Eq. (3.5) into Eq. (3.8), we arrive at

$$E = \tilde{E}_0 + \Delta E \sum_{j=1}^L j n_j \quad (3.9)$$

where $\Delta E = 2Fa$ and $\tilde{E}_0 = E_0 - L(L+1)\Delta E/4$ is the irrelevant energy offset, which is interpreted as ground state energy. Eq. (3.9) can be reinterpreted as the summation energy of L lattice sites. When $n_j = 1$ (occupied site), we gain an energy of $j\Delta E$ and zero otherwise. One can clearly see that Eq. (3.9) is the energy of a system with $L/2$ fermions distributed over L equal energy levels $\Delta E, 2\Delta E, \dots, L\Delta E$. The lowest energy (ground state) corresponds to the configuration where the left half of the lattice is fully filled by particles, and the corresponding polymer picture is the fully stretched configuration. The correspondence of the 1st and the 2nd excited states are illustrated in Fig. 3.2.

The mapping from the polymer to the particle-lattice picture is very useful for searching the solution of equilibrium statistics. In the following subsections, we solve the 1D statistics using two different methods. The first one based on the grand canonical ensemble is an approximate solution with a simpler formalism, while the second one is the exact solution based on the canonical ensemble but a more complex formalism.

3.2.2 Grand canonical ensemble solution

The 1D particle-lattice system is in principle a canonical ensemble system since the total particle number is conserved to $L/2$. However, in order to directly use the known results of Fermi-Dirac statistics, we first release the constraint by allowing the particles to be exchanged with the reservoir at both sides of the lattice. Thus the grand canonical ensemble can be applied to the system. After that, we can reimpose the constraint using the Brownian bridge technique [160, 161]. We can obtain accurate values for the mean and variance of the position of each bead using this method.

The Fermi-Dirac statistics

As we have mentioned above, the particles on the lattice are fermions. One benefit of working in the grand canonical ensemble is that we can directly use the *Fermi-Dirac* distribution. Consequently, the probability of a lattice site being occupied can be written as

$$\mathbb{P}\{n_j = 1\} = \frac{1}{1 + \exp\left[\frac{\Delta E(j-\mu)}{k_B T}\right]}, \quad (3.10)$$

where μ is the chemical potential $\mu = (L + 1)/2$ obtained from the requirement that on average there are $L/2$ particles in the system. Accordingly, the probability that a lattice site is empty can be written as

$$\mathbb{P}\{n_j = 0\} = 1 - \mathbb{P}\{n_j = 1\}. \quad (3.11)$$

Next we define a dimensionless quantity which we call *dimensionless temperature*:

$$\tilde{T} = \frac{k_B T}{\Delta E} = \frac{k_B T}{2Fa} \quad (3.12)$$

In Fig. 3.3 we present an illustration of the *Fermi-Dirac* distribution at different \tilde{T} . When \tilde{T} is small, namely $Fa \gg k_B T$, the distribution exhibits a strong bias. The left half sites are more likely to be occupied and the right half sites are more likely to be empty. In the polymer picture, this means the orientation of the first half rods is biased in the direction of force, whereas the second half of rods are more probable to point against the force field. Physically, it means the pinned polymer in a strong force field is mostly stretched.

With Eq. (3.10), the mean and variance of the random variable n_j can be calculated straightforwardly as follows:

$$\langle n_j \rangle = \mathbb{P}\{n_j = 1\}, \quad (3.13a)$$

$$\text{var}[n_j] = \mathbb{P}\{n_j = 1\} \cdot \mathbb{P}\{n_j = 0\} - \langle n_j \rangle^2. \quad (3.13b)$$

The position of beads can be calculated from Eq. (3.2) and Eq. (3.5):

$$z_i = a \left(2 \sum_{j=1}^i n_j - i \right). \quad (3.14)$$

If we assume n_1, n_2, \dots, n_L are all mutually independent, then the mean and variance

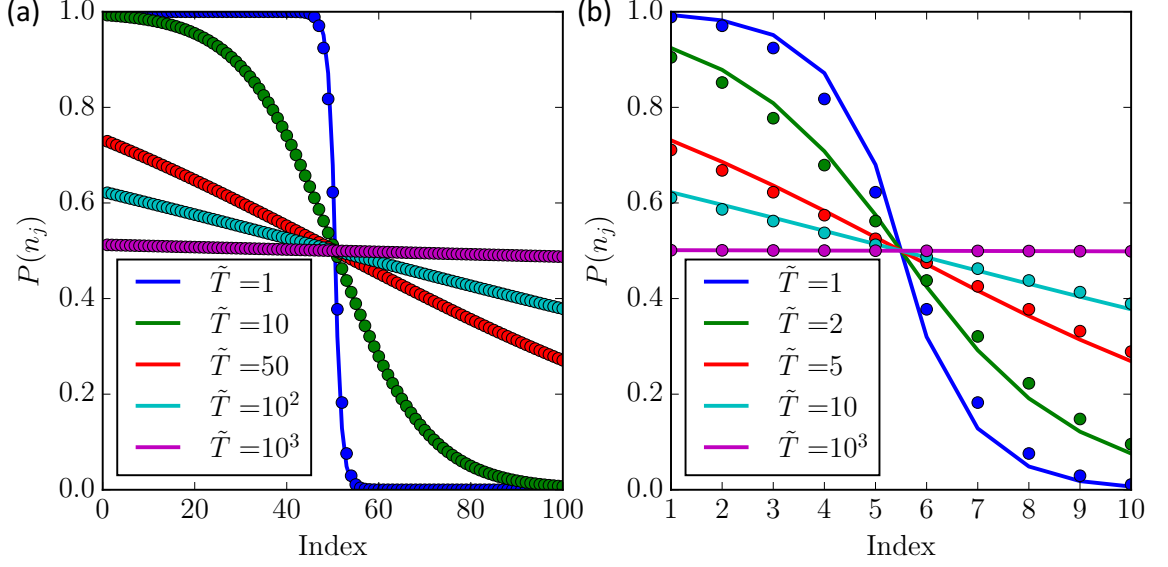


Figure 3.3: Fermi-Dirac distribution compared with the exact solution from the number partition theory. Solid lines are the exact solution while the dots are Fermi-Dirac approximations. Different dimensionless temperature is indicated by different colors as shown in the legend. (a) $L = 100$, (b) $L = 10$.

of bead position can be simply calculated as

$$\langle z_i \rangle = a \left(2 \sum_{j=1}^i \langle n_j \rangle - i \right), \quad (3.15a)$$

$$\text{var} [z_i] = 4a^2 \sum_{j=1}^i \text{var} [n_j] \quad (3.15b)$$

The results from the above equations can be compared to the Monte Carlo simulation (see Appendix B for details). We found that the formula works perfectly for mean bead position. However, significant error emerges for the variance of Eq. (3.15b). Notice that Eq. (3.15b) is monotonically increasing with the index i . We can try to use the simple symmetric argument that the $\text{var} [z_i] = \text{var} [z_{L-i}]$. The result with symmetric argument is shown in Fig. 3.4, which still differs significantly from the numerical result.

The reason for this mismatch is that the loop condition is fulfilled only on average by choosing of the chemical potential $\mu = (L + 1)/2$ in Eq. (3.10). We need to select from the possible trajectories that come back exactly to the starting point. In the following part, we will show how to solve this problem using the Brownian bridge technique.

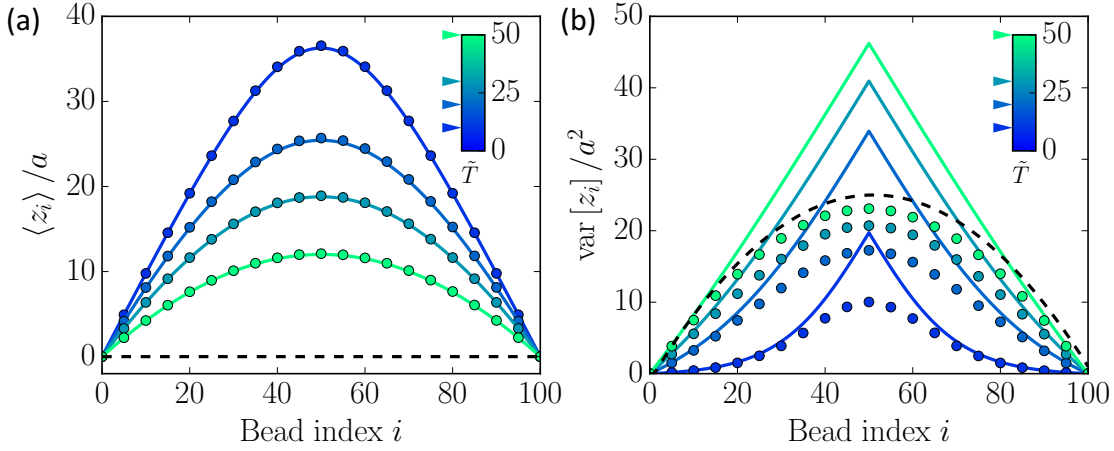


Figure 3.4: Mean and variance of the 1D pinned polymer bead positions. MC simulation results (dots) are compared with theoretical results (solid lines) Eq. 3.15. The length of the polymer loop $L = 10$. The black dash line indicates the case $\tilde{T} \rightarrow \infty$, i.e. no external force field.

The Brownian bridge condition

Let us consider the polymer loop as a random walk that returns to the origin point after L steps. This sort of random walk process is called the Brownian bridge [160, 161]. So each rod represents a random walk step. The segment connecting the k^{th} and the l^{th} bead with positions at z and z' corresponds to the propagator $\rho(z_l = z' | z_k = z)$. According to the Lindeberg-Feller central limit theorem [160], this propagator is Gaussian with the mean and variance equal to the sum of the mean and variance of all individual steps from k to l .

As we mentioned above, the grand canonical ensemble only ensures the loop condition on average. To solve the problem, we now impose the Brownian bridge condition so that every single trajectory fulfills the loop condition. The Brownian bridge can be formulated as follows:

$$\rho^L(z_i = z) = \frac{\rho(z_i = z | z_0 = 0) \rho(z_{L-i} = z | z_L = 0)}{\rho(z_L = 0 | z_0 = 0)}, \quad (3.16)$$

where $\rho(z_i = z)$ is the probability density function of finding the i^{th} bead at position z , $\rho(z_k = z | z_j = 0)$ are the propagators. Eq. (2.2) means that the probability density is calculated by requiring two pieces of random walk trajectory of length i and $L - i$ meet at position z on a condition that they belong to the same loop.

Notice that the propagators in Eq. (3.16) are Gaussian with the variance that is the sum of the variance of individual steps, i.e. Eq. (3.15b), so that $\rho^L(z_i = z)$ is also

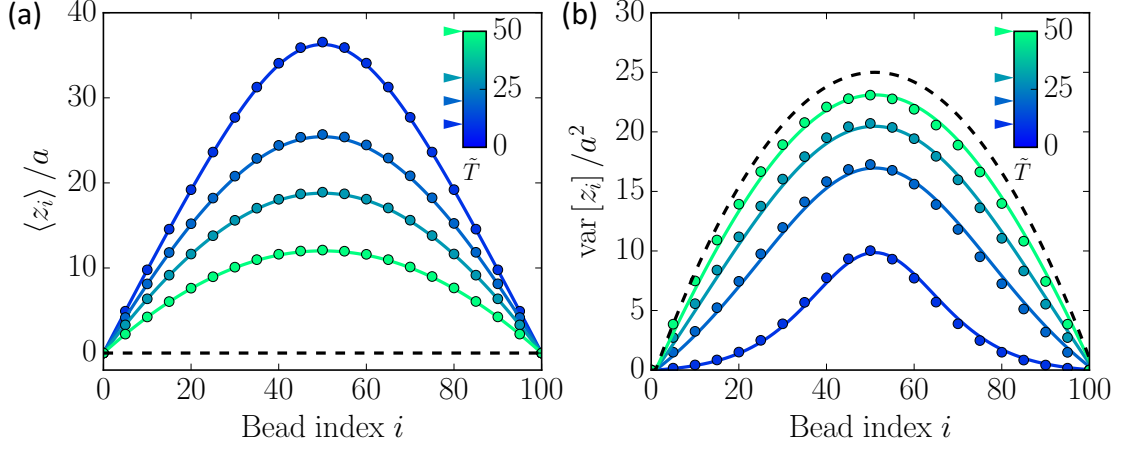


Figure 3.5: Mean and variance of the 1D pinned polymer bead positions. MC simulation results (dots) are compared with theoretical results (solid lines) Eq. 3.18. The length of the polymer loop $L = 10$. The black dash line indicates the case $\tilde{T} \rightarrow \infty$, i.e. no external force field.

Gaussian. Its variance is given by

$$\text{var}[z_i] = 4a^2 \frac{\sum_{j=0}^i \text{var}[n_j] \sum_{j=L-i}^L \text{var}[n_j]}{\sum_{j=0}^L \text{var}[n_j]}. \quad (3.17)$$

Plugging in Eq. (3.13b) and Eq. (3.15b) we can obtain the variance of bead position in the loop. For $\tilde{T} \gg 1$, we can obtain the close form expressions for mean and variance of bead position by converting the summations in Eq. (3.15a) and Eq. (3.17) to integral

$$\langle z_i \rangle = 2a\tilde{T} \ln \left[\frac{1 + \exp\left(\frac{L}{2\tilde{T}}\right)}{\exp\left(\frac{i}{2\tilde{T}}\right) + \exp\left(\frac{L-i}{2\tilde{T}}\right)} \right] \quad (3.18a)$$

$$\text{var}[z_i] = 2a^2\tilde{T} \frac{\sinh\left(\frac{L-i}{2\tilde{T}}\right) \sinh\left(\frac{i}{2\tilde{T}}\right)}{\sinh\left(\frac{L}{2\tilde{T}}\right) \cosh^2\left(\frac{L-2i}{4\tilde{T}}\right)} \quad (3.18b)$$

We have solved the mean and variance of bead position for 1D pinned polymer loop in an external force field by using the *Fermi-Dirac* statistics and re-enforcing the loop condition through the Brownian bridge technique. We can see from the above formulae that the $z_i - z_{L-i}$ symmetry is automatically satisfied. In Fig. 3.5, these results are compared with Monte Carlo simulation results. It is evident from the figure that a strong external force field leads to a stretched configuration and a small fluctuation of

the bead position. Excellent agreement with the Monte Carlo simulations is obtained. However, this method is not an exact solution. In the next subsection, we use the canonical ensemble to obtain the exact solution.

3.2.3 Canonical ensemble solution

In the particle-lattice picture, the system is a canonical ensemble system because of the conservation of particle number. In this section, we calculate the exact partition function using this ensemble. More interestingly, we show here the calculation can be recoded to a number partition problem. Exact results are obtained and compared with the results from the approximate approach above.

The number partition theory

Before the calculation of the exact partition function, let us discuss an interesting number partition problem that shares a lot of similarities with the former.

We consider a non-negative integer number K , which can be expressed into the summation of N non-negative integers:

$$K = \sum_{j=1}^N k_j \quad (3.19)$$

However, there is a constraint on the summation components $0 \leq k_1 \leq k_2 \leq \dots \leq k_N \leq M$. This kind of problem can be best visualized by the Young diagram [162], shown in Fig. 3.6. In the Young diagram, each row represents a integer number. The number

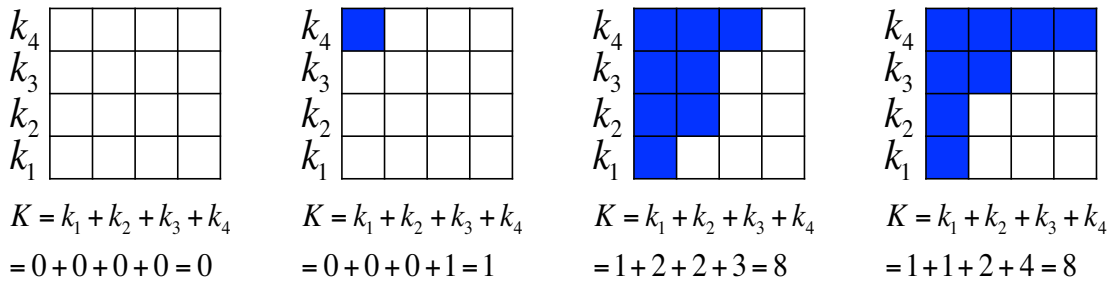


Figure 3.6: Some examples of the Young diagram.

of blue boxes means the value of the j^{th} integer. Starting from the bottom, because of the constraint, the diagram is non-decreasing.

The question is, given a certain integer K , how many different ways are there to partition it into N non-decreasing pieces $\{k_1, k_2, \dots, k_N\}$? For the simple cases, one can tell the answer immediately. For example, in the first two cases of Fig. 3.6, we

illustrate that there is only one way to partition integer 0 or 1 into 4 non-decreasing integers. However, this question in the general case is not intuitive. Fortunately, this problem is well studied by mathematicians. Let $g(M, N; K)$ denote the number of partitions of K with at most N parts, each of size at most M . Equivalently, these are the partitions whose Young diagram fits inside an $N \times M$ rectangle. Then we have the following generating function:

$$\Phi(q) := \sum_{K=0}^{MN} g(M, N; K) q^K = \binom{M+N}{N}_q \quad (3.20)$$

where q is an auxiliary number, and the notation at the right hand side of Eq. (3.20) is called q -binomial coefficient or Gaussian binomial coefficient. It is defined as

$$\binom{L}{N}_q := \frac{[L]_q!}{[L-N]_q! [N]_q!}, \quad (3.21)$$

and $[N]_q := 1 + q + q^2 + \dots + q^{N-1}$ is a q -number [162].

Exact partition function

Now, let us calculate the partition function of our pinned polymer in the particle-lattice picture. The partition function \mathcal{Z} of a canonical ensemble system with discrete energy can be written as:

$$\mathcal{Z}(T) = \sum_E g(E) \exp\left(-\frac{E}{k_B T}\right), \quad (3.22)$$

where $g(E)$ is the degeneracy of the microscopic states which have the same energy E . Once $g(E)$ is known, the partition function can be calculated straightforwardly.

Let us take a look at the energy of the system, i.e. Eq. (3.9). It is represented in the way of rod orientation u_j or occupation variable n_j . Here, we can use another way to represent the energy. In the particle-lattice picture, the system consists $N = L/2$ particles. So the energy can be rewritten as:

$$E = \tilde{E}_0 + \sum_{j=1}^N E_j, \quad (3.23)$$

where E_j is the energy of the j^{th} particle in the external force field. Again, \tilde{E}_0 is an unimportant constant energy offset. We denote the position of the j^{th} particle as x_j , which is an integer $x_j \in [1, L]$. Then we can write $E_j = x_j \Delta E$. Notice that, because of the exclusive condition, the sample space of the particle system is constrained in $\Omega = \{\mathbf{x} | 1 \leq x_1 < x_2 < \dots < x_N \leq L\}$.

Let us do a shift for the particle position by defining

$$k_j := x_j - j. \quad (3.24)$$

Now the constraint on x_j is transferred to $0 \leq k_1 \leq k_2 \leq \dots \leq k_N \leq N$, and the energy of the system can be rewritten as:

$$E = \hat{E}_0 + \Delta E \sum_{j=1}^N k_j = \hat{E}_0 + K \Delta E, \quad (3.25)$$

Again, \hat{E}_0 here is an unimportant constant energy offset, $\hat{E}_0 = \tilde{E}_0 + N(N+1)/2$. It is not difficult to find that the range of the energy is $\hat{E}_0, \hat{E}_0 + \Delta E, \dots, \hat{E}_0 + N^2 \Delta E$.

Now we are close to the number partition problem. As $K = \sum_{j=1}^N k_j$, we have the same type of constraint as in the number partition problem. Since the mapping from integer K to energy E is one-to-one, the degeneracy function $g(E)$ is exactly the number of ways of partitioning the integer K . Furthermore, by denoting $q := \exp(-\Delta E/k_B T)$, we have

$$\begin{aligned} \mathcal{Z}(T) &= \sum_E g(E) \exp\left(-\frac{E}{k_B T}\right) \\ &= \exp\left(-\frac{\hat{E}_0}{k_B T}\right) \sum_{K=0}^{N \times N} g(N, N; K) q^K \\ &= \exp\left(-\frac{\hat{E}_0}{k_B T}\right) \binom{L}{N}_q. \end{aligned} \quad (3.26)$$

With the exact partition function Eq. (3.26), the equilibrium distribution P^e can be calculated straightforwardly:

$$P^e \propto \frac{1}{\mathcal{Z}(T)} \exp\left(-\frac{E}{k_B T}\right) = \frac{q^K}{\binom{L}{N}_q}. \quad (3.27)$$

We can see here the offset energy is not in the distribution function. That is why we have commented that it is not important. In principle, one more constant pre-factor should be added to Eq. (3.27), which can be fixed by the normalization condition $\sum_{K=0}^{N^2} P^e = 1$. However, this constant is not important for our discussions, so we just keep it in the form of Eq. (3.27).

With Eq. (3.26) and Eq. (3.27), in principle, one can calculate any kind of equilibrium quantities. Here, we calculate the probability distribution of rod orientation in order to compare with our previous approach based on the grand canonical ensemble.

Exact probability distribution of the rod orientation

The probability distribution of the rod orientation is equivalent to the probability distribution of the lattice site occupation. Previously, we have employed the *Fermi-Dirac* distribution. In this subsection, we calculate the exact distribution of $\mathbb{P}\{n_j = 1\}$ to show how accurate the *Fermi-Dirac* distribution is.

We first rewrite the equilibrium distribution (Eq. (3.27)) in the coordinate of particle position:

$$P^e(x_1, x_2, \dots, x_N) = q^{-\frac{N(N+1)}{2}} \binom{L}{N}_q^{-1} \prod_{i=1}^N q^{x_i}. \quad (3.28)$$

Now let us denote $P_i(x)$ as the probability that the i^{th} particle is at position x in equilibrium. Then $P_i(x)$ can be calculated as

$$\begin{aligned} P_i(x) &= \sum_{1 \leq x_1 < \dots < x_{i-1} \leq x-1} P^e(x_1, x_2, \dots, x_N) \\ &\quad \times \sum_{x < x_{i+1} < \dots < x_N \leq L} P^e(x_1, x_2, \dots, x_N) \\ &= q^{(N+1-i)(x-i)} \binom{x-1}{i-1}_q \binom{L-x}{N-i}_q / \binom{L}{N}_q. \end{aligned} \quad (3.29)$$

Finally, the probability that the j^{th} site is occupied can be calculated as

$$\mathbb{P}\{n_j = 1\} = \sum_{i=1}^N P_i(x = j) \quad (3.30)$$

Eq. (3.30) means the probability that one site is occupied is the sum of the probability that it is occupied by any of the N particles. Plugging in Eq. (3.29), one can obtain the exact occupation probability distribution. The exact result is compared with the *Fermi-Dirac* distribution in Fig. 3.3. As we can see in the figure, the discrepancy is quite small. It is only noticeable for a small lattice size at very strong external force field (Fig. 3.3 (b)). So the *Fermi-Dirac* distribution is actually a very accurate approximation.

In this section, we have solved the equilibrium statistics of the pinned polymer loop model in 1D. Utilizing the mapping from the polymer to a particle-lattice system, we solve the statistics by two different approaches. The first one employs the *Fermi-Dirac* distribution and the Brownian bridge technique. However, it is an approximate method. The second method based on canonical ensemble and number partition theory is an exact solution. The exact results are compared with the first method as well as the Monte Carlo simulations. Our theory matches very well to the simulation results. In the next section, we extend our theory to the 3D system.

3.3 Equilibrium statistics in 3D

In 3D, the equilibrium statistics of the pinned polymer loop model can be calculated using the grand canonical ensemble and Brownian bridge condition. The orientation of rods have two more degree of freedom in 3D. As shown in section 3.1, the external force is assumed in the z direction. Let us use the spherical coordinates to describe the polymer system. We denote θ_j as the angle between the j^{th} rod and the z -axis, and ϕ_j as the rotational angle along z -axis. Then the loop condition along the force direction can be written as

$$\sum_{j=1}^L \cos \theta_j = 0. \quad (3.31)$$

Using the above condition, the energy of the 3D polymer Eq. (3.3) can be rewritten as

$$E = E_0 + Fa \sum_{j=1}^L j \cos \theta_j. \quad (3.32)$$

In the following subsections, we first derive the partition function and then calculate the mean and variance of the position of the three-dimensional beads.

3.3.1 Partition function

To calculate the equilibrium statistics of a 3D bead-rod system, we use the approach of grand canonical ensemble combined with the Brownian bridge condition. The grand canonical ensemble partition function can be written as:

$$\mathcal{Z} = \prod_{j=1}^L \mathcal{Z}_j = \prod_{j=1}^L \int_0^{2\pi} d\phi \int_0^\pi \exp\left(-\frac{(j-\mu) \cos \theta \Delta E}{k_B T}\right) \sin \theta d\theta. \quad (3.33)$$

Here, $\mu = (L+1)/2$ is the chemical potential, the same as in 1D. However, $\Delta E = Fa$ is different from the 1D case by a factor of 2. Again, let us define the *dimensionless temperature*:

$$\tilde{T} = \frac{k_B T}{\Delta E} = \frac{k_B T}{Fa}. \quad (3.34)$$

There is also a factor of 2 compared to the dimensionless temperature in 1D.

The integration in Eq. (3.33) can be performed to obtain

$$\mathcal{Z}_j = \frac{\tilde{T} \sinh \frac{j-\mu}{\tilde{T}}}{j-\mu}. \quad (3.35)$$

Thus, the mean and variance of the j^{th} rod orientation $u_{j,z} = \cos \theta_j$ can be directly

calculated as

$$\begin{aligned}\langle \cos \theta_j \rangle &= \tilde{T} \partial_\mu \ln \mathcal{Z}_j = \coth \frac{\mu - j}{\tilde{T}} - \frac{\tilde{T}}{\mu - j}, \\ \text{var} [\cos \theta_j] &= \tilde{T}^2 \partial_\mu^2 \ln \mathcal{Z}_j = \frac{\tilde{T}^2}{(j - \mu)^2} - \text{csch}^2 \frac{j - \mu}{\tilde{T}}.\end{aligned}\quad (3.36)$$

Notice that, because of the $x - y$ symmetry, the average projection for x and y directions are zero: $\langle u_{j,x} \rangle = \langle u_{j,y} \rangle = 0$. The second moment of these component can be calculated as

$$\langle u_{j,x}^2 \rangle = \langle u_{j,y}^2 \rangle = (1 - \langle \cos^2 \theta_j \rangle) / 2 \quad (3.37)$$

The above equations give the statistical properties of individual rod orientation. In the next subsection, we will use the Brownian bridge technique to calculate the mean and variance of bead position.

3.3.2 Mean and variance of the bead position

In the case of 3D pinned polymer, according to Lindeberg-Feller central limit theorem [160, 161], the corresponding random walk is a multi-variate Gaussian process. It can be factorized into the product of three Gaussian processes, each corresponding to a coordinate axis. Let us first discuss it in the z direction, i.e. the direction along the force field. The propagator in the z direction $\rho(z_k = z | z_0 = 0)$ is Gaussian with the following mean and variance:

$$\begin{aligned}\langle z_k \rangle &= a \sum_{j=1}^k \langle \cos \theta_j \rangle, \\ \sigma_{0 \rightarrow k, z}^2 &= a^2 \sum_{j=1}^k \text{var} [\cos \theta_j].\end{aligned}\quad (3.38)$$

Finally, by imposing the Brownian bridge condition similar to Eq. (3.17), the variance of bead position can be written as

$$\text{var} [z_k] = a^2 \frac{\sum_{j=0}^k \text{var} [\cos \theta_j] \sum_{j=L-k}^L \text{var} [\cos \theta_j]}{\sum_{j=0}^L \text{var} [\cos \theta_j]}.\quad (3.39)$$

The analytical results above are compared with the 3D Monte Carlo simulations (see Section 2.3). We can see in Fig. 3.7 that an excellent agreement between the theory and the simulation is obtained.

Now let us discuss the directions perpendicular to the force direction. By symmetry arguments, we can immediately conclude that the statistics in x and y directions are identical. In addition, the mean position in both directions should vanish because

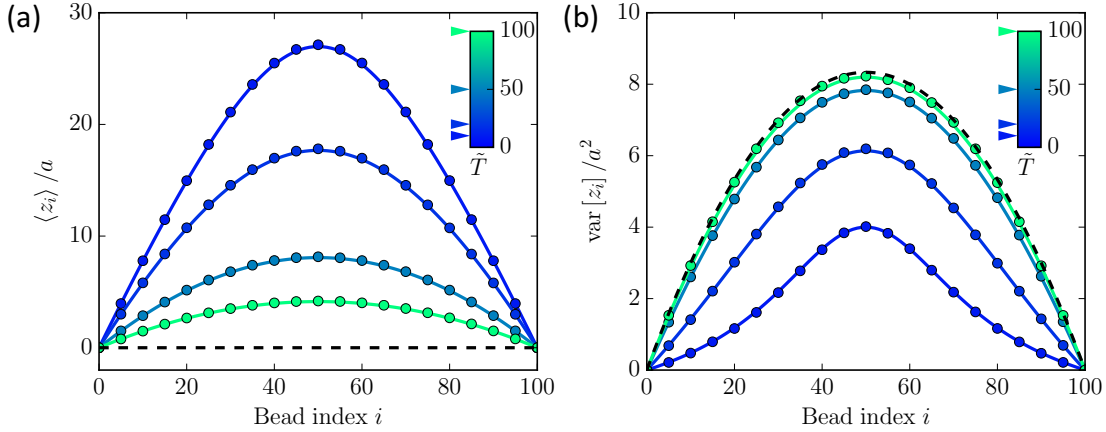


Figure 3.7: Mean and variance of the bead position in the direction along the force field. Solid lines are theory and dots are Monte Carlo simulation results. The black dash line indicates the case $\tilde{T} \rightarrow \infty$, i.e. no external force field.

there is no bias. We can write this as

$$\langle x_k \rangle = \langle y_k \rangle = 0. \quad (3.40)$$

On the other hand, using Eq. (3.37), the variance of x and y components of the j^{th} rod orientation can be written as

$$\text{var}[u_{j,x}] = \text{var}[u_{j,y}] = \langle u_{j,x}^2 \rangle - \langle u_{j,x} \rangle^2 = (1 - \langle \cos^2 \theta_j \rangle) / 2 \quad (3.41)$$

Again, by imposing the Brownian bridge condition similar to Eq. (3.39), the variance of x and y components of the bead position can be obtained. It is worth mentioning here that the variance in x and y directions are different from the variance in z direction. This is shown in Fig. 3.8 where our theory is compared to the Monte Carlo simulations.

3.3.3 The pairing of loops

In fission yeast, the homologous chromosomes are appearing in pairs during nuclear oscillation, which means there are two mechanically identical chromosomes. Biologically, recombination occurs during nuclear oscillation. It is essential for homologous chromosomes to come close spatially in order to recombine, which is done by a pairing process. The biological facts motivate us to consider a pair of polymer loops pinned at the same point. To understand the pairing process, it is meaningful to study the statistical distance between two “homologous” beads (Fig. 1.4) belonging to two identical

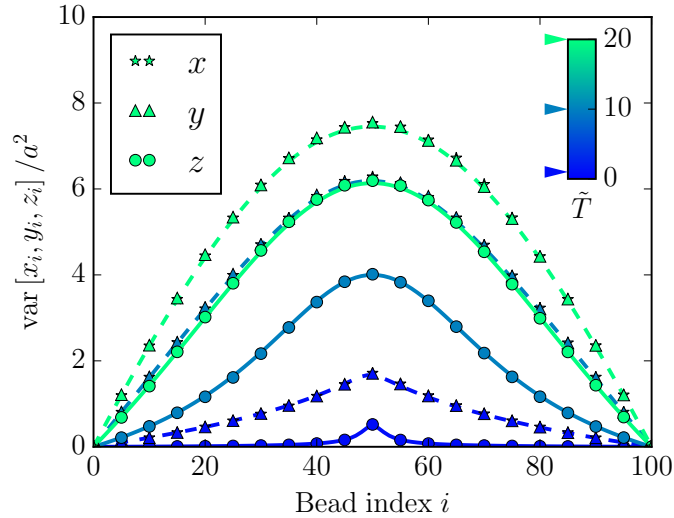


Figure 3.8: Comparison of fluctuations in x , y and z directions. Symbols denote the Monte Carlo simulations. Circles show the fluctuations along the z axis, whereas stars and triangles along x and y axis respectively. Colors correspond to different dimensionless temperatures. Solid and dash lines are theoretical predictions for fluctuations along and orthogonal to the force field, respectively.

polymer loops. Fig. 3.9 is the schematic diagram of this case. Due to the symmetry reason and no excluded volume effect in the model, the three-dimensional mean distance between two corresponding beads is zero. The statistical distance is defined as the square root of its variance with the variance calculated as:

$$\text{var}[\mathbf{d}_i] = \text{var}[\mathbf{r}_i - \mathbf{r}'_i] = 2\text{var}[\mathbf{r}_i] = 2(\text{var}[x] + \text{var}[y] + \text{var}[z]). \quad (3.42)$$

In Fig. 3.10 we show that the statistical distance varies with the dimensionless temperature, the later being the inverse measure of the external force field strength. We can see from the figure that strong force field reduces the statistical distance for all beads and thus facilitates pairing. BD simulations are performed and results are found to match our theory.

3.3.4 Intersecting loops

The paring process of homologous chromosomes connects two homologues by proteins along their lengths [163]. However, it is hypothesized that some connections between homologues could have been formed before the pairing of other parts. One of the hypotheses is that the centromeres of homologues are still bond together during the nuclear oscillation. In this subsection, we discuss a pair of pinned polymer loops with an additional connection in the middle part of the loop. The schematic diagram of the

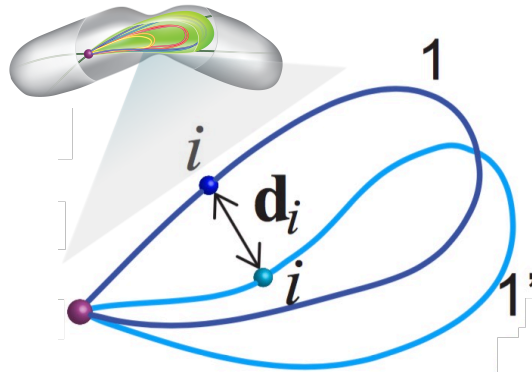


Figure 3.9: A Pair of polymer loops pinned at the same point representing the homologs. The distance of a pair of loci is illustrated as d_i .

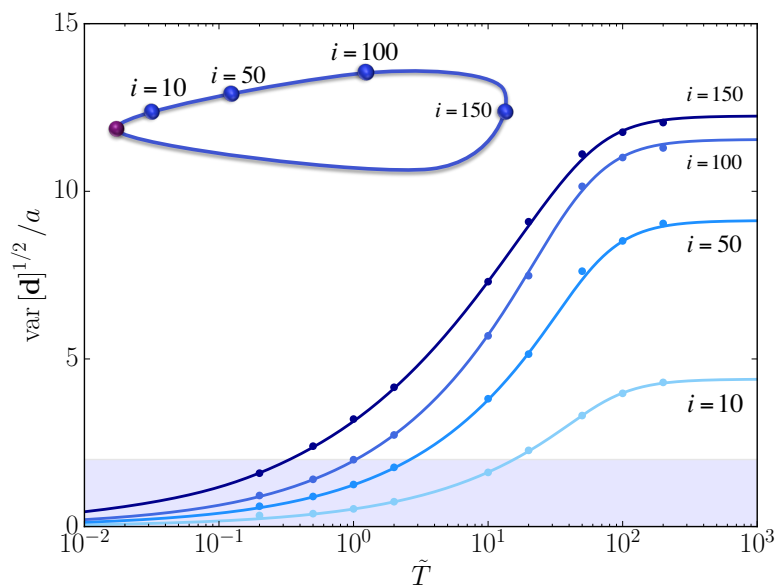


Figure 3.10: The distance between corresponding loci of polymer pair loops varies with the dimensionless temperature. Different curves indicate different locations along the loop. The shaded region represents the pairing distance. Dots are BD simulation data and solid lines are results from our theory. Inset is a sketch of the observing loci along the chromosome. Here $L = 300$, $k_B T = 1$.

intersecting loops is shown in Fig. 3.11. The pair of polymer loops (denoted by 1 and

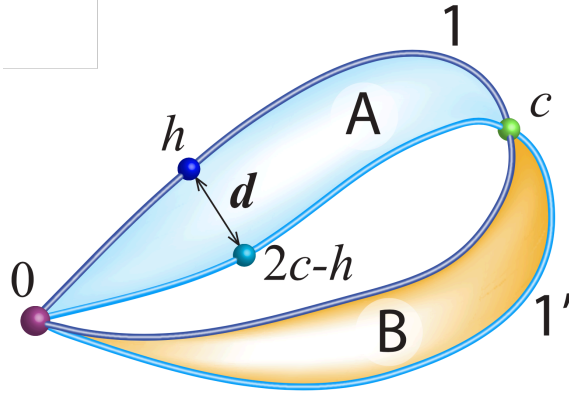


Figure 3.11: The sketch of two intersecting loops 1 and 1' which are connected at one additional bead with index c . Shaded regions indicate the redefined loops A and B. The distance \mathbf{d} between two homologous beads h and $2c - h$ is illustrated.

1') are pinned at the same point 0 with an additional constraint at some intermediate bead position (indexed by c , where $0 < c < L$). However, bead c is not pinned so that it can still move around.

In order to solve this problem, we redefine the loops as shown in Fig. 3.11. The loop A starts at the pinned point, continues along the loop 1, to the constraint point c and then returns to the origin along the loop 1' by the path of the same length as shown in Fig. 3.11 shaded with cyan color in between. The loop B is shown in Fig. 3.11 shaded with orange color in between. We are interested in the distance \mathbf{d} between two homologous beads as shown in the figure. We denote the first bead position with index h , then the other one can be denoted by $2c - h$ considering the loop A.

To calculate the probability density function (PDF) of $\mathbf{d} := \mathbf{r}_h - \mathbf{r}_{2c-h}$, which is denoted as $\rho(\mathbf{d})$, let us first calculate the joint positional PDF $\rho_{h,2c-h}(\mathbf{r}_1, \mathbf{r}_2)$. We denote the propagator as $\rho_{k \rightarrow j}(\mathbf{r}_1 | \mathbf{r}_2) = \rho(\mathbf{r}_k = \mathbf{r}_1 | \mathbf{r}_j = \mathbf{r}_2)$. The propagator is a multivariate Gaussian function with a mean and variance summing up by path steps. We can apply the similar Brownian bridge condition, obtaining

$$\rho_{h,2c-h}(\mathbf{r}_1, \mathbf{r}_2) = \frac{\rho_{0 \rightarrow h}(\mathbf{r}_1 | 0) \rho_{h \rightarrow 2c-h}(\mathbf{r}_1 | \mathbf{r}_2) \rho_{0 \rightarrow 2c-h}(\mathbf{r}_2 | 0)}{\rho_{0 \rightarrow 2c}(0 | 0)}. \quad (3.43)$$

Then the PDF $\rho(\mathbf{d})$ can be calculated as

$$\rho(\mathbf{d}) = \int \int d\mathbf{r}_1 d\mathbf{r}_2 \delta(\mathbf{d} - (\mathbf{r}_1 - \mathbf{r}_2)) \rho_{h,2c-h}(\mathbf{r}_1, \mathbf{r}_2), \quad (3.44)$$

Without evaluating the integrals in Eq. (3.44), one can conclude that $\rho(\mathbf{d})$ is Gaussian because $\rho_{h,2c-h}(\mathbf{r}_1, \mathbf{r}_2)$ is Gaussian. It is not difficult to obtain the mean distance

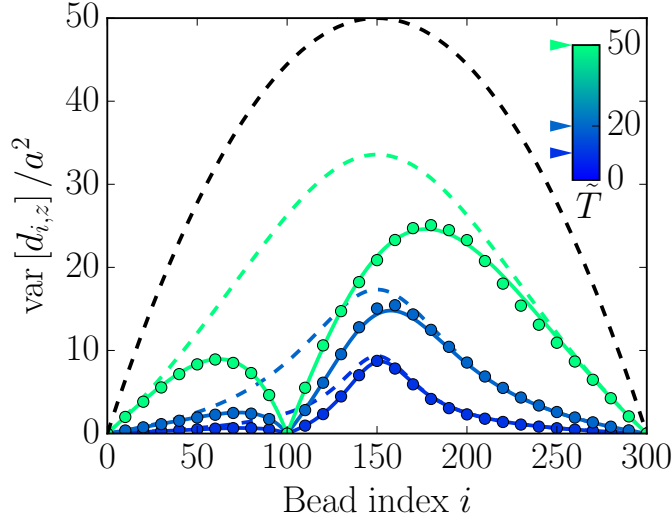


Figure 3.12: Variance of the distance between pinned polymer loops with an additional constraint. The constraint is located at the bead with index $c = 100$. Circles denote the simulation results while the solid lines represent the theory. The dashed lines show the variance of the unconstrained case with different color indicates different dimensionless temperature. The black dashed line shows the limit of unconstrained force-free Brownian bridge.

$\langle \mathbf{d} \rangle = \mathbf{0}$ because of symmetry and no excluded volume effect. The variance can be calculated in the same way as Section 3.3.2. For example, the z -component variance is

$$\text{var}[d_z] = 2 \frac{\sigma_{0 \rightarrow h,z}^2 \sigma_{h \rightarrow c,z}^2}{\sigma_{0 \rightarrow c,z}^2}, \quad (3.45)$$

where each variance is calculated according to Eq. (3.36). The result compared with simulations is shown in Fig. 3.12. We see that fluctuations of the distance is reduced globally with the additional constraint point compared to the unconstrained case.

3.3.5 Excluded volume effect

In this subsection, we discuss the influence of excluded volume effects on to the statistics of the polymer loops. To do this, we resort to the BD simulations, add the Lennard-Jones interactions in the model (see section 2.2), and compare the results to the case without excluded volume.

In particular, in Fig. 3.13, we compare the simulation results of mean and variance of bead position along the force field with excluded volume effect to the analytical results without excluded volume effect. In general, the polymer loop with excluded volume in a force field is more elongated than in the case without excluded volume.

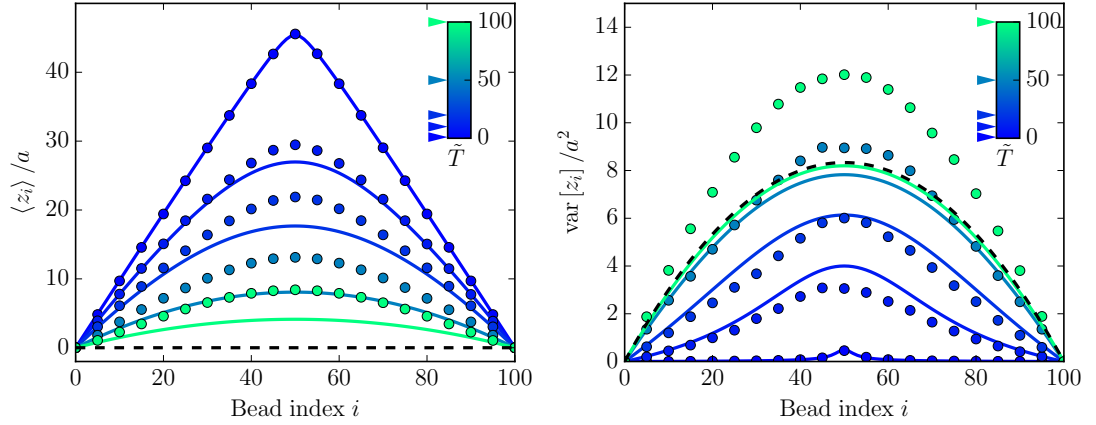


Figure 3.13: Mean and variance of the bead position in the direction along the force field. Solid lines are the theory without excluded volume effect, dots are Monte Carlo simulation results with excluded volume effect. The black dash line corresponds to the theory of no external force field case. Different cases of external forces are indicated by different colors shown in the legend.

However, the excluded volume effect is minor if the force field is strong and the polymer is almost fully stretched. The effect of excluded volume on the position fluctuations is interesting. In weak external force field, the polymer loop is in a coiled configuration, and we observe that the excluded volume amplifies the fluctuation of bead position. In contrast, the fluctuations are reduced by the excluded volume effect in a moderate external force field. In strong external force field, the excluded volume effect is negligible.

The excluded volume effect on different directions is shown in Fig. 3.14. As we can see in the figure, the excluded volume increases the fluctuation of the bead position perpendicular to the force direction, even in a strong external force field. These results are expected. Because of the excluded volume effect, it is not possible for two beads to overlap. Beads become more “excited” under the Lennard-Jones interactions when they come close enough.

To summarize, in Section 3.3, we discussed the three-dimensional pinned polymer loop model and its equilibrium statistics. The mean and variance of each bead position are calculated using the grand canonical ensemble combined with Brownian bridge technique. Fluctuations of distance between corresponding beads of pinned polymer pair loops are calculated analytically to quantify the pairing process. All theoretical results are verified by simulations. In addition, by discussing the case of two intersecting polymer loops, we find that the additional constraint helps to reduce the fluctuations, thus facilitate the pairing process. Finally, the influence of excluded volume effect is discussed. We found that the excluded volume reduces the fluctuation

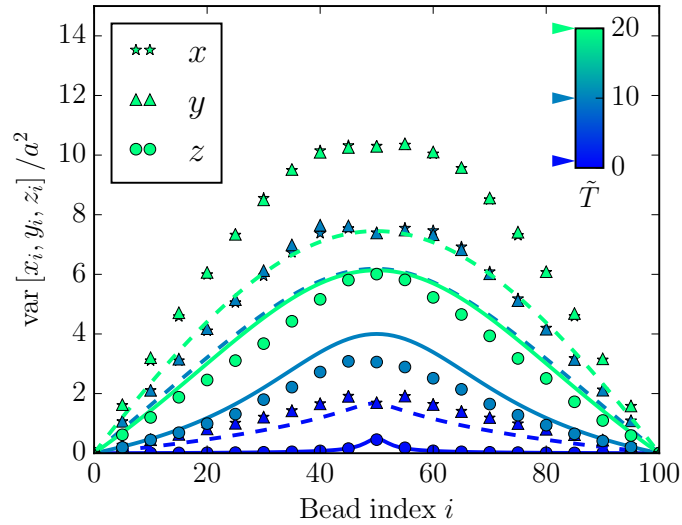


Figure 3.14: Comparison of the fluctuations in x , y and z directions. Solid and dash lines are theoretical predictions for fluctuations along and orthogonal to the force field without excluded volume effect, respectively. Symbols denote the Monte Carlo results with excluded volume effect. Different cases of dimensionless temperature are indicated by different colors shown in the legend.

along the force direction when the external force field is moderate and amplifies the fluctuation when the polymer loop is in a coiled configuration. In the next section, we use the theory of equilibrium statistics to quantify the shape of polymer loops in an external force field.

3.4 Characterizing the shape of pinned polymer loops

In Fig. 1.3, we have shown the fluorescent labeled chromosomes during nuclear oscillation. Experimentally, it is possible to measure the shape of the chromosomes, which is believed to be an important factor for nuclear oscillations in fission yeast. For example, it is reported in [11] that an elongated nucleus promoted accumulation of the LinE component Rec25, which could in turn promote recombinatory pathways, leading to the accumulation of irresolvable recombination intermediates at the end of meiotic prophase. So it is meaningful to characterize the shape of the chromosomes quantitatively.

In this section, we introduce several indicators commonly used to quantify the shape of steady state chromosomes, which is modeled by the pinned polymer loops. The three-dimensional gyration tensor, asphericity and the nature of asphericity are discussed. The simulation results are compared with the theory based on preceded sections.

3.4.1 The gyration tensor

Before explaining the shape of the pinned polymer loops, let us first have a look at the simulation results for several typical cases. We show in Fig. 3.15 the segment density distribution of a 3D pinned polymer loop projected in the 2D $x - z$ plane. The upper panel shows the marginal distribution of density along the force direction, while the right panel shows the marginal distribution of density perpendicular to the force direction. The red lines represent the theoretical predictions which we will discuss next.

In section 3.3, we calculated the mean and variance of the bead position in 3D. When the dimensionless temperature is not too small ($\tilde{T} \gg 1$), the distribution of the bead position can be considered as Gaussian. We thus have

$$p(z_i) = \frac{1}{\sqrt{2\pi\text{var}[z]_i}} \exp\left(-\frac{(z_i - \langle z_i \rangle)^2}{2\text{var}[z]_i}\right), \quad (3.46a)$$

$$p(x_i) = \frac{1}{\sqrt{2\pi\text{var}[x]_i}} \exp\left(-\frac{(x_i - \langle x_i \rangle)^2}{2\text{var}[x]_i}\right). \quad (3.46b)$$

Then the marginal particle density function can be calculated as

$$P(z) = \frac{1}{L} \sum_{i=1}^L p(z_i), \quad (3.47a)$$

$$P(x) = \frac{1}{L} \sum_{i=1}^L p(x_i). \quad (3.47b)$$

Substituting the mean and variance we obtained in section 3.3, the theoretical results shown by red lines in Fig. 3.15 can be obtained.

Although the density profile of monomers can be calculated as Eq. (3.47), the intuition of the polymer shape is still unclear. In order to quantify the shape, we calculate the 3D gyration tensor of the polymer, which is defined as following:

$$\mathbf{Q} = \begin{bmatrix} Q_{xx} & Q_{xy} & Q_{xz} \\ Q_{yx} & Q_{yy} & Q_{yz} \\ Q_{zx} & Q_{zy} & Q_{zz} \end{bmatrix} \rightarrow \begin{bmatrix} \lambda_x^2 & 0 & 0 \\ 0 & \lambda_y^2 & 0 \\ 0 & 0 & \lambda_z^2 \end{bmatrix} \quad (3.48)$$

where the elements of the \mathbf{Q} tensor Q_{mn} can be written as

$$Q_{mn} = \frac{1}{L} \sum_{i=1}^L (r_m(i) - r_m^{CM})(r_n(i) - r_n^{CM}), \quad (3.49)$$

with $m, n \in \{x, y, z\}$ and r^{CM} is the center of mass position. The arrow in Eq. (3.48)

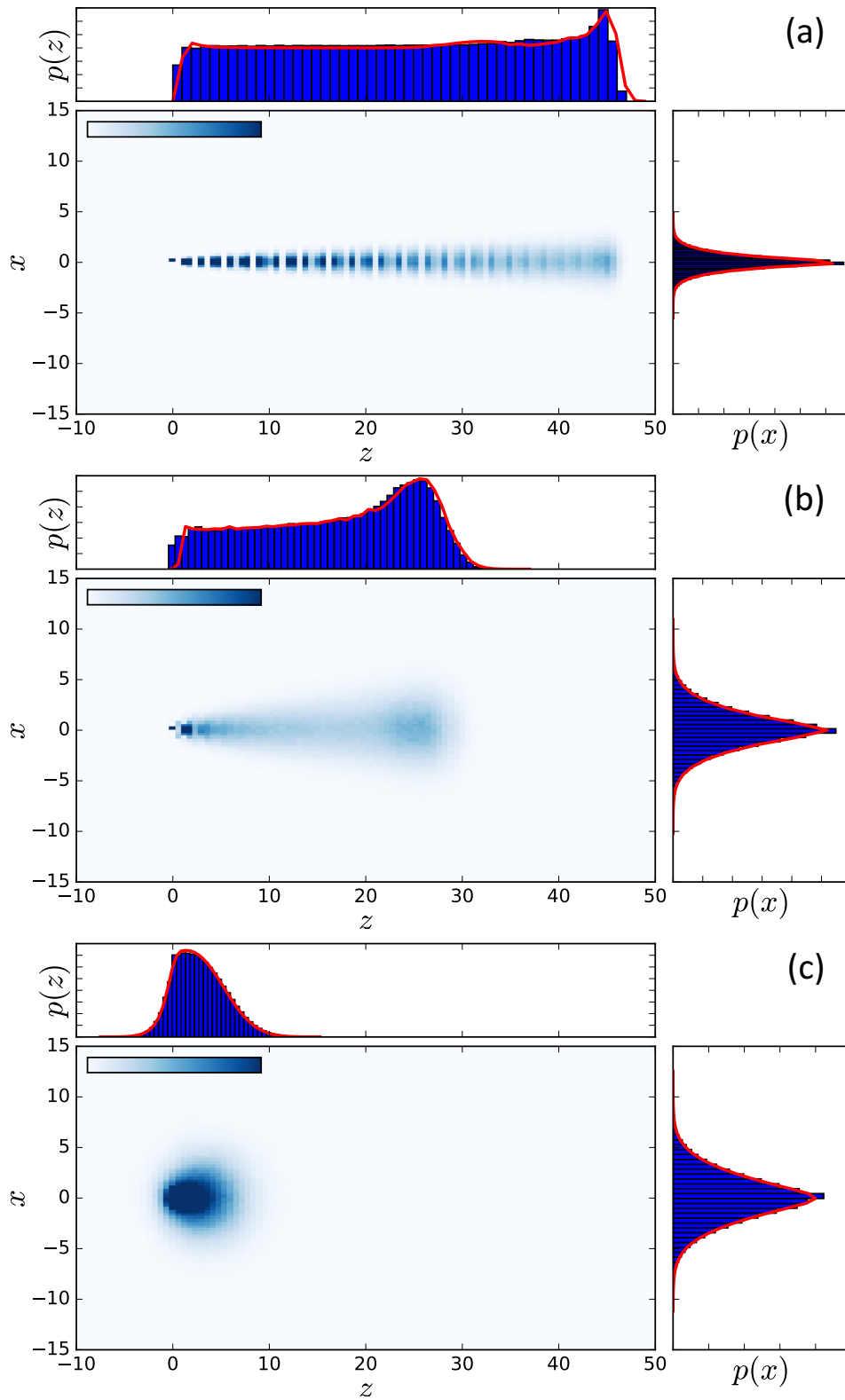


Figure 3.15: The density distribution of pinned polymer shape indicated by the color map for (a) strong external force field with $F = 1$, (b) moderate external force field with $F = 0.1$, (c) weak external force field with $F = 0.01$. Other parameters are set as following $a = 1$, $k_B T = 1$, $L = 100$. See more explanations in the main text.

indicates the diagonalization, and λ_x^2 , λ_y^2 , λ_z^2 represent the three non-negative eigenvalues of the gyration tensor. Physically, the intuition of the three eigenvalues can be interpreted as the magnitude of three principal axes of a fitted ellipsoid enclosing the polymer loops. For convenience, we order them by $\lambda_x^2 \leq \lambda_y^2 \leq \lambda_z^2$.

Based on the gyration tensor, the first shape indicator introduced here is the gyration radius of the polymer, which is defined and can be calculated as following:

$$R_g^2 := \frac{1}{L} \sum_{i=1}^L (\mathbf{r}_i - \mathbf{r}_{CM})^2 = \lambda_x^2 + \lambda_y^2 + \lambda_z^2 \quad (3.50)$$

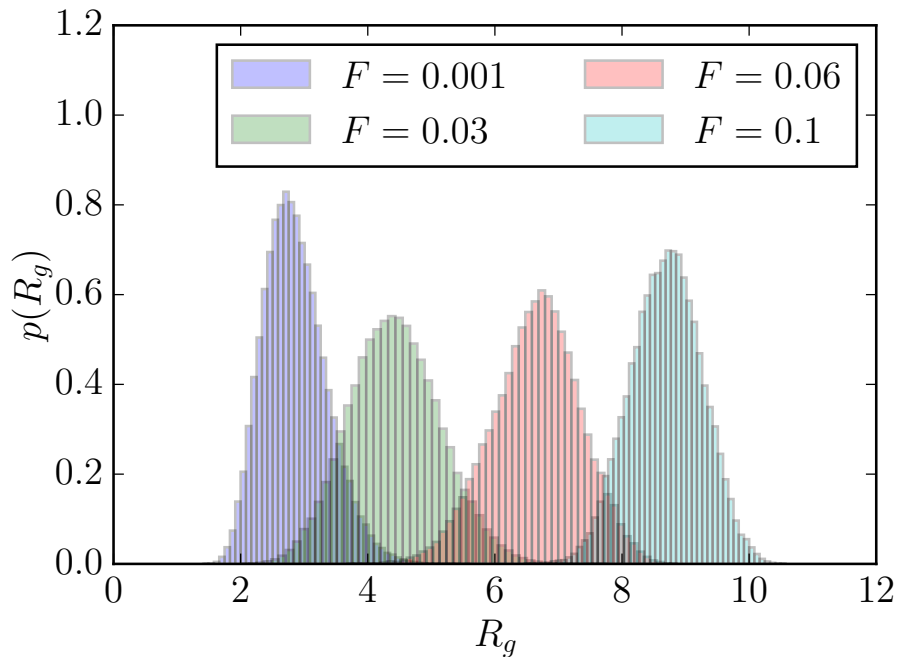


Figure 3.16: The distribution of gyration radius of pinned polymer loop under different strength of external force field. $L = 100$, $k_B T = 1$.

In Fig. 3.16, we show the distribution of the gyration radius under several force fields. Interestingly, we can see that the height of the distribution varies non-monotonically with the strength of the external force. In other words, the gyration radius is more fluctuating and distributed in a broader regime under a moderate force field. The underlying reason for this non-monotonic behavior is not clear yet. The looping geometry of the polymer might play a role since the non-monotonic behavior disappears once we cut the pinned polymer loop at the middle and turn it into two pinned polymer chains (data not shown here).

In next subsection, we introduce two more descriptors of the polymer shape, which is the asphericity and the nature of asphericity.

3.4.2 Asphericity and the nature of asphericity

The asphericity and the nature of asphericity are two descriptors that are commonly used to quantify the shape of the polymer. The definition of them is based on the gyration tensor [85]. More specifically, the asphericity is defined by

$$\Delta = \frac{3}{2} \frac{\text{Tr}\hat{Q}^2}{(\text{Tr}Q)^2}, \quad (3.51)$$

where $\hat{Q}_{ij} = Q_{ij} - \delta_{ij}\text{Tr}Q/3$. The nature of asphericity is given by

$$\Sigma = \frac{4 \det \hat{Q}}{\left(\frac{2}{3}\text{Tr}\hat{Q}^2\right)^{3/2}}. \quad (3.52)$$

However, in order to compare the shape of the pinned model with that described in the literature [85, 164], we adopt the parameter $\rho = 2\sqrt{\Delta} \in [0, 2]$ and $\theta = \arccos \Sigma/3 \in [0, \pi/3]$. The physical interpretation of these parameters is illustrated in Fig. 3.17 (a). Basically, $\rho = 0$ corresponds to a fully spherical object while $\rho = 2$ means the shape of the object is rod-like, and θ measures whether the object is prolate or oblate.

As we can see from Fig. 3.17, the shape of the pinned polymer loop is spread over a sickle-shaped area. In addition, the prolate and elongated shape is preferred no matter the external force is strong or not. The diagrams we found here are similar to those of semi-flexible unpinned polymer loops in [85].

In this section, we introduce several quantitative shape descriptors of a pinned polymer loop based on the 3D gyration tensor. The theory of segment density distribution was shown and compared to the Monte Carlo simulation data and a good consistency is obtained. In the future, we can use the theory here to quantify the shape of chromosomes from the experimental data.

3.5 Summary

In this chapter, we discussed the equilibrium statistics of pinned polymer loops in an external force field, which is used as the model for chromosomes in meiotic fission yeast.

We first solved the statistics of the polymer configuration in an idealized 1D model. A technique which combines the *Fermi-Dirac* statistics and Brownian bridge condition was introduced to solve the problem in *grand* canonical ensemble. The solution found was compared to the exact solution, which can be obtained after utilizing the analogy to a number partition problem. However, we found that the results from Brownian bridge technique are quite accurate while the exact solution is quite cumbersome for later calculations. Thus the first approach is preferred. Using these results, we are

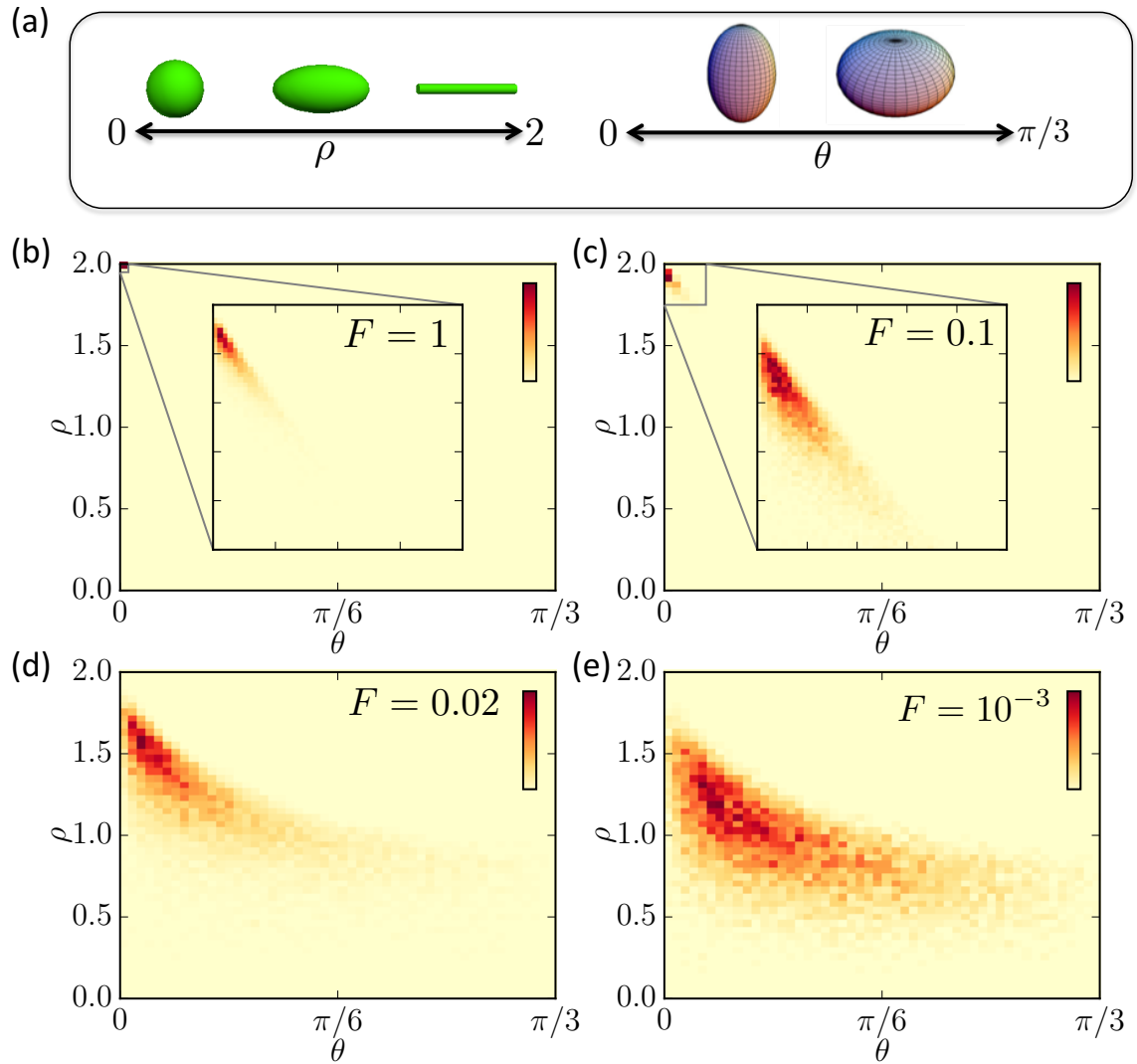


Figure 3.17: The shape of pinned polymer loop distributed over the phase diagram of asphericity and the nature of asphericity. (a) The meaning of asphericity and the nature of asphericity are illustrated. (b) The $\rho - \theta$ phase diagram for $F = 1$. (c) The $\rho - \theta$ phase diagram for $F = 0.1$. (d) The $\rho - \theta$ phase diagram for $F = 0.02$. (e) The $\rho - \theta$ phase diagram for $F = 0.001$. Other parameters are $k_B T = 1$, $L = 1$, $a = 1$.

able to calculate the mean and variance of bead position.

We then extended our theory to the three-dimensional system. The same method of Brownian bridge was used to solve the equilibrium statistics of the polymer configuration. Also, the three-dimensional mean and variance of the bead position were calculated. Moreover, the pairing process of two identical polymer loops pinned at the same point was discussed. We calculated the statistical distance of the corresponding beads along the polymer loops. We found that the external force field can reduce the statistical distance significantly. Thus the mechanism of facilitating pairing by pulling was illustrated. In addition, we also considered the intersecting polymer loops in order to study the role of additional constraints in the pairing process. The results show that the additional constraints further reduce the fluctuation and facilitate the pairing process.

In the last section, we employed our theoretical results to discuss the shape of pinned polymer loops in an external force field. The marginal distribution of segment density was calculated in both parallel and transverse direction of the force field. We then quantified the shape based on the three-dimensional gyration tensor. Interestingly, we found that the width of gyration radius distribution varies non-monotonically with the strength of the external force field. The diagram of asphericity and the nature of asphericity were shown which imply a rod-like and prolate shape of the pinned polymer loops in both weak and strong force field. The shape measurements discussed here could be compared with the experimental data in the future.

In next chapter, we delve deeper to study the dynamical properties of the pinned polymer loop in an external force field.

Chapter 4

Relaxation Dynamics of the Forced Pinned Polymer Loop

In the previous chapter, the equilibrium statistics of pinned polymer loops in an external force field were discussed in detail. However, we have assumed that the relaxation time of the system is much smaller than the oscillation period to make our discussion relevant for the biological circumstances. This assumption needs to be justified. The dynamical properties of pinned polymers in an external field is an interesting topic from the theoretical point of view. To the best of our knowledge, the way to calculate the relaxation time of a pinned bead-rod model in an external force field is still missing.

In this chapter, we study the dynamical properties of the pinned polymer loop model. In the first section, we illustrate how to apply the Rouse theory on the pinned polymer loop model in an external field. In the second section, we introduce the mapping from 1D polymer dynamics to the ASEP and show some interesting results from the Kinetic Monte Carlo simulations. In the third section, we use the Bethe ansatz method to solve the ASEP problem exactly and calculate the relaxation time analytically. In the fourth section, we try to apply our calculation to the 3D bead-rod model. Finally, a summary is given in the last section.

4.1 Rouse theory of the pinned bead-spring loop

Rouse theory is a theoretical framework to calculate the dynamics of a bead-spring polymer [19]. In the case of modeling chromosomes in fission yeast, we mainly use the bead-rod model instead of the bead-spring model. However, the study of Rouse theory is still useful because of several reasons. On one hand, we can see later that the Rouse theory can correctly represent the dynamics of the bead-rod model when the external force field is vanished. On the other hand, the Rouse theory describing the infinite extensible bead-spring polymer allows us to study the role of extensibility when compared with the result of finite extensible bead-rod model.

Despite of the simplicity of the Rouse theory, we have not seen a calculation of the Rouse theory on the pinned polymer loop model. To the best of our knowledge, what

we present here is new. Let us start by writing down the dynamical equations of the model.

4.1.1 Dynamical equation

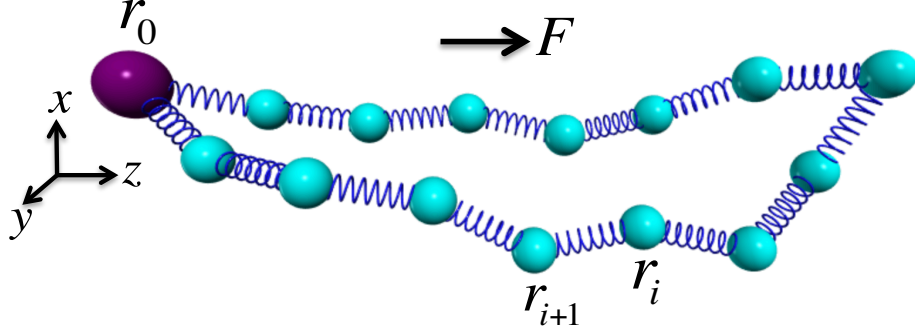


Figure 4.1: The sketch of pinned bead-spring loop with notations.

We consider a pinned polymer loop modeled by beads and connecting springs (Fig. 4.1). As in our previous discussion of the bead-rod model, the bead labeled by 0 is assumed to be pinned at the origin and there are L beads in total in the loop. Again, the periodic indexing is used. We can write the pinned condition as $\mathbf{r}_0 = \mathbf{r}_L = \mathbf{0}$.

The dynamical equation for a single bead in the loop is Eq. (2.10). Here, we rewrite it for the convenience of later calculation as:

$$\xi \frac{d\mathbf{r}_i}{dt} = -k_H \sum_k A_{ik} \mathbf{r}_k + \mathbf{f}_i^e + \mathbf{f}_i^b, \quad (4.1)$$

where ξ is the friction coefficient of bead in fluid, \mathbf{r}_i is the bead position of the i^{th} bead, k_H is the spring constant with a linear Hookean spring assumed. \mathbf{f}_i^e is the external force exerted on beads, \mathbf{f}_i^b is a typical Brownian force satisfying Eq. (2.2). For a pinned loop, \mathbf{A} is a $(L-1) \times (L-1)$ matrix and has the following form

$$\mathbf{A} = \begin{bmatrix} 2 & -1 & 0 & \cdots \\ -1 & 2 & -1 & \cdots \\ \vdots & \ddots & \ddots & \vdots \\ \cdots & -1 & 2 & -1 \\ \cdots & 0 & -1 & 2 \end{bmatrix}. \quad (4.2)$$

We do not take into account any complex terms of interaction such as bending energy and excluded volume effect in this simple model.

4.1.2 The normal modes

For convenience, we use the vector notation and rewrite Eq. (4.1) as:

$$\xi \frac{d}{dt} \mathbf{R} = -k_H \mathbf{A} \mathbf{R} + \mathbf{F}^e + \mathbf{F}^b, \quad (4.3)$$

where $\mathbf{R} = [\mathbf{r}_1, \mathbf{r}_2, \dots, \mathbf{r}_{L-1}]^T$. Similar vector notation is also applied for $\mathbf{F}^e, \mathbf{F}^b$. In order to solve this set of dynamical equations, we first notice that the connecting matrix \mathbf{A} is a very special type of matrix called tridiagonal Toeplitz matrix [166]. Fortunately, it can be diagonalized exactly. To do this, let us introduce a similarity transform such that

$$[\Omega^{-1} \mathbf{A} \Omega]_{jk} = \mathbf{D}_{jk} = \lambda_k \delta_{jk}, \quad (4.4)$$

here Ω is normalized to be a unitary matrix, and λ_k is the eigenvalue of matrix \mathbf{A} . The calculation details are shown in Appendix C. The results can be written as following

$$\lambda_k = 4 \sin^2 \left(\frac{k\pi}{2L} \right), k = 1, 2, \dots, L-1; \quad (4.5a)$$

$$\Omega_{jk} = \Omega_{kj} = [\Omega^{-1}]_{jk} = [\Omega^{-1}]_{kj} = \sqrt{\frac{2}{L}} \sin \left(\frac{jk\pi}{L} \right). \quad (4.5b)$$

Multiplying both sides of Eq. (4.3) by Ω^{-1} , we arrive at

$$\xi \frac{d(\Omega^{-1} \mathbf{R})}{dt} = -k_H \Omega^{-1} \mathbf{A} \Omega \Omega^{-1} \mathbf{R} + \Omega^{-1} \mathbf{F}^e + \Omega^{-1} \mathbf{F}^b. \quad (4.6)$$

Here $\Omega^{-1} \mathbf{A} \Omega = \mathbf{D}$. Using the notation such that $\tilde{\mathbf{R}} = \Omega^{-1} \mathbf{R}$, we get the set of decoupled dynamical equations

$$\xi \frac{d\tilde{\mathbf{r}}_j}{dt} = -k_H \lambda_j \tilde{\mathbf{r}}_j + \tilde{\mathbf{f}}_j^e + \tilde{\mathbf{f}}_j^b. \quad (4.7)$$

Eq. (4.7) can be solved easily by standard methods. The general solution can be written as:

$$\tilde{\mathbf{r}}_j(t) = \tilde{\mathbf{r}}_j(0) e^{-\frac{k_H \lambda_j}{\xi} t} + \frac{1}{\xi} \left(\int_0^t \tilde{\mathbf{f}}_j^e e^{-\frac{k_H \lambda_j}{\xi} (t-t')} dt' + \int_0^t \tilde{\mathbf{f}}_j^b e^{-\frac{k_H \lambda_j}{\xi} (t-t')} dt' \right). \quad (4.8)$$

Here the transformed Brownian force also fulfills

$$\langle \tilde{\mathbf{f}}_j^b \rangle = \mathbf{0}; \quad (4.9a)$$

$$\langle \tilde{f}_{i\alpha}^b(t) \tilde{f}_{j\beta}^b(t') \rangle = 2\xi k_B T \delta_{ij} \delta_{\alpha\beta} \delta(t-t'). \quad (4.9b)$$

Given the solution of Eq. (4.8), the position of each bead can be obtained by the inverse transformation $\mathbf{R} = \Omega \tilde{\mathbf{R}}$. In the simple case of constant external force field, $\mathbf{f}_j^e = f^e \mathbf{e}_z$, Eq. (4.8) can be rewritten as

$$\tilde{\mathbf{r}}_j(t) = \tilde{\mathbf{r}}_j(0)e^{-\frac{k_H \lambda_j}{\xi} t} + \frac{\tilde{f}^e \mathbf{e}_z}{k_H \lambda_j} \left(1 - e^{-\frac{k_H \lambda_j}{\xi} t}\right) + \frac{1}{\xi} \int_0^t \tilde{\mathbf{f}}_j^b e^{-\frac{k_H \lambda_j}{\xi} (t-t')} dt'. \quad (4.10)$$

Finally, the bead position can be obtained by the inverse transformation:

$$\mathbf{r}_i(t) = \sum_j \Omega_{ij} \tilde{\mathbf{r}}_j(t) \quad (4.11)$$

Now the equilibrium statistics of the polymer, such as the mean and variance of each bead position can be calculated easily. Substituting $\tilde{\mathbf{r}}_j(t)$ from Eq. (4.10) to Eq. (4.11) and taking the limit $t \rightarrow \infty$, we get

$$\langle \mathbf{r}_i^\infty \rangle = \sum_j \Omega_{ij} \frac{\tilde{f}^e \mathbf{e}_z}{k_H \lambda_j} = \frac{f^e \mathbf{e}_z}{2Lk_H} \sum_{j,k} \frac{\sin\left(\frac{ij\pi}{L}\right) \sin\left(\frac{jk\pi}{L}\right)}{\sin^2\left(\frac{j\pi}{2L}\right)}. \quad (4.12)$$

The summation of j can be calculated explicitly, we get

$$\langle \mathbf{r}_i^\infty \rangle = \frac{f^e \mathbf{e}_z}{k_H} \sum_{k=1}^{\frac{L+1}{2}} \frac{\sin\left(\frac{i(2k-1)\pi}{L}\right)}{(2k-1)\pi \sin^2\left(\frac{(2k-1)\pi}{2L}\right)}. \quad (4.13)$$

One can clearly see from Eq. (4.13) that $\langle \mathbf{r}_i^\infty \rangle = \langle \mathbf{r}_{L-i}^\infty \rangle$ as expected. In addition, the components of mean position perpendicular to the force field direction are vanished.

In order to calculate the variance of the bead position, it is nontrivial to firstly calculate the two-time correlation of normal coordinate position as

$$\begin{aligned} \langle \tilde{\mathbf{r}}_m(t) \tilde{\mathbf{r}}_n(t') \rangle &= \langle \tilde{\mathbf{r}}_m(0) \tilde{\mathbf{r}}_n(0) \rangle e^{-\frac{k_H \lambda_m}{\xi} t - \frac{k_H \lambda_n}{\xi} t'} \\ &+ \frac{(\tilde{f}^e)^2}{k_H^2 \lambda_m \lambda_n} \left(1 - e^{-\frac{k_H \lambda_m}{\xi} t}\right) \left(1 - e^{-\frac{k_H \lambda_n}{\xi} t'}\right) \\ &+ \frac{3k_B T}{k_H \lambda_m} e^{-\frac{k_H \lambda_m}{\xi} t} \delta_{mn}. \end{aligned} \quad (4.14)$$

Then the second moment of the bead position can be calculated as:

$$\langle \mathbf{r}_i^2(t) \rangle = \sum_{m,n} \Omega_{im} \Omega_{in} \langle \tilde{\mathbf{r}}_m(t) \tilde{\mathbf{r}}_n(t) \rangle. \quad (4.15)$$

Finally, taking the limit $t \rightarrow \infty$, we get the equilibrium variance of the bead position

$$\text{var} [\mathbf{r}_i^\infty] = \langle (\mathbf{r}_i^\infty)^2 \rangle - \langle \mathbf{r}_i^\infty \rangle^2 = \frac{3k_B T}{2Lk_H} \sum_{k=1}^{L-1} \left[\frac{\sin\left(\frac{ik\pi}{L}\right)}{\sin\left(\frac{k\pi}{2L}\right)} \right]^2 \simeq \frac{3k_B T}{k_H L} i(L-i). \quad (4.16)$$

It is worth mentioning here we also have the symmetry that $\text{var} [\mathbf{r}_i^\infty] = \text{var} [\mathbf{r}_{L-i}^\infty]$. Moreover, we want to point out that the variance does not depend on the external force. It means that the statistical distance between two beads does not depend on the external force field. This is essentially because infinite extensible Hookean springs are employed in the Rouse theory. Furthermore, we also want to remark that the result of Eq. (4.16) is identical to the Brownian bridge result without external force.

4.1.3 Relaxation time

We discuss in this subsection the relaxation time of the pinned polymer loop. To extract the relaxation time, we calculate the autocorrelation function of diameter vector, defined as $\mathbf{r}_d = \mathbf{r}_{\frac{L}{2}} - \mathbf{r}_0 = \mathbf{r}_{\frac{L}{2}}$, to obtain

$$\langle \mathbf{r}_d(t) \mathbf{r}_d(0) \rangle = \sum_{m,n} \Omega_{\frac{L}{2}m} \Omega_{\frac{L}{2}n} \langle \tilde{\mathbf{r}}_m(t) \tilde{\mathbf{r}}_n(0) \rangle. \quad (4.17)$$

From Eq. (4.14) we can readily get the relaxation time

$$\tau = \frac{\xi}{k_H \lambda_1} = \frac{\xi}{4k_H \sin(\pi/2L)}, \quad (4.18)$$

when L is large we can expand the sin term arriving at $\tau = \frac{\xi L^2}{k_H \pi^2}$, which coincides with the unpinned polymer chain [18, 19], called Rouse time. Like the variance of bead position, the relaxation time does not depend on the external force.

4.1.4 Comparison to the bead-rod model

Now we try to fit the Rouse theory to the pinned bead-rod loop. To do this, we take the spring in the bead-spring model as entropic spring and then relate the spring constant to the length of the rod. If the spring in the polymer is the three-dimensional entropic spring, then the spring constant can be evaluated by the equipartition theorem as

$$\frac{1}{2} k_H a^2 = \frac{3}{2} k_B T, \quad (4.19)$$

where a can be interpreted as the equilibrium length of the spring and is set to the length of a rod for the comparison. We obtain $k_H = \frac{3k_B T}{a^2}$. Plugging it into Eq. (4.13)

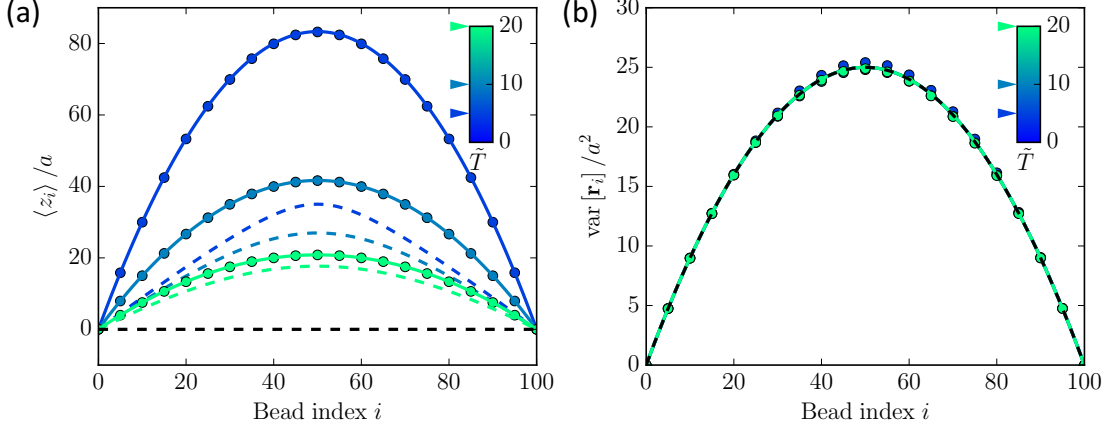


Figure 4.2: The equilibrium mean and variance of bead position for the bead-spring model, compared with the bead-rod model. (a) Mean bead position of the z component. (b) The variance of bead position. Dots are BD simulation results of the bead-spring model, solid lines are the Rouse theory. Dashed lines are the theory of the bead-rod model. Different color denotes different dimensionless temperature \tilde{T} which is indicated in the legend. The black dash line in both (a) and (b) shows the limit of no external force field.

and Eq. (4.16) we arrive at

$$\langle \mathbf{r}_i^\infty \rangle = \frac{1}{3\tilde{T}} a \mathbf{e}_z \sum_{k=1}^{\frac{L+1}{2}} \frac{\sin\left(\frac{i(2k-1)\pi}{L}\right)}{(2k-1)\pi \sin^2\left(\frac{(2k-1)\pi}{2L}\right)}; \quad (4.20a)$$

$$\text{var}[\mathbf{r}_i^\infty] = a^2 \frac{i(L-i)}{L}; \quad (4.20b)$$

where $\tilde{T} = k_B T / \Delta E = k_B T / f^e a$. Now we can compare these results with the bead-rod results obtained in previous chapter. From Fig. 4.2, we notice that unlike the bead-rod model, the variance of bead position does not depend on the external force field here. This is a fundamental difference between the bead-rod and bead-spring model.

For the relaxation time, plugging Eq. (4.19) into the Eq. (4.18) and let $L \gg 1$, we obtain

$$\tau = \frac{\xi a^2 L^2}{3\pi^2 k_B T}. \quad (4.21)$$

Interestingly, it coincides with the relaxation time of a free bead-spring polymer chain with L monomers. Again, it does not depend on the external force field. We remark here that $k_H = k_B T / a^2$ in case of 1D, which results in a factor of 3 for the relaxation time. More discussions can be found in the Section 4.4.

In this section, we discussed the Rouse theory for pinned polymer loop in an external force field. Using the theory, the equilibrium statistics of the bead position and the relaxation time of the pinned polymer loop were calculated. The equilibrium results were compared to the results from the bead-rod model. We found that the relaxation time of the bead-spring model does not depend on the external force field. Physically, it is caused by the infinite extensibility of the springs. To further explore the role of finite extensibility, in following sections, we try to solve the relaxation time of the rigid bead-rod model.

4.2 1D pinned bead-rod loop can be mapped to ASEP

We have illustrated the mapping from one-dimensional polymer loop to particles on lattice sites in Chapter 3. Here, we further show that the same mapping can also be used to study the polymer dynamics. The dynamics of the bead-rod polymer can be mapped to the hopping process of the exclusive particles, which is well known as ASEP.

4.2.1 The mapping to ASEP

We recall that in the mapping from 1D bead-rod polymer to the particle-lattice system, right oriented rods are interpreted as sites occupied by one particle, left oriented rods are interpreted as empty sites. L rods map to exactly L lattice sites and the reflecting boundaries are applied. The number of particles must be exactly $L/2$ because of the looping condition.

Now, let us consider the dynamical problem in the picture of particle-lattice. It is intuitive to imagine that the particle can hop to the empty neighboring sites. Multiple occupations are forbidden because the phase space is restricted to be binary. This kind of one-dimensional particle hopping process is exact ASEP. The hopping rates to left and right are usually not the same. The reflecting boundaries can be imposed representing ASEP with reflecting boundary conditions. In Fig. 4.3 (a), we present a schematic diagram of the reflecting ASEP. The question is what is the corresponding process of particle hopping in the polymer picture.

Let us consider just one particle with its neighboring sites and take the example of the particle hopping to the left site. The particle that hops to the left affects the states of two neighboring sites and thus the states of two neighboring rods in the polymer picture. Correspondingly, the orientation of the two rods change from left-right to right-left. So one step of particle hopping corresponds to a flip of two rods connecting to the same bead in the polymer picture. The same analysis can be applied to the case when the particle hops to the right. Fig. 4.3 (b) illustrates the mapping of the hopping process. Then the next question is how to determine the hopping rates corresponding to the flipping of rods.

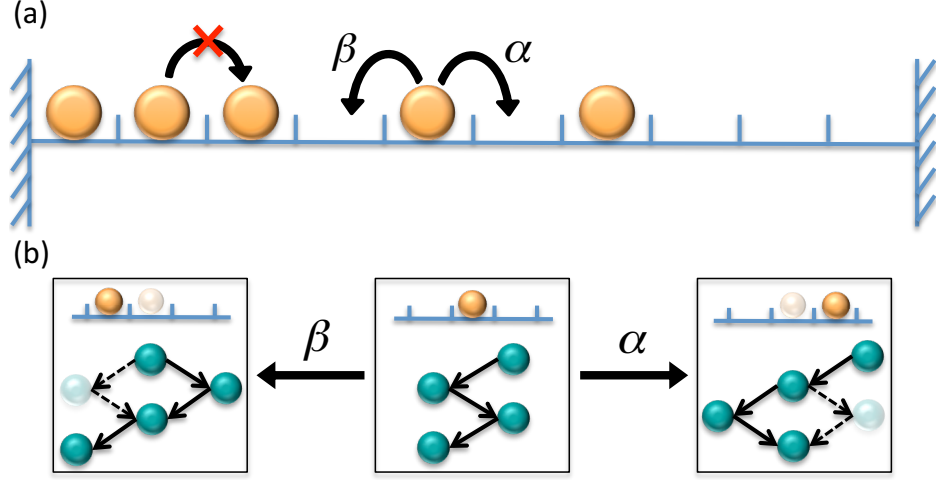


Figure 4.3: The schematic of ASEP and the mapping of dynamics. (a) Illustration of ASEP, orange beads represent particle and reflecting boundary is indicated. (b) Illustration of one step particle hopping process maps to the flipping of two neighboring rods in the polymer picture.

We denote the rate of particle hopping to the right and to the left as α and β respectively. We start with the case of no external force field, i.e. $F = 0$. In this case, there is no hopping bias, so we have $\alpha = \beta$. The value of the hopping rates is related to the flipping time scale of two rods in the polymer picture. Here we estimate the flipping time by a typical timescale τ_0 for a bead to diffuse a distance of the order of the rod length a . Then the total hopping rate $r := \alpha + \beta$ can be estimated as

$$r = 1/\tau_0 = \frac{2D}{a^2} = \frac{2k_B T}{\xi a^2}. \quad (4.22)$$

where we used the diffusion constant of the bead given by Einstein relation $D = k_B T/\xi$, and ξ being the friction coefficient. As a result, we have $\alpha = \beta = r/2$ in the case of $F = 0$.

Now we turn to the case when $F \neq 0$. In this case, the hopping of particles is biased by the external force field. Here, we assume the “local” detailed balance condition [147, 165] to be fulfilled:

$$\alpha/\beta = \exp(-\Delta E/k_B T), \quad (4.23)$$

where ΔE is the energy change between the pre-hopping configuration η and post-hopping configuration η' . η and η' are different by a single hopping step of one particle to the left. We emphasise that Eq. (4.23) in general does not mean the system is in equilibrium, for which the global detailed balance condition $\alpha/\beta = P^{eq}(\eta)/P^{eq}(\eta')$ has

to be fulfilled. Here $P^{eq}(\eta)$ is the equilibrium probability of the configurations. ASEP with *periodic* boundary condition is an example where the “local” detailed balance holds while the global detailed balance is violated because $P^{eq}(\eta)$ is uniform. However, the global detailed balance is satisfied for the case of reflecting ASEP discussed here [137, 147].

In order to fully determine the hopping rates α and β , one more constraint is required in the case of $F \neq 0$. Here, we adopt the same argument used in Driven Lattice Gas systems [147]. Namely, by introducing an external force field, the hopping rate along the force field β is enhanced by a factor κ so that $\beta = \kappa r/2$, and the hopping rate against the force field α is reduced by the same factor so that $\alpha = \kappa^{-1}r/2$. Then, from Eq. (4.23), we can easily obtain $\kappa = \exp(\Delta E/2k_B T)$, and the corresponding left and right hopping rates for the ASEP system become

$$\alpha = \frac{k_B T}{\xi a^2} \exp(-\Delta E/2k_B T) \quad (4.24a)$$

$$\beta = \frac{k_B T}{\xi a^2} \exp(\Delta E/2k_B T) \quad (4.24b)$$

With Eq. (4.24), we now have a well defined reflecting ASEP model that can be mapped to the polymer dynamics. Here are several remarks about the mapping:

- For simplicity, we have assumed that only single-particle hopping is allowed in the ASEP system. In the polymer picture, this corresponds to demanding that only the smallest segment of the loop – a single bead – is allowed to move at any given time, and there are no simultaneous movements in longer segments.

- We have assumed here that α , β are the same for different lattice sites, i.e. a homogeneous hopping system is assumed.

- In the polymer picture, ΔE is the energy change caused by the flipping of two neighboring rods. In the strictly one-dimensional setting, we cannot define the continuous process of flipping but only its initial and final states. We have $\Delta E = 2Fa$ in 1D. However, when we try to fit the mapping to a 3D system, where the continuous rotation of rods is possible, $\Delta E = Fa$ should be used. The intuition is that rotation over $\pi/2$ already changes the orientation of two neighboring rods. The setting of $\Delta E = Fa$ is also consistent with the calculation of equilibrium statistics of 3D pinned polymer loops in Section 3.3.

Although ASEP is a well studied non-equilibrium model, not so many works focus on the particular case of reflecting boundary conditions. To the best of our knowledge, the exact solution of the full dynamics of the reflecting ASEP system is still missing. In the next section, we solve the problem completely using a generalized Bethe ansatz method. However, we would like to discuss some interesting numerical results before that in order to highlight certain features of the reflecting ASEP system.

4.2.2 Some numerical results

We solved the equilibrium statistics of the 1D particle-lattice model in the Chapter 3. To solve the dynamics, we first resort to numerical simulations to get some hints. Since the 1D reflecting ASEP is a well-defined model, we can forget about the mapping to polymer system and focus on the ASEP model itself in this moment. We illustrate some of the numerical details in this subsection.

We are mainly interested in the relaxation time of the system. Relaxation time characterizes how long the system takes to return to the stationary state when it is subjected to a small perturbation. In the reflecting ASEP system, we trace the trajectory of a tagged particle, then calculate the auto-correlation function of the trajectory to extract the relaxation time. Usually, we choose a particle in the middle. If we denote the position of this particle as $x_{\frac{N}{2}}$, and the total number of particles in the system as N , the autocorrelation function can be written as

$$\left\langle x_{\frac{N}{2}}(t)x_{\frac{N}{2}}(0) \right\rangle \sim \sum_k \exp\left(-\frac{t}{\tau_k}\right). \quad (4.25)$$

In the long time regime, the largest τ_k , which we denote by τ for simplicity, dominates the relaxation. By fitting the autocorrelation function in the long time regime, we can obtain the relaxation time numerically.

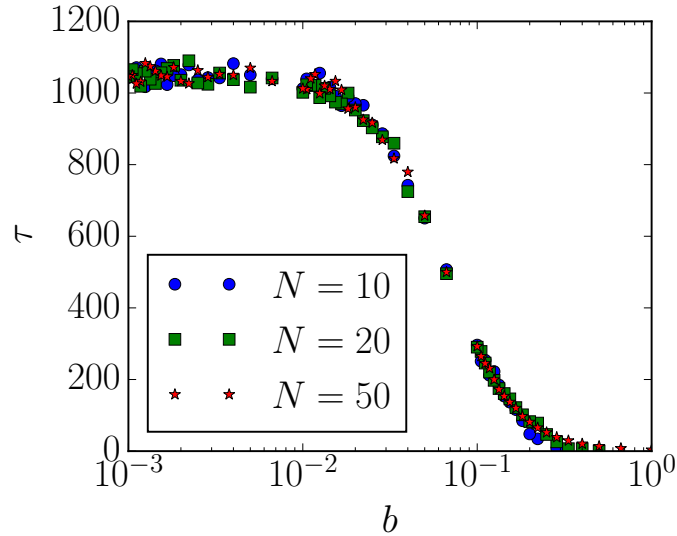


Figure 4.4: The relaxation time of 1D reflecting ASEP system varies with hopping bias. Total number of lattice site is $L = 100$, and $k_B T / \xi a^2 = 1$. Different markers denote different total number of particles on the lattice.

In our simulations of 1D reflecting ASEP, we use the Kinetic Monte Carlo algorithm to simulate the particle hopping process. Details of this algorithm are shown in

Appendix B. Then the autocorrelation function Eq. (4.25) is measured and fitted to extract the longest relaxation time. In Fig. 4.4, we show that the relaxation time of a 1D reflecting ASEP model varies with a dimensionless parameter b , which is defined as

$$b := \ln\left(\frac{\beta}{\alpha}\right) \in [0, \infty). \quad (4.26)$$

When there is no hopping bias, i.e., $\alpha = \beta$, we have $b = 0$, and b increases as the bias becomes stronger. Fig. 4.4 illustrates the simulation results of a system with total lattice sites $L = 100$ but different particle number N on the lattice. We can read from Fig. 4.4 that the three curves of $\tau(b)$ are almost overlapped. The crucial point hinted by the simulation results is that the relaxation time of the system seems to be independent of the total particle number on the lattice (as long as it is neither all empty nor all occupied). Intuitively, one can imagine the relaxation time of a system with N particles and $L - N$ particles should be the same because of the particle-hole symmetry. However, our simulation results suggest that it is far more than one expected.

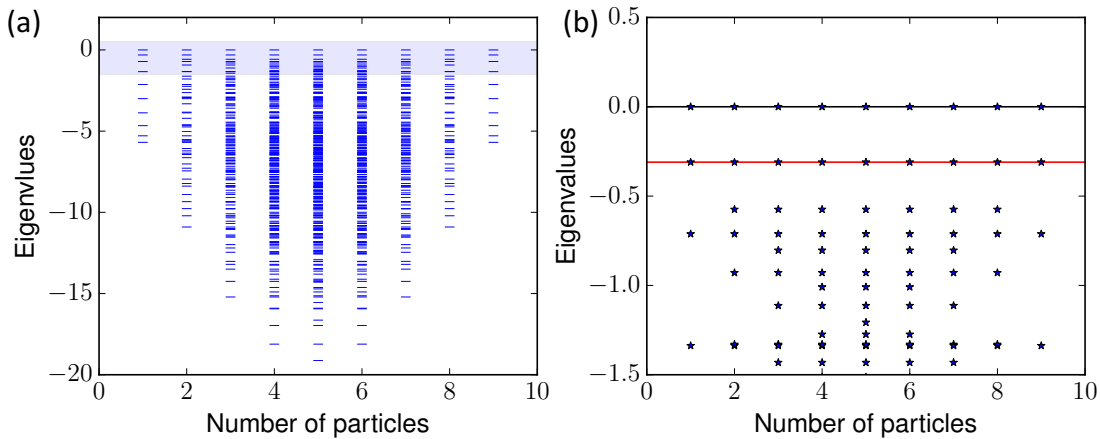


Figure 4.5: Eigenvalues of a small 1D reflecting ASEP system with different particle number on the lattice. $L = 10$ and the number of particle $N \in \{1, 2, \dots, 9\}$. (a) All eigenvalues, the eigenvalue is marked by bars. (b) Zoom in view for the shaded regime in (a), eigenvalues are marked by asters, the back line denotes the zero line and the red line shows that the second largest eigenvalues are all the same. Parameters are set as $\alpha = 1$, $\beta = 2$.

To understand this observation, we write down the master equation which describes the dynamics of the ASEP system:

$$\frac{dP(\eta, t)}{dt} = M \cdot P(\eta, t), \quad (4.27)$$

where M is a $\binom{L}{N} \times \binom{L}{N}$ matrix, called Markov matrix. Numerically, the matrix M can be constructed by enumerating all possible many-particle configurations $\{\eta\}$ of the ASEP. The transition rate $M_{\eta,\eta'}$ is set to α if a configuration η can be reached from an other configuration $\eta' \neq \eta$ by an event of a single particle hopping to the right. Similarly, $M_{\eta',\eta} = \beta$. The diagonal elements are prescribed by conservation of probabilities, $M_{\eta,\eta} = -\sum_{\eta'} M_{\eta',\eta}$.

The dynamical information of the system is encoded in the Markov matrix M . By diagonalizing the matrix, we can obtain the full dynamical information in terms of eigenvalues and eigenvectors. For example, the stationary state corresponds to the eigenvector with zero eigenvalue, and the longest relaxation time of the system is related to the second largest eigenvalue Λ_1 . For a stochastic system with stationary state, the eigenvalues of the Markov matrix are always non-positive. The longest relaxation time can thus be calculated as

$$\tau = -\frac{1}{\Lambda_1}. \quad (4.28)$$

In Fig. 4.5, we use the brute force algorithm to diagonalize a small size system with $L = 10$ lattice sites and different particle number. In these results, we observe the following:

- All eigenvalues are non-positive as expected.
- The eigenvalues satisfy the particle-hole symmetry, i.e. the eigenvalues for N particle system and $L - N$ particle system are exactly the same. This is well illustrated in Fig. 4.5 (a).
- By carefully examining Fig. 4.5 (a), we can find that the set of eigenvalues in case of $N = 1$ is a subset of the case $N = 2$. In general, the set of eigenvalues for the case N is contained in the set of eigenvalues for the case $N + 1$ as long as $N < L/2$. This is another interesting key feature of the reflecting ASEP system.
- As indicated by the red line in Fig. 4.5 (b), we can see that the second largest eigenvalue for all the cases is the same. The result explains our observation shown in Fig. 4.4. For more general cases, detailed discussions are presented in next section.

In this section, we introduced the mapping from polymer dynamics to the ASEP model with reflecting boundaries. Moreover, we discussed some interesting simulation results of the reflecting ASEP model. Some interesting features of the reflecting ASEP system was illustrated. In next section, we use the generalized Bethe ansatz method to solve the reflecting ASEP model exactly. With the exact solution, we map it back to understand the polymer dynamics.

4.3 The Bethe ansatz solution of ASEP

As introduced in Section 1.3, the Bethe ansatz method is a powerful tool used for seeking the complete solution of the ASEP system. For instance, the standard Bethe

ansatz solution which is composed by plane wave functions works perfectly on the ASEP system with periodic boundaries. However, the standard Bethe ansatz does not work in the case of reflecting boundaries.

In this section, we show that a generalized Bethe ansatz method can be used to solve the dynamics of the ASEP model with reflecting boundaries. Unlike the standard Bethe ansatz, the generalized Bethe ansatz is constructed by more complex building functions. We find that the single particle eigenfunctions, which take into account the boundary conditions, can be used as the building functions. In order to construct the solution, let us first discuss the single particle solution of the reflecting ASEP system.

4.3.1 Solution of single particle

The master equation of a single particle on a closed lattice with L sites can be written as:

$$\frac{d}{dt}P(x, t) = \alpha P(x - 1, t) + \beta P(x + 1, t) - (\alpha + \beta)P(x, t), \quad (4.29a)$$

$$\frac{d}{dt}P(1, t) = \beta P(2, t) - \alpha P(1, t), \quad (4.29b)$$

$$\frac{d}{dt}P(L, t) = \alpha P(L - 1, t) - \beta P(L, t), \quad (4.29c)$$

where $P(x, t)$ is the probability of a particle sitting on site x at time t , and x is confined to be an integer in the range of $x \in \{1, 2, \dots, L\}$. Eq. (4.29b) and (4.29c) are the special cases of the master equation at the boundaries. It is more convenient to rewrite Eq. (4.29b) and (4.29c) as the following boundary conditions:

$$\alpha P(0, t) = \beta P(1, t), \quad (4.30a)$$

$$\alpha P(L, t) = \beta P(L + 1, t). \quad (4.30b)$$

The notation of Eq.(4.30) might be confusing. Because $x = 0, L + 1$ sites are out of the domain and one would expect the corresponding $P(x, t) = 0$. However, this notation actually employs a technique called “ghost coordinate”, which is often used in the analysis of discrete stochastic processes [147]. To clarify the concept, we remark several points here:

- By writing down Eq. (4.30), we have introduced an auxiliary space with infinite lattice sites where the master equation Eq. (4.29a) is satisfied. In the auxiliary space, $P(0, t)$ and $P(L + 1, t)$ are not necessarily vanished.

- Based on the auxiliary space, we then impose additional constraints. Eq. (4.30a) can be interpreted as the flux from site 0 to site 1 equals to the flux from site 1 to site 0. Similarly, the same interpretation can also be applied to Eq. (4.30b). So the boundary condition simply means that the net flux at the boundaries is vanished. Namely, the reflecting boundary condition is imposed.

• Physically, $P(x, t)$ in the real space is normalized in the domain $x \in \{1, 2, \dots, L\}$, and the probability outside the domain is zero.

• Mathematically, Eq. (4.30) can be derived straightforwardly by assuming Eq. (4.29a) is valid in the whole space and subtracting Eq. (4.29a) by Eq. (4.29b) and Eq. (4.29c), respectively.

Now, our task is to solve the master equation Eq. (4.29a) and boundary conditions Eq. (4.30). Let us take the ansatz of separation of variables $P(x, t) = \phi(x)e^{\lambda t}$ and plug it into Eq. (4.29a), obtaining

$$\beta\phi(x+1) - (\alpha + \beta + \lambda)\phi(x) + \alpha\phi(x-1) = 0. \quad (4.31)$$

Given that x is an integer number, Eq. (4.31) is essentially a set of linear difference equations. Substituting the ansatz of $P(x, t)$ into Eq. (4.30), we obtain

$$\alpha\phi(0) = \beta\phi(1), \quad (4.32a)$$

$$\alpha\phi(L) = \beta\phi(L+1). \quad (4.32b)$$

The standard method to find the solution of $\phi(x)$ is to take an ansatz $\phi(x) = Az^x$, where z is an arbitrary complex number. We arrive at the quadratic characteristic equation:

$$\beta z^2 - (\alpha + \beta + \lambda)z + \alpha = 0. \quad (4.33)$$

If we denote the two roots of Eq. (4.33) as z_+ and z_- respectively, we have $z_+z_- = \frac{\alpha}{\beta}$. The solution of Eq. (4.31) can be written as

$$\phi(x) = A_+z_+^x + A_-z_-^x. \quad (4.34)$$

By applying Eq. (4.32) to Eq. (4.34), we can find all the eigenvalues and corresponding eigenvectors. The results are summarized as following. The stationary eigenmode with zero eigenvalue is

$$\phi_s(x) = A \left(\frac{\alpha}{\beta} \right)^x, \quad A = \text{const.} \quad (4.35a)$$

$$\lambda_s = 0. \quad (4.35b)$$

There are $L - 1$ non-stationary eigenmodes and corresponding eigenvalues, which can be written as

$$\phi_k(x) = A_k \left(\frac{\alpha}{\beta} \right)^{\frac{x}{2}} \left[\sin \left(\frac{k\pi}{L} x \right) - \sqrt{\frac{\beta}{\alpha}} \sin \left(\frac{k\pi}{L} (x-1) \right) \right], \quad (4.36a)$$

$$\lambda_k = -(\alpha + \beta) + 2\sqrt{\alpha\beta} \cos\left(\frac{k\pi}{L}\right); \quad k = 1, 2, \dots, L-1. \quad (4.36b)$$

The eigenvalue $\lambda_s = 0$ and the corresponding eigenvector represent the stationary mode $\phi_s(x)$. We define a scalar product between any two functions by

$$(\phi, \psi) = \sum_x \frac{\phi(x)\psi(x)}{\phi_s(x)}. \quad (4.37)$$

The definition Eq. (4.37) makes $\phi_s(x)$ identical to the stationary distribution $P^e(x)$, where x is an integer. By properly choosing the constant pre-factor and let $L \rightarrow \infty$, one can check the orthogonality and completeness of the eigenfunctions:

$$\sum_{x=1}^L \phi_k(x)\phi_l(x) = \delta_{k,l}, \quad (4.38a)$$

$$\sum_{k=1}^L \phi_k(x)\phi_k(y) = \delta_{x,y}. \quad (4.38b)$$

For an arbitrary initial distribution of $P(x, 0)$, we can decompose it as

$$P(x, 0) = \sum_k c_k \phi_k(x), \quad (4.39)$$

where c_k can be calculated by

$$c_k = \sum_x \phi_k(x)P(x, 0). \quad (4.40)$$

Finally, the solution of single particle on reflecting lattice can be written as

$$P(x, t) = \sum_k \phi_k(x) e^{\lambda_k t} \sum_{x'} \phi_k(x') P(x', 0). \quad (4.41)$$

For the special case that $P(x, 0) = \delta_{x,y}$, solution (4.41) can be simplified to

$$P(x, t) = \sum_k \phi_k(x)\phi_k(y) e^{\lambda_k t}. \quad (4.42)$$

With the complete solution of reflecting ASEP with single particle, we can step further to the system of more particles. The idea is that the single particle solution can work as the building blocks of the N -particle solution. To illustrate that, we start with the case of $N = 2$ in next subsection.

4.3.2 Solution of two particles

We denote the probability of the two particles sitting at x_1 and x_2 respectively at time t as $P(x_1, x_2; t)$, assuming $x_1 < x_2$. Firstly, we shall write down the master equation, which is

$$\begin{aligned} \frac{dP(x_1, x_2; t)}{dt} = & \alpha P(x_1 - 1, x_2; t) + \beta P(x_1 + 1, x_2; t) \\ & + \alpha P(x_1, x_2 - 1; t) + \beta P(x_1, x_2 + 1; t) \\ & - 2(\alpha + \beta)P(x_1, x_2; t). \end{aligned} \quad (4.43)$$

Taking the same eigenfunction expansion as in the single particle case, we get

$$P(x_1, x_2, t) = \sum_k \Psi_k(x_1, x_2) e^{\Lambda_k t}. \quad (4.44)$$

Plugging it into the master equation Eq. (4.43) we have

$$\begin{aligned} \Lambda \Psi(x_1, x_2) = & \alpha \Psi(x_1 - 1, x_2) + \beta \Psi(x_1 + 1, x_2) \\ & + \alpha \Psi(x_1, x_2 - 1) + \beta \Psi(x_1, x_2 + 1) \\ & - 2(\alpha + \beta) \Psi(x_1, x_2). \end{aligned} \quad (4.45)$$

The reflecting boundaries are

$$\alpha \Psi(0, x_2) = \beta \Psi(1, x_2), \quad (4.46a)$$

$$\alpha \Psi(x_1, L) = \beta \Psi(x_1, L + 1). \quad (4.46b)$$

For the case of more than one particle, we need to take into account the exclusion effect, i.e., one site can be occupied by at most one particle. Mathematically, it can be written as an additional boundary condition

$$\alpha \Psi(x, x) + \beta \Psi(x + 1, x + 1) = (\alpha + \beta) \Psi(x, x + 1). \quad (4.47)$$

Notice that the exclusive condition must hold for any x . The notation of $\Psi(x, x)$ may look strange, but we keep in mind that it is a boundary condition that denotes the limiting situation $x_1 = x_2$. We can understand it in the same way of understanding the “ghost coordinate”. In appendix D for a detailed derivation of Eq. (4.47) is given.

To construct the Bethe ansatz solution, we summarize the eigenfunctions Eq. (4.35) and Eq. (4.36) into a set and rewrite them as following:

$$\psi(x) \in \left\{ \psi_s(x), \psi_{ns}(x) \right\} = \left\{ A \left(\frac{\alpha}{\beta} \right)^x, \left(\frac{\alpha}{\beta} \right)^{\frac{x}{2}} (A_+ e^{ipx} + A_- e^{-ipx}) \right\}, \quad (4.48)$$

where ψ_s and ψ_{ns} represent stationary eigenfunction and non-stationary eigenfunctions respectively. A , A_+ , A_- are amplitude coefficients, p is the wave vector of excited

eigenmodes. In case of single particle above, these coefficients can be fixed by applying the boundary conditions Eq. (4.30). Here, however, we keep them arbitrary and use the general form to construct the Bethe ansatz solution. Boundary conditions can be imposed afterwards and all arbitrary coefficients can be solved then.

The idea to construct the two-particle solution is inspired by the standard Coordinate Bethe ansatz. However, instead of using the plane wave function as building blocks, we use $\psi(x)$ drawn from Eq. (4.48) here. The ansatz for $\Psi(x_1, x_2)$ reads

$$\Psi(x_1, x_2) = \psi_1(x_1)\psi_2(x_2) + \tilde{\psi}_2(x_1)\tilde{\psi}_1(x_2). \quad (4.49)$$

Since there are two particles in the system, we have ψ_1 and ψ_2 in the ansatz. The functional form of ψ_1 and ψ_2 can be drawn from the set of Eq. (4.48), either in stationary form ψ_s or in non-stationary form ψ_{ns} . However, the argument variable of ψ_1 and ψ_2 can be either x_1 or x_2 . In general, one has $N!$ ways to permute the function ψ_n and the argument variable x_n . In the case of $N = 2$, there are only two ways.

We classify $\psi_1, \tilde{\psi}_1$ as one class and $\psi_2, \tilde{\psi}_2$ as the other class. Functions in the same class (e.g. ψ_1 and $\tilde{\psi}_1$) share the same functional form but different amplitude coefficients. For example, $\psi_1(x_1) = \left(\frac{\alpha}{\beta}\right)^{\frac{x_1}{2}} (A_{1+}e^{ip_1x_1} + A_{1-}e^{-ip_1x_1})$ and $\tilde{\psi}_1(x_2) = \left(\frac{\alpha}{\beta}\right)^{\frac{x_2}{2}} (\tilde{A}_{1+}e^{ip_1x_2} + \tilde{A}_{1-}e^{-ip_1x_2})$. In general $A_{1+} \neq \tilde{A}_{1+}$ and $A_{1-} \neq \tilde{A}_{1-}$, but ψ_1 and $\tilde{\psi}_1$ share the same functional form ψ_{ns} and the same wave vector p_1 . It is important that ψ_n and $\tilde{\psi}_n$ might have different amplitude coefficients. The main idea is to tune these amplitude coefficients so that $\Psi(x_1, x_2)$ satisfies the reflecting boundaries Eq. (4.46) and the exclusive condition Eq. (4.47).

With the ansatz Eq. (4.49), the remaining task is to impose the constraints Eq. (4.46) and Eq. (4.47) and fix amplitude coefficients as well as the wave vectors. There are three types of $\Psi(x_1, x_2)$ depending on the combination of the two constructed classes: both stationary, both non-stationary and the mixed type with one stationary and the other non-stationary. In the following paragraph, we will discuss these cases separately.

Both stationary

Let us first check the case when $\Psi(x_1, x_2)$ is constructed by only ψ_s , namely $\psi_1(x) = A_1 \left(\frac{\alpha}{\beta}\right)^x$, $\psi_2(x) = A_2 \left(\frac{\alpha}{\beta}\right)^x$, $\tilde{\psi}_1(x) = \tilde{A}_1 \left(\frac{\alpha}{\beta}\right)^x$, $\tilde{\psi}_2(x) = \tilde{A}_2 \left(\frac{\alpha}{\beta}\right)^x$. Plugging in to (4.49) we obtain

$$P^e(x_1, x_2) = \Psi(x_1, x_2) = A \left(\frac{\alpha}{\beta}\right)^{x_1+x_2}, \quad (4.50)$$

where $A = A_1\tilde{A}_1 + A_2\tilde{A}_2$. One can readily check that Eq. (4.50) is exactly the stationary eigenfunction of the two-particle system as expected, the corresponding

eigenvalue being $\Lambda_s = 0$. The reflecting boundaries Eq. (4.46) and the exclusive condition Eq. (4.47) are both fulfilled.

The prefactor A can be fixed by normalization. However, it is not a trivial work because of the constraint $x_1 < x_2$. We postpone the discussion of normalization to the N -particle solution later.

Mixed non-stationary

The mixed type is a non-stationary eigenmode. Without loss of generality, we choose $\{\psi_1(x), \tilde{\psi}_1(x)\}$ to be in the stationary form ψ_s , then $\Psi(x_1, x_2)$ can be written as

$$\begin{aligned} \Psi(x_1, x_2) = & A_1 \left(\frac{\alpha}{\beta}\right)^{x_1} \left(\frac{\alpha}{\beta}\right)^{\frac{x_2}{2}} (A_{2+} e^{ip_2 x_2} + A_{2-} e^{-ip_2 x_2}) \\ & + \tilde{A}_1 \left(\frac{\alpha}{\beta}\right)^{x_2} \left(\frac{\alpha}{\beta}\right)^{\frac{x_1}{2}} (\tilde{A}_{2+} e^{ip_2 x_1} + \tilde{A}_{2-} e^{-ip_2 x_1}). \end{aligned} \quad (4.51)$$

Plugging Eq. (4.51) in to the master equation, we can find the corresponding eigenvalue. Plug it in to the reflecting boundaries and exclusive condition, A_1 , \tilde{A}_1 , $A_{2\pm}$ and $\tilde{A}_{2\pm}$ can be tuned to fulfill these conditions. Consistency condition gives us the Bethe equation for the wave vector p_2 .

We first insert the solution Eq. (4.51) to the master equation Eq. (4.45), obtaining the corresponding eigenvalue:

$$\Lambda = -(\alpha + \beta) + 2\sqrt{\alpha\beta} \cos(p_2), \quad (4.52)$$

where p_2 is the wave vector to be determined. Accordingly, the reflecting condition Eq. (4.46) gives us

$$\frac{A_{2+}}{A_{2-}} = -\frac{(\alpha - \sqrt{\alpha\beta} e^{-ip_2}) e^{-ip_2 L}}{(\alpha - \sqrt{\alpha\beta} e^{ip_2}) e^{ip_2 L}}, \quad (4.53a)$$

$$\frac{\tilde{A}_{2+}}{\tilde{A}_{2-}} = -\frac{\alpha - \sqrt{\alpha\beta} e^{-ip_2}}{\alpha - \sqrt{\alpha\beta} e^{ip_2}}. \quad (4.53b)$$

We now check the exclusive condition Eq. (4.47). Substituting Eq. (4.51) into Eq. (4.47), we find that

$$\frac{A_1 A_{2+}}{\tilde{A}_1 \tilde{A}_{2+}} = -\frac{\alpha e^{ip_2} - (\alpha + \beta) \sqrt{\frac{\alpha}{\beta}} + \sqrt{\alpha\beta}}{\alpha e^{ip_2} - (\alpha + \beta) e^{ip_2} + \sqrt{\alpha\beta}}, \quad (4.54a)$$

$$\frac{A_1 A_{2-}}{\tilde{A}_1 \tilde{A}_{2-}} = -\frac{\alpha e^{-ip_2} - (\alpha + \beta) \sqrt{\frac{\alpha}{\beta}} + \sqrt{\alpha\beta}}{\alpha e^{-ip_2} - (\alpha + \beta) e^{-ip_2} + \sqrt{\alpha\beta}}. \quad (4.54b)$$

Finally, using the consistency condition that

$$\begin{pmatrix} \tilde{A}_{2+} \\ \tilde{A}_{2-} \end{pmatrix} \begin{pmatrix} A_{2-} \\ A_{2+} \end{pmatrix} = \begin{pmatrix} \tilde{A}_1 \tilde{A}_{2+} \\ A_1 A_{2+} \end{pmatrix} \begin{pmatrix} A_1 A_{2-} \\ \tilde{A}_1 \tilde{A}_{2-} \end{pmatrix}, \quad (4.55)$$

we obtain the Bethe equation

$$e^{i2p_2 L} = 1. \quad (4.56)$$

Solving the equation we get $p_2 = \frac{k\pi}{L}$. Plugging it into the eigenvalues Eq. (4.52), we note that the eigenvalues are exactly the same as the those of the single particle case. Now, we can re-substitute the solution of p_2 into Eq. (4.53) and Eq. (4.54) to get the corresponding eigenfunctions. The results of this type of non-stationary eigenvalues and corresponding eigenfunctions are summarized as follows

$$\Lambda_k = -(\alpha + \beta) + 2\sqrt{\alpha\beta} \cos\left(\frac{k\pi}{L}\right), \quad k = 1, 2, \dots, L-1; \quad (4.57a)$$

$$\Psi_k(x_1, x_2) = A \left[\frac{\alpha}{\beta} \left(\frac{\alpha}{\beta}\right)^{x_1} \phi_k(x_2) + \left(\frac{\alpha}{\beta}\right)^{x_2} \phi_k(x_1) \right]. \quad (4.57b)$$

Here $\phi_k(x)$ are the single particle non-stationary eigenfunctions and A is a constant normalization coefficient.

Both non-stationary

We now turn to non-stationary eigenmodes constructed by both non-stationary classes of single particle modes. The number of remaining unknown eigenfunctions and eigenvalues in this case is $L(L-1)/2 - L$. Let us first write down the ansatz:

$$\begin{aligned} \Psi(x_1, x_2) = & \left(\frac{\alpha}{\beta}\right)^{\frac{x_1+x_2}{2}} \left[(A_{1+} e^{ip_1 x_1} + A_{1-} e^{-ip_1 x_1}) (A_{2+} e^{ip_2 x_2} + A_{2-} e^{-ip_2 x_2}) \right. \\ & \left. + \left(\tilde{A}_{1+} e^{ip_1 x_2} + \tilde{A}_{1-} e^{-ip_1 x_2} \right) \left(\tilde{A}_{2+} e^{ip_2 x_1} + \tilde{A}_{2-} e^{-ip_2 x_1} \right) \right]. \end{aligned} \quad (4.58)$$

Plugging it in to the master equation, we get the corresponding eigenvalues as

$$\Lambda = \sum_{n=1}^2 \left[-(\alpha + \beta) + 2\sqrt{\alpha\beta} \cos(p_n) \right]. \quad (4.59)$$

Plugging it in to the reflecting boundaries, we obtain

$$\frac{A_{1+}}{A_{1-}} = -\frac{\alpha - \sqrt{\alpha\beta}e^{-ip_1}}{\alpha - \sqrt{\alpha\beta}e^{ip_1}}; \quad (4.60a)$$

$$\frac{\tilde{A}_{1+}}{\tilde{A}_{1-}} = -\frac{(\alpha - \sqrt{\alpha\beta}e^{-ip_1})e^{-ip_1L}}{(\alpha - \sqrt{\alpha\beta}e^{ip_1})e^{ip_1L}}; \quad (4.60b)$$

$$\frac{\tilde{A}_{2+}}{\tilde{A}_{2-}} = -\frac{\alpha - \sqrt{\alpha\beta}e^{-ip_2}}{\alpha - \sqrt{\alpha\beta}e^{ip_2}}; \quad (4.60c)$$

$$\frac{A_{2+}}{A_{2-}} = -\frac{(\alpha - \sqrt{\alpha\beta}e^{-ip_2})e^{-ip_2L}}{(\alpha - \sqrt{\alpha\beta}e^{ip_2})e^{ip_2L}}. \quad (4.60d)$$

To simplify the notation, we define the function $a(p, p') := \sqrt{\alpha\beta}e^{i(p+p')} - (\alpha + \beta)e^{ip} + \sqrt{\alpha\beta}$. Then the exclusive condition gives

$$\frac{A_{1+}A_{2+}}{\tilde{A}_{1+}\tilde{A}_{2+}} = -\frac{a(p_1, p_2)}{a(p_2, p_1)}; \quad (4.61a)$$

$$\frac{A_{1+}A_{2-}}{\tilde{A}_{1+}\tilde{A}_{2-}} = -\frac{a(p_1, -p_2)}{a(-p_2, p_1)}; \quad (4.61b)$$

$$\frac{A_{1-}A_{2+}}{\tilde{A}_{1-}\tilde{A}_{2+}} = -\frac{a(-p_1, p_2)}{a(p_2, -p_1)}; \quad (4.61c)$$

$$\frac{A_{1-}A_{2-}}{\tilde{A}_{1-}\tilde{A}_{2-}} = -\frac{a(-p_1, -p_2)}{a(-p_2, -p_1)}. \quad (4.61d)$$

The similar consistency conditions as Eq. (4.55) give the following Bethe equation:

$$e^{i2p_1L} = \frac{a(p_1, p_2)}{a(p_2, p_1)} \frac{a(p_2, -p_1)}{a(-p_1, p_2)}; \quad (4.62a)$$

$$e^{i2p_2L} = \frac{a(p_2, p_1)}{a(p_1, p_2)} \frac{a(p_1, -p_2)}{a(-p_2, p_1)}. \quad (4.62b)$$

Now it would be interesting to interpret the Bethe Equation and compare it with the well known Bethe Equation of ASEP with periodic boundaries (see in Appendix E). The interpretation can be useful to derive N -particle Bethe Equations. We can interpret Eq. (4.60) as a reflector that reflects the particle and change the direction of wave vector, i.e., $p_n \leftrightarrow -p_n$. Meanwhile, Eq. (4.61) can be interpreted as a permutator that permutes two neighboring particles $n \leftrightarrow (n + 1)$. Imagine particle 1 starts from the left side of the lattice and then permutes with all the particle on its right side until it reaches the right boundary (in the case of two particles, only one particle is found at the right side of particle 1), and then is reflected by the boundary, becomes a particle traveling in the opposite direction, and then permutes with all the left side

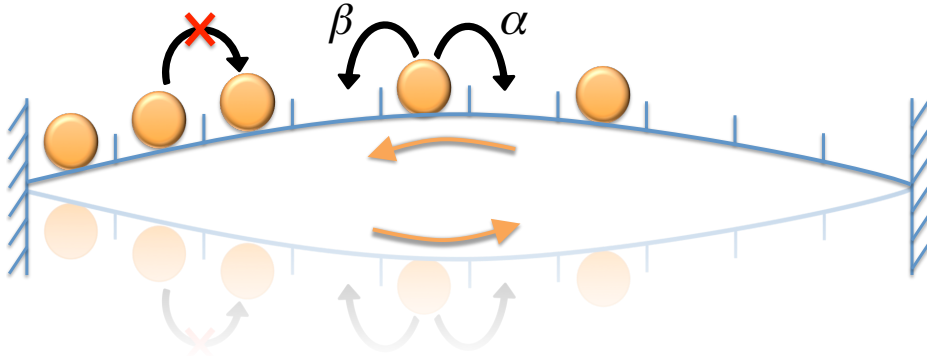


Figure 4.6: The interpretation for the Bethe Equations of the reflecting ASEP as if it is a periodic ASEP system.

particles until it reaches the left side boundary, and then reflects again, which recovers the initial state. A schematic diagram of this process is shown in Fig. 4.6. In this sense, the particle works as if it is sitting on a lattice with periodic boundary. Using this interpretation and the well known result of periodic Bethe Equation (see in Appendix E), one can easily recover exactly Eq. (4.62).

By solving the Bethe equation Eq. (4.62), one can get p_1 and p_2 and thus all amplitude coefficients up to a constant normalization factor. Then Eq. (4.59) gives the eigenvalues and Eq. (4.58) gives the eigenfunctions. Unfortunately, it might not be possible to solve the Bethe equation analytically. So we resort to numerical solutions. We have verified the resulting eigenvalues and eigenfunctions by comparing with the results from brute force diagonalization of the transition matrix for small system size $L \leq 10$.

To summarize, the complete solution of two-particle hopping system with reflecting boundaries is found. The solution is shown in the form of eigenfunction expansion, i.e. Eq. (4.45). The stationary eigenfunction with eigenvalue $\Lambda_0 = 0$ is listed as Eq. (4.50), while the two types of non-stationary eigenvalues and corresponding eigenfunctions are listed in Eq. (4.52), (4.59) and Eq. (4.51), (4.58), respectively. They can be fully determined by solving the Bethe Equation Eq. (4.56) and Eq. (4.62). Part of them are analytically shown in Eq. (4.57).

Finally, we would like to make some remarks here. Firstly, as one can see from Eq. (4.57) that the eigenvalues of two-particle system always contain the eigenvalues of the single particle system. We can show later this can be generalized such that the eigenvalues of $N + 1$ particle system always contain the eigenvalues of N particle system for $N < L/2$. Secondly, the relaxation time of the system is related to the second largest eigenvalue Λ_1 . Eq. (4.57) suggests $\Lambda_1 = -(\alpha + \beta) + 2\sqrt{\alpha\beta} \cos(\frac{\pi}{L})$. However, since there is no analytical solution for all Bethe Equations, it is difficult to rigorously prove that. Numerical evidence is provided to verify the conjecture. In the next subsection, we generalize the solution to the N particle system. The procedure

is quite straightforward after we solved the two-particle case.

4.3.3 Solution of general N particles

Now we consider the system with N particles. Notice that, $N = L/2$ has to be set considering the mapping to polymer loop. However, our method of finding solution works for arbitrary N . As before, we first write down the master equation of a N particles system:

$$\frac{dP(x_1, \dots, x_N; t)}{dt} = \sum_{j=1}^N [\alpha P(\dots, x_j - 1, \dots; t) + \beta P(\dots, x_j + 1, \dots; t) - (\alpha + \beta)P(\dots, x_j, \dots; t)] \quad (4.63)$$

Similarly, after the eigenfunction expansion the reflecting boundaries can be written as

$$\alpha\Psi(0, x_2, \dots, x_N) = \beta\Psi(1, x_2, \dots, x_N) \quad (4.64a)$$

$$\alpha\Psi(x_1, \dots, x_{N-1}, L) = \beta\Psi(x_1, \dots, x_{N-1}, L + 1) \quad (4.64b)$$

The exclusive condition for N particles case is more tricky. In principle, one has to consider the case of three body collision, four body collision and so on. Luckily, in the simple model of ASEP, one can prove that these many body exclusive conditions are not new but just linear recombination of two body exclusive conditions. For example, the three body exclusive condition of particles denoted by 1, 2, 3 can be written as the sum of two body exclusive conditions of 1, 2 and 2, 3. Consequently, the exclusive condition of a N -particle system can be written as

$$\alpha\Psi(\dots, x, x, \dots) + \beta\Psi(\dots, x + 1, x + 1, \dots) = (\alpha + \beta)\Psi(\dots, x, x + 1, \dots) \quad (4.65)$$

The reason that the exclusive condition can be written in such a simple way originates from the Yang-Baxter Equation, which encodes the integrability of the ASEP system [126].

Stationary mode

Intuitively, we construct the N particles stationary solution as

$$P^e(x_1, x_2, \dots, x_N) = \Psi(x_1, x_2, \dots, x_N) = A \prod_{j=1}^N \left(\frac{\alpha}{\beta}\right)^{x_j}. \quad (4.66)$$

One can plug it in the master equation to check that the corresponding eigenvalue is $\Lambda_s = 0$, and also verify the exclusive condition as well as the reflecting boundaries are

fulfilled by inserting the solution into Eq. (4.65) and Eq. (4.64) separately.

We now try to fix the parameter A by normalization. Let us denote $q := \frac{\alpha}{\beta}$, then we can write A as following

$$A^{-1} = \sum_{\Omega} q^{\sum_j x_j} = \sum_{x_1 < x_2 < \dots < x_N} q^{\sum_j x_j}. \quad (4.67)$$

Let us do a variable change so that

$$K = \sum_j x_j - K_0,$$

where $K_0 = 1 + 2 + \dots + N = N(N+1)/2$. It is easy to see that K is an integer in the range of $0, 1, \dots, N(L-N)$. Eq. (4.67) can be rewritten as

$$A^{-1} = q^{K_0} \sum_{K=0}^{N(L-N)} g(K) q^K, \quad (4.68)$$

where $g(K)$ is the number of partitions of positive integer K to N parts with each part having maximum possible value $L-N$. From the number partition theory, we identify

$$\sum_{K=0}^{N(L-N)} g(K) q^K = \binom{L}{N}_q = \frac{[L]_q!}{[L-N]_q! [N]_q!}, \quad (4.69)$$

where $[N]_q = 1 + q + q^2 + \dots + q^{N-1}$ is a q number, and Eq. (4.69) is a q -binomial coefficient [162]. Finally, we arrive at

$$P^e(x_1, x_2, \dots, x_N) = q^{-\frac{N(N+1)}{2}} \binom{L}{N}_q^{-1} \prod_{j=1}^N q^{x_j}. \quad (4.70)$$

The above equation is exactly the same as the Eq. (3.28) in Section 3.2, where a different approach is used. Also, in [137], Schütz used a quantum group formalism to obtain the same result with a different notation.

Non-stationary modes

Inspired by the calculation of two particles case, we try to find the Bethe solution of the N particles system by taking the following ansatz:

$$\Psi(x_1, x_2, \dots, x_N) = \sum_{\sigma \in S_N} \prod_{n=1}^N \psi_n^\sigma(x_{\sigma(n)}), \quad (4.71)$$

where S_N is the group of permutations of N elements and ψ_n^σ is the building block function drawn from Eq. (4.48), either stationary or non-stationary. The subscript n denotes the index of class in which all functions share the same functional form and wave vector p_n . For example, in the notation of the two-particle case, $\{\psi_1, \tilde{\psi}_1\}$ is the class with index $n = 1$. Notice that $n \in \{1, 2, \dots, N\}$ and N is the total number of particles in the system. The superscript σ is the N -element index arrangement used to distinguish different functions in one class, which is equivalent to the tilde notation in two-particle case. These functions are different by the amplitude coefficients A_n^σ or $A_{n\pm}^\sigma$ depending on whether it is a stationary or a non-stationary class. For example, in the two-particle case, the class $n = 1$ contains two functions with coefficients $\{A_1^{12}, A_1^{21}\}$ or $\{A_{1\pm}^{12}, A_{1\pm}^{21}\}$.

Now, we assume Eq. (4.71) is constructed by N_s functions ψ_s from the stationary class and $N - N_s$ non-stationary ψ_{ns} . Notice that $N_s = 0$ corresponds to the both non-stationary type in the two-particle system, and $1 < N_s < N$ corresponds to the mixed non-stationary type. We discuss them separately here.

Inserting the ansatz Eq. (4.71) into the master equation Eq. (4.63), we obtain the corresponding eigenvalue

$$\Lambda = \sum_{n=1}^{N-N_s} \lambda_n, \quad (4.72)$$

where $\lambda_n = -(\alpha + \beta) + 2\sqrt{\alpha\beta} \cos(p_n)$. Notice that, as in the case of two-particle system, p_n can be determined by the Bethe Equations which is discussed in the following. The eigenvalues can be obtained according to Eq. 4.72. In general, there are more than one solution because Bethe Equations are nonlinear, and different solution can lead to different eigenvalues.

In the case of $N_s = 0$, plugging Eq. (4.71) into the reflecting boundaries Eq. (4.64) we can obtain

$$\frac{A_{n+}^{\sigma|\sigma(1)=n}}{A_{n-}^{\sigma|\sigma(1)=n}} = -\frac{\alpha - \sqrt{\alpha\beta}e^{-ip_n}}{\alpha - \sqrt{\alpha\beta}e^{ip_n}}, \quad (4.73a)$$

$$\frac{A_{n+}^{\sigma|\sigma(N)=n}}{A_{n-}^{\sigma|\sigma(N)=n}} = -\frac{(\alpha - \sqrt{\alpha\beta}e^{-ip_n})e^{-ip_n L}}{(\alpha - \sqrt{\alpha\beta}e^{ip_n})e^{ip_n L}}. \quad (4.73b)$$

Substituting the ansatz in the exclusive condition Eq. (4.65) we get

$$\frac{A_{n\pm}^\sigma A_{(n+1)\pm}^\sigma}{A_{n\pm}^{\sigma|n \leftrightarrow n+1} A_{(n+1)\pm}^{\sigma|n \leftrightarrow n+1}} = -\frac{a(\pm p_n, \pm p_{n+1})}{a(\pm p_{n+1}, \pm p_n)}, \quad (4.74)$$

where $a(p, p') = \sqrt{\alpha\beta}e^{i(p+p')} - (\alpha + \beta)e^{ip} + \sqrt{\alpha\beta}$. Then one can either use the consistency condition or the interpretation of the Bethe Equations we discussed in the two-particle case and the well known periodic Bethe Equation, the following set of Bethe Equations

for the N particles system can be obtained:

$$e^{i2p_n L} = \prod_{m \neq n}^N \frac{a(p_n, p_m) a(p_m, -p_n)}{a(p_m, p_n) a(-p_n, p_m)}. \quad (4.75)$$

By solving Eq. (4.75) we get all the p_n and then one can plug them back in Eq. (4.72) and Eq. (4.71) for the corresponding eigenvalues and eigenfunctions.

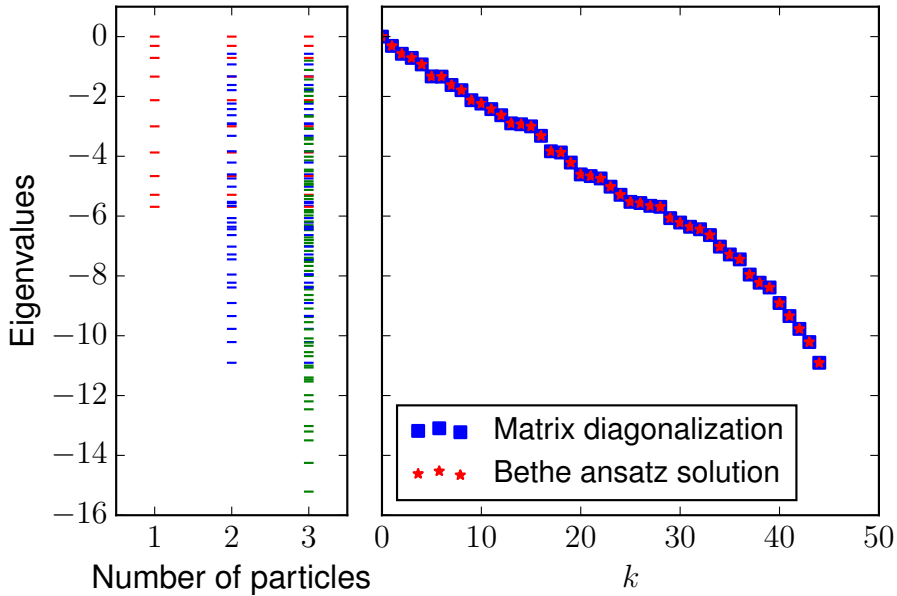


Figure 4.7: The left panel: the embedding structure of eigenvalues illustrated by a system of $L = 10$ with one, two and three particles. The right panel: eigenvalue obtained from brute force digitalization of Markov matrix and from the Bethe equations. $\alpha = 2$, $\beta = 1$, $L = 10$ for both panel and $N = 2$ for the right panel.

Now let us discuss the case that $0 < N_s < N$. The calculation of the two-particle system is a good illustration. We can easily find that there is nothing different except we have only $N - N_s$ wave vectors and $2N - N_s$ amplitude coefficients. So one just need to use the relation similar to Eq. (4.54) together with Eq. (4.73) to build the Bethe Equations. Moreover, Eq. (4.56) suggests that the obtained Bethe Equations are exactly the same as the Bethe Equations of a $N - N_s$ particle system with all non-stationary type building block functions ψ_{ns} . According to Eq. (4.72) for the eigenvalues, we can conclude that the eigenvalues of $N - N_s$ particles system are always contained in the eigenvalue set of the N -particle system. Notice that this is only true for $N < L/2$. For $N > L/2$, one can use the particle-hole duality which means that the eigenvalue of N particle system should be the same as the $L - N$ particle system. This important structure of the solution explains our simulation results in

Section 4.2.2.

This kind of embedding structure is verified by our simulations. In Fig. 4.7, we show in the left panel that eigenvalues of case $N = 1$ are contained in the set of eigenvalues $N = 2$, and all eigenvalues of case $N = 2$ are contained in the set of $N = 3$. In the right panel, the eigenvalues obtained from the brute force diagonalization of the Markov matrix are compared with those from the solution of the Bethe Equations Eq. (4.75). We can see that they are identical to each other.

Finally, we remark that one has to solve the Bethe Equations numerically in most cases. However, there is a small set of non-stationary eigenvalues and eigenvectors we can obtain analytically, which correspond to the case of only one excitation mode. The results are summarized as follows:

$$\Lambda_k = -(\alpha + \beta) + 2\sqrt{\alpha\beta} \cos\left(\frac{k\pi}{L}\right), \quad k = 1, 2, \dots, L - 1; \quad (4.76a)$$

$$\Psi_k(x_1, x_2, \dots, x_N) = A \sum_{n=1}^N \left(\frac{\alpha}{\beta}\right)^{n-1} \phi_k(x_n) \prod_{m \neq n} \left(\frac{\alpha}{\beta}\right)^{x_m}. \quad (4.76b)$$

Notice that this set of eigenvalues is exactly the single particle spectrum, and again $\phi_k(x)$ is exactly the single particle eigenfunction. Fortunately, the numerical evidence shows that the most interesting eigenmode, i.e. the slowest relaxation mode, is contained in this set. We discuss it in the following subsection.

4.3.4 Relaxation time

With the complete Bethe solution of the reflecting ASEP system, the relaxation time can be calculated. Here, we first discuss the relaxation time of the ASEP system and then map it back to the relaxation of the polymer system.

Relaxation time of the reflecting ASEP

The relaxation time of the ASEP system is determined by the second largest eigenvalue of the Markov matrix. In principle, one has to solve all the Bethe equations to obtain the second largest eigenvalue. However, it is a difficult task to solve them all analytically except the single excitation mode listed in Eq. (4.76). The second largest eigenvalue can be written down explicitly in the single particle case, which is

$$\Lambda_1 = -(\alpha + \beta) + 2\sqrt{\alpha\beta} \cos\left(\frac{\pi}{L}\right). \quad (4.77)$$

We argue that Eq. (4.77) is the second largest eigenvalue of general N -particle cases. On one hand, this conjecture can be verified by our simulation results. Two facts from the simulation results support the conjecture. The first one is the relaxation time of a reflecting ASEP system does not depend on the particle number. The second one lies

on the eigenvalues structure obtained from brute force digitalization of the Markov matrix. On the other hand, for the continuous limit of ASEP with particle density N/L , which corresponds to a single file diffusion process, we can prove Eq. (4.77) is truly the second largest eigenvalue (see Appendix F). In addition, Labbé et. al. studied the mixing time problem of the reflecting ASEP and found the same second largest eigenvalue as in Eq. (4.77) using a hydrodynamical approach [174]. Thus we are confident that Eq. (4.77) is indeed the second largest eigenvalue of general N -particle systems. If we assume $L \gg 1$, Eq. (4.77) can be expanded as

$$\Lambda_1 = -(\sqrt{\beta} - \sqrt{\alpha})^2 - \frac{\sqrt{\alpha\beta}\pi^2}{L^2} \quad (4.78)$$

Then the relaxation time can be calculated as $\tau = -\frac{1}{\Lambda_1}$.

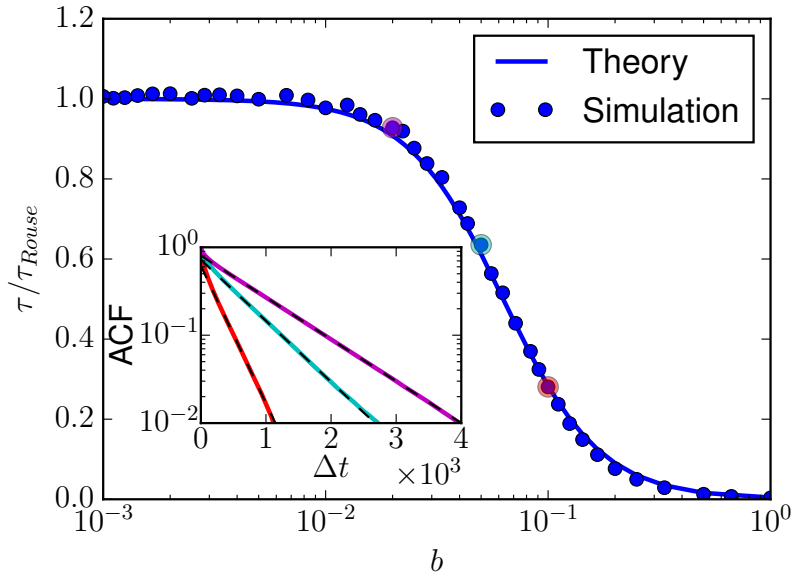


Figure 4.8: Relaxation time of 1D reflecting ASEP varies with the hopping bias defined in Eq. (4.26). The relaxation time is normalized with the Rouse relaxation time. The ACF curves for several typical cases are shown in the inset. The corresponding relaxation time is fitted and show with dashed black lines, which are also marked with the cycle of the same color in the simulation dots.

We now discuss the strong and weak hopping bias regime separately. For strong bias $\beta \gg \alpha$, then $\Lambda_1 \rightarrow -\beta$ and the relaxation time is $\tau \rightarrow 1/\beta$. So the relaxation time of the system tends to be a constant which is independent of the system size. Moreover, the relaxation time $\tau \rightarrow 0$ as $\beta \rightarrow \infty$. In the weak bias $\alpha \approx \beta$, we can obtain $\tau \approx \frac{L^2}{\sqrt{\alpha\beta}\pi^2}$. The scaling $\tau \sim L^2$ means the dynamical exponent of the system is 2. The result of relaxation time as a function of hopping bias is shown in Fig. 4.8. The Kinetic Monte Carlo results are compared with the theory and we find that they match

well to each other. The asymptotic behaviors of strong and weak bias are illustrated to be consistent with our analysis above. The autocorrelation function (ACF) used for extracting the relaxation time is shown in the inset for several typical cases of hopping bias.

Map back to 1D polymer

Now, we can re-map the ASEP model back to the picture of polymer dynamics to discuss the relaxation time of 1D polymer model. Utilizing Eq. (4.24) and plugging it into Eq. (4.77), the relaxation time can be calculated explicitly.

$$\tau = \frac{\xi a^2}{k_B T} \frac{1}{\exp\left(\frac{\Delta E}{k_B T}\right) + \exp\left(-\frac{\Delta E}{k_B T}\right) - 2 \cos\left(\frac{\pi}{L}\right)}. \quad (4.79)$$

Here, ΔE is the energy of flipping of two neighboring rods to change the orientations, $\Delta E = 2Fa$ in 1D. T is the effective temperature. Since $\exp\left(\frac{\Delta E}{k_B T}\right) + \exp\left(-\frac{\Delta E}{k_B T}\right) \geq 2$, we have

$$\tau \leq \frac{\xi a^2}{4k_B T \sin^2\left(\frac{\pi}{2L}\right)}. \quad (4.80)$$

Expanding the sine term as $L \gg 1$, we get

$$\tau_{max} = \frac{\xi a^2 L^2}{\pi^2 k_B T}. \quad (4.81)$$

The result above can be compared with the prediction of one-dimensional Rouse theory. According to our calculation in Section 4.1, the one-dimensional relaxation time of a pinned polymer loop is 3 times that of the three-dimensional model. We found it is exactly the same with our results here. Also, we note that the Rouse scaling with system size L^2 is recovered.

In Rouse theory, the relaxation time does not depend on external force. In contrast, we have an obvious force dependence of the relaxation time here. This point highlights the fundamental difference between the infinite extensible bead-spring model and the finite extensible bead-rod model. Unfortunately, it is not possible to perform the BD simulation for a one-dimensional bead-rod model since the flipping is not a continuous process. However, the relaxation behavior postulated by Eq. (4.79) can be verified by Kinetic Monte Carlo results shown in Fig. 4.8. Furthermore, we present a comparison of BD simulations and the theory in 3D in the next Section. 4.4.

In this section, we used the generalized Bethe ansatz methods to solve the ASEP model with reflecting boundaries exactly. The stationary distribution obtained here matches to our calculation in Chapter 3. The explicit form of the relaxation time was analyzed in different cases. We then re-mapped it back to the polymer system to discuss the relaxation time of pinned polymer loop in 1D. In contrast to the bead-

spring model, an explicit force dependence of the relaxation time is demonstrated. In the next section, we try to use the results obtained here to further analyze the three-dimensional pinned polymer loop system.

4.4 Dynamics of 3D bead-rod polymer loop

Unlike the 1D model discussed in the previous section, the 3D bead-rod model can be studied directly by the BD simulations. We discuss the BD simulation results in this section and apply the theory obtained in 1D ASEP to explain our observations.

4.4.1 Relaxation time of 3D pinned bead-rod loop

Similar to the 1D model, our main interest of the polymer dynamics is the relaxation time. To measure the relaxation time of the 3D pinned bead-rod polymer loop, we perform the BD simulation using the methods described in Chapter 2. The trajectory of diameter vector, defined as $\mathbf{r}_d = \mathbf{r}_{\frac{L}{2}} - \mathbf{r}_0$, is monitored. Then the autocorrelation function of the diameter vector is calculated to extract the relaxation time. Since \mathbf{r}_d is a three-dimensional vector, we measure both the relaxation time along the external force direction and the relaxation time perpendicular to the external force direction, viz. τ_{\parallel} and τ_{\perp} , respectively.

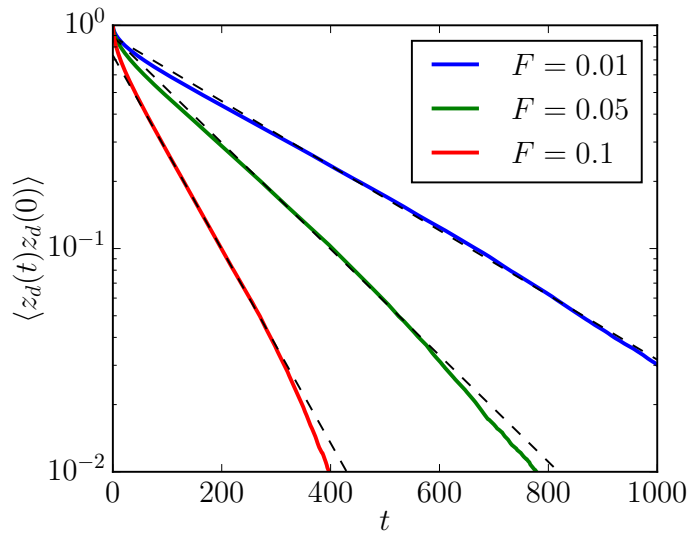


Figure 4.9: Illustration of the autocorrelation function along the external force direction under several cases of different external force. The dashed black lines are the fittings for extraction of relaxation time.

In Fig. 4.9 we show some examples of extracting relaxation time τ_{\parallel} from the auto-

correlation functions (ACF). We can see clearly in the figure, the slope of ACF become steeper when external force increases, which leads to a faster relaxation time.

Based on the simulations, we plot the parallel relaxation time τ_{\parallel} against the strength of external force field, which is shown in Fig. 4.10. One can immediately find that the result is very similar to the 1D theory. Thus we use the theory from the 1D ASEP, and try to match it to the 3D BD simulations.

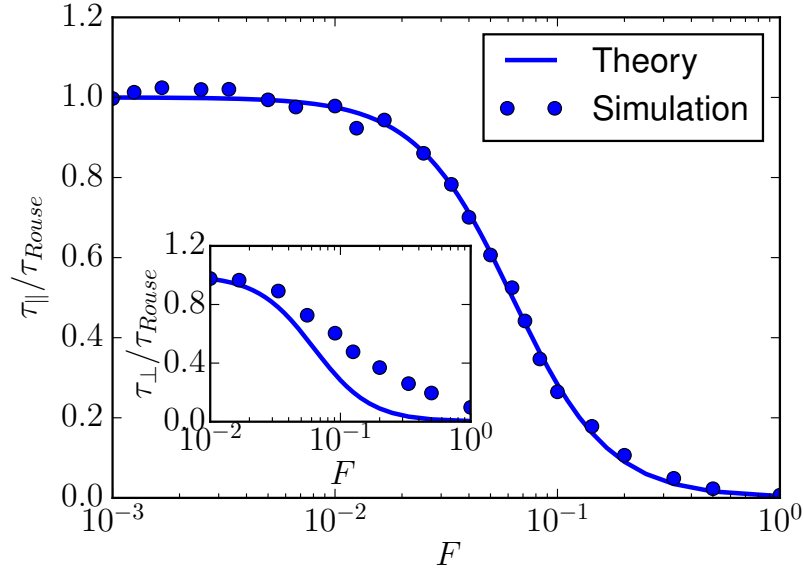


Figure 4.10: Relaxation time along external force direction of pinned 3D bead-rod model varies with the external force. Inset is the relaxation time perpendicular to the external force direction compared with the same theory. $L = 100$ and $T = 1$.

To get insights of the relaxation time for the 3D pinned polymer loop, let us first discuss the case without external force field. In this case, the relaxation time of the 3D pinned polymer loop is correctly predicted by the Rouse theory, we have

$$\tau_{Rouse} = \frac{\xi a^2 L^2}{3\pi^2 k_B T} \quad (4.82)$$

Moreover, for symmetric reasons we have $\tau_{\parallel} = \tau_{\perp} = \tau_{Rouse}$ in this case. This prediction is verified by the BD simulations as shown in Fig. 4.10. Compare Eq. (4.82) with Eq. (4.81), we find that the only difference is the factor 3 in the denominator, which is easy to understand because of the dimensionality of the system.

We now discuss how does the relaxation time vary with the external force. Assuming that τ_{\parallel} varies with external force the same way as in 1D, we can simply divide Eq. (4.77)

by a factor of 3, obtaining:

$$\tau_{\parallel} = \frac{\xi a^2}{3k_B T} \frac{1}{\exp\left(\frac{Fa}{k_B T}\right) + \exp\left(-\frac{Fa}{k_B T}\right) - 2 \cos\left(\frac{\pi}{L}\right)}. \quad (4.83)$$

Here, $\Delta E = Fa$ is used. In 3D, rods can rotate continuously in the space. The orientation is changed when a rod rotates over a length scale of a along the external force field direction. Correspondingly, the energy change is Fa in 3D. Again, we can recover the Rouse limit of the relaxation time by noting $\exp\left(\frac{\Delta E}{k_B T}\right) + \exp\left(-\frac{\Delta E}{k_B T}\right) \geq 2$ and assuming $L \rightarrow \infty$ in Eq. (4.83). The theory of Eq. (4.83) is compared with the simulation results in Fig. 4.10, and we can see an excellent agreement of τ_{\parallel} with the numerical results. However, τ_{\perp} is not well described by the theory as we can see in the inset of Fig. 4.10. Given that it is the relaxation perpendicular to the force field direction, the result is not surprising. Nevertheless, we can still see that τ_{\perp} depends on the external force.

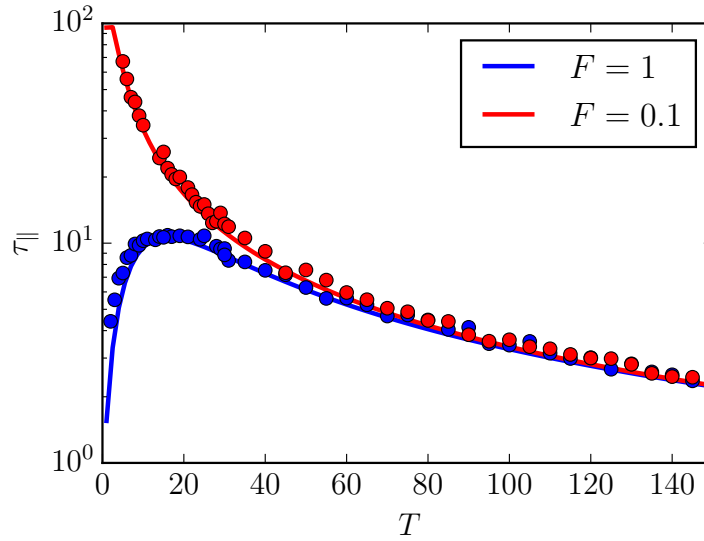


Figure 4.11: Relaxation time of 3D pinned polymer loop varies with the level of noise. Dots are simulation results while solid lines are the theory. $L = 100$.

To further test the theory, we also do the simulation by changing other parameters such as the effective temperature T . Interestingly, according to the prediction of Eq. (4.83), the non-monotonic curve of $\tau_{\parallel}(T)$ can be obtained in a strong external force field. Physically, it means that the relaxation of a bead-rod system is slower if we increase the noise level of the system under a certain force field. It is a counter-intuitive result as one usually expects faster relaxation in a more fluctuating system. However,

the results from the BD simulation verify this prediction, as shown in Fig. 4.11. Meanwhile, we also see in the figure that the non-monotonic behavior disappears when the external force is weak enough.

4.4.2 Stretch coil relaxation

Now, let us discuss the relaxation behavior of two different processes. The first one is that the polymer loop relaxes from a stretched configuration to a coiled configuration when the external force field is stopped at some point. The second one is that the pinned polymer loop relaxes from a coiled configuration to a stretched configuration when the external force field is exerted at a certain point. Experimentally, the measurement of ACF function is more tricky when the fluctuations are relatively small. It is more convenient to measure the stretch-coil transition using the optical tweezer [103, 104].

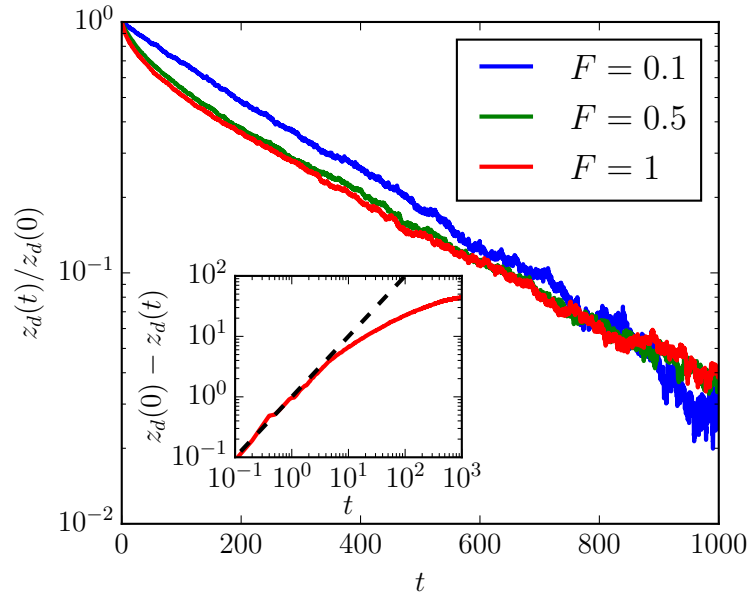


Figure 4.12: The stretch-coil transition of a pinned polymer loop. The relaxation of the middle bead position is monitored for different initial stretched cases. The inset shows the short time relaxation of the polymer initially stretched by external force $F = 1$, dashed black line is a linear fit. $L = 100$, $T = 1$.

From the theoretical point of view, these two transitions are not the same, because one process is under external force field while the other is not. To illustrate more details, we discuss them one by one.

In Fig. 4.12, we show how the free end of a pinned polymer loop, i.e. the middle bead, relaxes to the coiled position. We can see from the figure that the decay is exponential except for the initial part. Moreover, the same slope in the figure indicates that

the relaxation time scale are the same, although the initial states are different. We verified that the time scale here is the same as the Rouse time calculated in Eq. (4.82). However, certain distinctions are also observed between these curves, mainly in the short time regime. As we show in the inset of Fig. 4.12, the initial relaxation of a stretched polymer is linear. Thus the bead moves ballistically with a certain velocity. In contrast, we do not see this regime when the polymer is relaxed from a coiled configuration (see the blue line in Fig. 4.12). The observations can be interpreted as following. Once we stop the external force field, the polymer is driven by an entropic force, which makes the polymer to move ballistically in the initial stage. Moreover, the entropic force is stronger for a stretched polymer and weaker for a coiled polymer. This leads to the more profound linear regime for the relaxation of a stretched polymer.

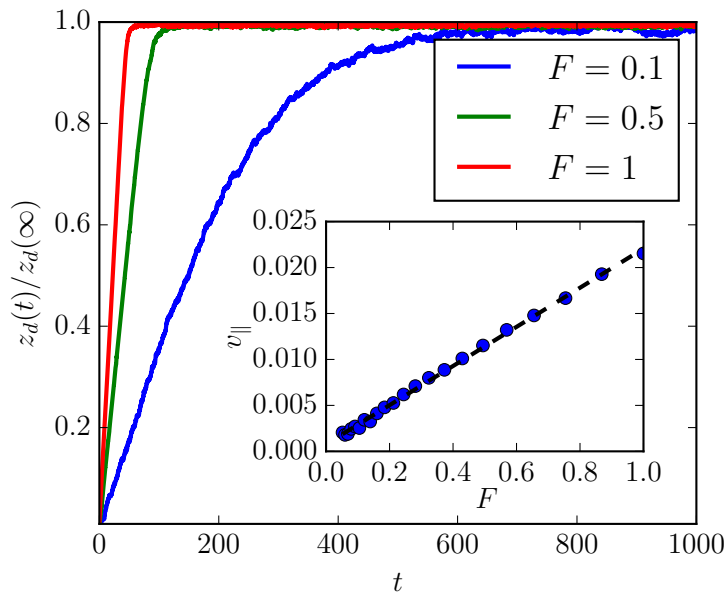


Figure 4.13: The coil-stretch transition of a pinned polymer loop. Here, the polymer is stretched by different force fields. The inset shows the fitted parallel velocity of the middle bead against different external forces. $L = 100$, $T = 1$.

In Fig. 4.13, we show the coil-stretch transition of a pinned polymer loop. The transition can also be divided into two parts. The first part is a ballistic shooting as indicated by the initial linearity of the curves. The second part is again an exponential relaxation to the equilibrium position. However, as we can see from the figure, the ballistic regime dominates for a strong stretching force. In the inset of the figure, we fit the velocity of the ballistic part. As expected, we find that it linearly depends on the external force. The linear regime is reasonable because the effect of the external force field dominates in the early stage, which drives the polymer to move linearly towards the direction of the force field.

In this section, we discussed the relaxation behavior of 3D pinned polymer loops in

an external force field. By 3D BD simulations, we are able to extract the relaxation time of the polymer numerically. We then applied our theory obtained from the reflecting ASEP model to match the relaxation time of the 3D polymer along the force direction. We find that they match well. Moreover, we also discussed the stretch-coil relaxation of the pinned polymer. One linear and one exponential regime were identified for both stretch-coil and coil-stretch transitions.

4.5 Summary

To summarize, we discussed the dynamical properties of pinned polymer loop in a constant external force field in this chapter. More specifically, the relaxation time was discussed in detail.

Firstly, we solved the dynamics of a bead-spring polymer loop using the Rouse theory, which turns out to be the only work for the pinned bead-rod without external force field. Utilizing the mapping from 1D bead-rod to the particle lattice system, the dynamics of the polymer can be mapped to the ASEP on a reflecting lattice. Kinetic Monte Carlo results are shown which indicate that the relaxation time of the system is independent of the total particle number on the lattice. Next, we introduced the generalized Bethe ansatz method to solve exactly the reflecting ASEP system and remapped the analytical results to the polymer system to discuss the relaxation behavior of the pinned polymer loop. Extensive BD simulations were performed and the results match quite well with our theory. Finally, the stretch-coil transition was discussed in the 3D polymer model.

The generalized Bethe ansatz method we used here can be applied to broader systems as long as the total number of particles is conserved. Moreover, since reflecting boundary is one of the typical boundary conditions, we think that it is important to solve it exactly for the celebrated ASEP model from the theoretical point of view. The mapping from polymer dynamics to the ASEP system offers a new way to study the polymer problems. We only discussed here the biologically relevant pinned polymer loop system. The extension of the mapping to other polymer systems is also quite straightforward. In the next chapter, we employ the insights obtained from the theoretical study to discuss the biological system and the known experimental results. Finally, a summary of the whole thesis and some outlooks are provided

Chapter 5

Discussions and Outlook

In preceding chapters, the equilibrium statistics and relaxation dynamics of pinned polymer loop were discussed with a focus on mathematical modeling and numerical simulations. In this chapter, we come back to the biology of fission yeast and discuss the new insights we gained in our study. Here, we also relate some of our results to previous works, both theoretical and experimental. In the last section, we provide a summary of the thesis.

5.1 Discussions

In this section, our discussion is divided into two parts. The first part discusses the biological system of fission yeast, while the second part is devoted to the comparison of our theory to previous results on the pulled polymer systems.

5.1.1 Chromosome pairing and alignment

In the prophase I of fission yeast, the pair of chromosomes is supposed to align in space to undergo recombination between homologous chromosomes, which means the distance between the corresponding loci should be below a certain threshold. This process is important for the correct segregation of homologous chromosomes in the later stage of meiosis I.

The nuclear oscillations period in fission yeast was divided into two pieces of steady motion in our discussions. In addition, the pulled polymer was transferred to the scenario of pinned polymer loops in an external force field. It is reasonable that the chromosome tends to be in a stretched configuration if the external force field is strong. As a result, the statistical distance between two corresponding loci is shortened. Experimentally, two homologous chromosomes are assumed to be aligned when the statistical distance between them is less than 400 nm. It is interesting to ask how does the pulling facilitate the pairing of homologous chromosomes. We now apply our theory to get insights of the pairing problem of chromosomes.

In order to fit our theory to the real biological problem, we need to estimate the number of monomers of our polymer loop model, which would correspond to the chromosomes in fission yeast. Here we focus on the longest chromosome out of the three

in fission yeast. During meiosis, chromosomes are highly condensed. As a consequence, the Kuhn length is large (~ 200 nm). The length of the longest chromosome in base pairs is about 5.58 Mb, and the compact ratio is about 100 bp/nm (see in Table 1.1). So the total number of monomers needed to represent the longest chromosome in our model is about 230.

Our next question is what is the magnitude of the actual pulling force on the monomer in vivo fission yeast. To answer this question, we employ the Stokes' relation $F = 6\pi\eta Rv$. Here, η is the viscosity of nucleoplasm which is listed in Table 1.1, R is the radius of the monomer which can be estimated as half of the Kuhn length $R \approx 100$ nm. The moving velocity $v \approx 2.5\mu\text{m}/\text{min}$ is measured from the experiment. As a result, we can obtain $F \approx 7 \times 10^{-14}$ N.

As mentioned in the first chapter, the nuclear oscillations are driven by the dynein motors. We now ask the question whether the number of motor molecules involved in the nuclear oscillations is sufficient for driving the motion. To answer this question, we first estimate the total force needed for the pulling motion. Using the genomic length of each chromosome listed in Table 1.1, the total number of monomers in fission yeast ~ 1260 can be estimated in the same way of estimating the number of monomers of the longest chromosome. Thus the total pulling force required is $F_{total} \approx 100$ pN. The stall force of dynein motors has been reported within the range of 1 – 7 pN [167, 168]. This corresponds to 14 – 100 dynein motors pulling together. Previous measurements show that there are 50 – 100 dynein motors engaged in the pulling of the SPB [169]. Thus the experimentally observed number of dynein motors is sufficient to generate a force for the alignment of the chromosomes.

Now, let us apply the theory from the equilibrium statistics to discuss the pairing process of the homologous chromosomes. In Section 1.2.2, we calculated the distance between two corresponding beads of the polymer pair with $L = 300$, as illustrated in Fig. 3.9. These two beads are meant to represent the same loci of the homologous chromosomes. The pairing process is supposed to bring them together with a statistical distance less than 400 nm. The theoretical and numerical results of how the distance varies with the dimensionless temperature \tilde{T} was shown in Fig. 3.10. Notice that the $\tilde{T} = k_B T / Fa$ is the only dimensionless parameter in our equilibrium system. \tilde{T} can be considered as the inverse measure of pulling force F if the effective temperature T is fixed. We can clearly see from Fig. 3.10 that the strong external pulling force (small \tilde{T}) significantly decreases the distance between beads. In other words, the model shows that pulling facilitates the chromosome pairing.

The next question is whether the magnitude of external force in fission yeast sufficient for the success pairing of the whole chromosome or not. To answer the question, let us estimate what is the corresponding \tilde{T} in the circumstance of the meiotic fission yeast. It is easy to find $\tilde{T} \approx 0.3$ according to the estimations above. This is a parameter locates at the lower left strong force regime in Fig. 3.10. As we can see from the figure, the distance between corresponding beads is smaller and mostly below the pairing threshold, which is indicated by the shaded area in Fig. 3.10. So the conclusion

is the pulling motion of chromosomes in fission yeast supplies a sufficient force for the pairing.

Now we use our theory to estimate the relaxation time of the longest chromosome. We assume the effective temperature (including the thermal and non-thermal contributions, see in Section 1.2.3) $T = 300$ K, which is near to the room temperature. With these parameters, we are able to calculate the relaxation time of the polymer according to Eq. (4.83). Plugging in the estimated parameters, we can obtain the parallel relaxation time is about 6 seconds. According to our BD simulation results, the transverse relaxation time in such a strong external force regime is about 10 folds of the parallel relaxation time. So the transverse relaxation time is about 1 minute. It is still less than half of the nuclear oscillation time, which is about 5 mins. So the movements of chromosomes toward to one direction can be considered as an equilibrium problem. Our assumption of short relaxation time is justified.

Finally, we have not discussed the role of nuclear envelope during the nuclear oscillations in fission yeast. In contrast to the mammal cell, the nuclear envelope breakdown does not happen in fission yeast during meiosis [170, 171]. The nuclear oscillation happens in the presence of the intact nuclear envelope [170, 171]. However, since there are many nuclear pores in the nuclear membrane and the structure of the membrane is soft [170], we assume that the fluid is freely draining through the nuclear membrane. In other words, the effects of the nuclear membrane is neglected in our model.

To summarize, we can provide some new relevant insights regarding the alignment process of fission yeast chromosomes using the theory of our quantitative model. Next, we want to discuss how our theory is related to previous works.

5.1.2 The blob theory of pulled polymer

Coming from a problem of modeling fission yeast chromosomes during nuclear oscillation, we discussed in this thesis mostly about the pinned polymer loop model. Our study is very special in the sense that the polymers not only retain a loop structure but also pulled by an external force at one point. To the best of our knowledge, no previous study was focused on this specific case. However, the pulled polymer chain model was well studied by F. Brochard-Wyart et al. [96–101]. They developed the blob theory of grafted polymer chains under flow. Three steady-state regimes, namely the unperturbed state, the trumpet regime and the stem-flower regime were found. Before delving into the comparison between our theory and the blob theory, we want to highlight several differences between the setting of these two models.

- Obviously, the looping structure of fission yeast chromosome is a very special case and different from the chain model.
- In our model, we ignore all the complex interactions including the excluded volume effect and hydrodynamic interactions. However, these facts were taken into account in studies of Brochard-Wyart et al. Actually, the hydrodynamic interaction is crucial to formulate the blob theory of pinned chain.

- The ideal polymer with the size scaling $R \sim L^{\frac{1}{2}}a$ is used in our model instead of the Flory scaling $R \sim L^{\frac{3}{5}}a$ [18, 19]. Here L is the number of monomers in the polymer and a is the size of one monomer. The ideal behavior has been claimed in the experiments for DNA under 20 microns [172]. Notice that, the fission yeast chromosomes are exactly in this ideal regime since the size of fission yeast is around 10 microns.

With these notes in mind, we now discuss the results from our model and compare it with the blob theory. In order to do the comparison, it is better to have the blob theory of pinned polymer loops in hand. It is not much different from the pinned polymer chain and is discussed in Appendix G.

The blob theory states that the configuration of the pinned polymer in a flow is composed by a sequence of blobs with increasing size along the flow direction. In a certain regime of external flow, the blobs near to the pinned end vanish to a “stem” structure, while the free end forms a “flower” structure (Fig. 1.7). However, these pictures are the equilibrium configurations. Here, we focus on the relaxation behaviors. The main result of the blob theory for the dynamics is about the stretch-coil transition. For an initially stretched pinned polymer chain, the “stem” starts to retract when the external flow is stopped at some point. The retraction rate scales with time as $l_0 - l \sim t^{1/2}$, where l_0 is the initial length of the “stem”. This scaling was then seen in experiments on stretch-coil relaxation of the free DNA molecules in the Poiseuille flow [173]. In another experiment with a DNA molecule held by an optical tweezer in the flow, a different scaling for the relaxation time was reported $\tau \sim L^{1.66}$ [103, 104] by looking at the stretch-coil transition by turning off the flow.

In comparison, we do not observe the $t^{1/2}$ scaling for stretch-coil transition in our model (Section 4.4). In our model, the relaxation from stretched configuration to coiled one is characterized by an initial ballistic shooting followed by a long exponential decay (Fig. 4.12).

To explain the discrepancies, recall that our model is without excluded volume effect and hydrodynamical interactions. Physically, the results of these interactions slow down the response of the system. So a power law scaling is obtained instead of the exponential decay. Our study of the simple analytically tractable model also stresses the importance of hydrodynamic interactions in modeling chromosomes.

The relaxation time problem was discussed in a very recent work by Labbé and Lacoïn [174]. They solved the problem of mixing time of a biased card shuffling process, which can be mapped to the ASEP with reflecting boundaries. The identical results as Eq. (4.77) was obtained. However, a different approach based on the hydrodynamic limit of ASEP was used and the full eigenfunctions were not reached in their work.

In this section, we used our results to discuss the biological problem of chromosome movements in fission yeast. A comparison of the dynamics of our model to the blob theory was discussed. The distinctions between them highlight the importance of hydrodynamic interactions and excluded volume effect in modeling polymer dynamics. In next section, we summarize the whole thesis and give some outlooks of the future

studies.

5.2 Summary and outlook

To summarize, we investigated the pinned polymer loops in an external force field in order to quantify the chromosome movements in fission yeast during nuclear oscillation. More specifically, the steady state and relaxation dynamics of the pinned polymer loops were studied. The equilibrium statistics were solved analytically by applying the Brownian bridge technique. The relaxation dynamics were solved by mapping the polymer system to the particle-lattice system. The mapped reflecting ASEP was solved exactly and then remapped to the polymer system to discuss the relaxation dynamics. Extensive BD simulations and MC simulations were performed to verify our analytical results.

Many results and techniques developed in this thesis are novel. We believe that they are very useful in the discussion of a large range of problems. For example, the Brownian bridge technique in an external field is useful to discuss any stochastic system with a looping structure. The generalized Bethe ansatz method can be applied to any system with conserved number of particles. Moreover, the exact solution of the reflecting ASEP system we find here complements the knowing results of this important non-equilibrium model. The peculiar mapping from polymer to particle system is also an interesting way to solve both polymer problems and particle problems.

In addition to the work we have discussed in this thesis, there are still a lot of exciting problems waiting for further exploration. We list a few here.

- In Section 3.2, we solved the 1D pinned polymer loop exactly by using the canonical ensemble and number partition theory. In 3D, we have shown in Section 3.3 that the statistics of the equilibrated polymer loop can be obtained using grand canonical ensemble and Brownian bridge condition. It is interesting to find out whether the canonical ensemble method can be extended to the 3D case or not.

- The discussion of mapping the polymer to the particle system is restricted to 1D lattice model in this thesis. However, the generalization of the mapping from 1D to more than 1D is also an exciting issue. In 1D, the two states of rod orientation can be mapped to the two states of lattice site occupation. In a 2D lattice model of polymers, there are four states of the rod orientation. One possible solution is to map them to a multi-species particle-lattice system. However, one has to go much deeper to check whether the idea works or not.

- Most of our discussions in the thesis are about one single pinned polymer loop system. As we known, there are three pairs of chromosomes in fission yeast, but the multiple loops effect should be weak because the excluded volume effect is ignored in our simple model, it can become important when we consider more complex models. So it is interesting to study the inter-loop interactions and the impact of the crowded environment in the future work.

- In this thesis, the nuclear oscillation is divided into two parts of chromosomes moving in opposite directions. We only study the polymers moving with steady speed without changing directions. So our theory is not applicable to discuss the turning process of the nuclear oscillation. We think it is important to model the oscillation behavior as a whole in the future work.

- We have discussed a lot of theoretical insights regarding the meiotic chromosome movements in fission yeast. With the development of experimental techniques such as optical tweezer, it should be possible to manipulate the chromosomes in the lab. Especially the measurement of the relaxation time of the chromosomes should be possible. It would be interesting if we can perform some relevant experiments to test our theory in the future.

To conclude, we presented a theoretical framework in this thesis and established a link between the physics of polymers and statistics of many particle systems. From biological perspective, our theory helps to understand the crucial role of physical forces during nuclear oscillation of meiotic fission yeast.

Appendices

Appendix A

An efficient algorithm to compute pseudo force of bead-rod loop

We have mentioned that the calculation of the *pseudo* force in BD simulation is time-consuming. In fact, a plain algorithm without optimization takes about 80% of the total simulation time. Thus we need to develop an efficient algorithm to calculate the *pseudo* force. Recall that

$$\mathbf{F}_i^{pseudo} = -\frac{1}{2}k_B T \sum_{\alpha,\beta} G_{\beta,\alpha}^{-1} \frac{\partial G_{\alpha\beta}}{\partial \mathbf{r}_i}, \quad (\text{A.1})$$

where G is the metric matrix shown in Eq. (2.19). Notice that G is a symmetric matrix with constant diagonal elements. The summation in Eq. (A.1) can be reduced to the summation of terms with c_1, c_2, \dots, c_L where $c_j = -\mathbf{u}_j \cdot \mathbf{u}_{j-1}$. Thus we can rewrite Eq. (A.1) as

$$\mathbf{F}_i^{pseudo} = k_B T \sum_{j=1}^L G_{j-1,j}^{-1} \frac{\partial \mathbf{u}_j \cdot \mathbf{u}_{j-1}}{\partial \mathbf{r}_i}. \quad (\text{A.2})$$

Again, the periodic indexing is applied for $G_{j-1,j}^{-1}$. The derivative in the sum term of Eq. (A.2) can be evaluated as

$$\frac{\partial \mathbf{u}_j}{\partial \mathbf{r}_i} = \frac{1}{a} (\delta_{i,j} - \delta_{i,j-1}) (\mathbf{I} - \mathbf{u}_j \mathbf{u}_j), \quad (\text{A.3})$$

where \mathbf{I} is the unit tensor. According to Cramer's rule, we can write

$$G_{j-1,j}^{-1} = \frac{\text{cof } G_{j,j-1}}{\det G}, \quad (\text{A.4})$$

where $\text{cof } G_{j,j-1}$ is the cofactor of $G_{j,j-1}$, which is the minus determinant of a $L-1 \times L-1$ sub-matrix. So now we reduce the problem to the calculation of the determinant of a matrix.

To calculate $\det \mathbf{G}$, let us first expand matrix \mathbf{G} by the last line to obtain

$$\det G = -c_L^2 \det \mathbf{S}_1 - c_{L-1}^2 \det \mathbf{S}_2 - 2(-1)^L \prod_{j=1}^L c_j + 2 \det \mathbf{S}_3, \quad (\text{A.5})$$

where \mathbf{S}_1 , \mathbf{S}_2 , \mathbf{S}_3 are symmetric tridiagonal sub-matrices of \mathbf{G} . \mathbf{S}_1 is a $(L-2) \times (L-2)$ sub-matrix with off-diagonal elements c_2, \dots, c_{L-1} , \mathbf{S}_2 is a $(L-2) \times (L-2)$ sub-matrix with off-diagonal elements c_1, \dots, c_{L-2} and \mathbf{S}_3 is a $(L-1) \times (L-1)$ sub-matrix with off-diagonal elements c_1, \dots, c_{L-1} .

For a symmetric tridiagonal matrix, an efficient algorithm can be employed to calculate the determinant [149]. Let \mathbf{S} be a $N \times N$ symmetric tridiagonal matrix with diagonal elements d_1, d_2, \dots, d_N and off-diagonal elements s_1, s_2, \dots, s_{N-1} . Taking \mathbf{T}^j as the top left sub-matrix of \mathbf{S} with j rows and j columns and \mathbf{B}^j the bottom right sub-matrix of \mathbf{S} with $(N-j)$ rows and $(N-j)$ columns, we have

$$\det \mathbf{T}^{j+1} = d_{j+1} \det \mathbf{T}^j - s_j^2 \det \mathbf{T}^{j-1}, \quad (\text{A.6a})$$

$$\det \mathbf{B}^{j-1} = d_{j-1} \det \mathbf{B}^j - s_{j-1}^2 \det \mathbf{B}^{j+1}, \quad (\text{A.6b})$$

where $\mathbf{T}^0 = \mathbf{B}^{N+1} = \mathbf{I}$ and $\mathbf{S} = \mathbf{T}^N = \mathbf{B}^0$. Using this algorithm and Eq. (A.5), $\det \mathbf{G}$ can be calculate efficiently.

Finally, the cofactor $\text{cof}G_{j,j-1}$, which is essentially a determinant, can be calculated in the same way as $\det \mathbf{G}$. Using the algorithm above, the computation time of *pseudo* force can be reduced to 15% of the total simulation time.

Appendix B

Monte Carlo simulation of 1D particle-lattice model

The Monte Carlo simulation technique is widely used to study the particle-lattice model. In equilibrium, the standard simple Monte Carlo algorithm can be applied to sample the stationary measure. However, what we discuss here is the Kinetic Monte Carlo algorithm [175]. This algorithm allows us to go beyond equilibrium to the dynamics. We list the main steps of the algorithm as follows:

- Step 1: set the initial time $t = 0$ and choose an initial state of the system. The initial state can be N particle randomly distributed over L lattice sites or other specified configurations. For the convenience of later discussion, we denote the initial state as state k .

- Step 2: find all the possible hopping events and the corresponding hopping rates of the system, denoting the total number of hopping events as N_k and the transition rate to a new state i as r_{ki} . For example, if both sides of the j^{th} particle are empty sites, then two possible hopping events are that the particle hops either to right or to left. The corresponding hopping rates are α or β , respectively. Notice that, the reflecting boundaries are specified here in the simulation. Namely, if the first particle is already sitting on the first lattice site, then the hopping rate for it to the left is zero. Similar setting applies for the last particle.

- Step 3: order the possible hopping events in a list and calculate the cumulative hopping rate $R_{ki} = \sum_{j=1}^i r_{kj}$ for $i = 1, \dots, N_k$. The total hopping rate is $Q_k := R_{kN_k}$.

- Step 4: draw a uniform random number $u \in (0, 1]$, and find out the corresponding event i such that $R_{k,i-1} < uQ_k \leq R_{ki}$.

- Step 5: update the system from state k to state i .

- Step 6: update the system with $t = t + \Delta t$. Here, Δt is drawn from the Poisson distribution, which can be calculated as

$$\Delta t = \frac{1}{Q_k} \ln \left(\frac{1}{u'} \right), \quad (\text{B.1})$$

where u' is a new uniform random number different from u , also $u' \in (0, 1]$.

- Step 7: return to step 2 and do the iteration.

One has to wait for the system to reach equilibrium if the equilibrium statistics

are the main interests. Usually, the simulation runs quite fast. For a system of 1000 lattice sites and 500 particles, 10^6 update steps take less than 10 minutes.

Appendix C

The Toeplitz matrix

Toeplitz matrices are a special type of matrices that all elements along each diagonal parallel to the main diagonal are the same. Here, we focus on the tridiagonal Toeplitz matrix shown in Eq. (4.2).

To calculate the eigenvalues of matrix given by Eq. (4.2), we have to solve the equation

$$(\mathbf{A} - \lambda \mathbf{I})\mathbf{x} = \mathbf{0}. \quad (\text{C.1})$$

Then we can obtain a set of linear difference equations such that

$$x_{j-1} - (2 - \lambda)x_j + x_{j+1} = 0, \quad j = 1, \dots, L - 1. \quad (\text{C.2})$$

Here, $x_0 = x_L = 0$ is set for the boundaries. The characteristic equation for Eq. (C.2) is

$$r^2 - (2 - \lambda)r + 1 = 0. \quad (\text{C.3})$$

Denoting the two roots of Eq. (C.3) as r_1, r_2 , the solution of Eq. (C.2) can be written as

$$x_j = \begin{cases} \alpha r_1^j + \beta r_2^j & \text{if } r_1 \neq r_2, \\ \alpha \rho^j + \beta j \rho^j & \text{if } r_1 = r_2 = \rho, \end{cases} \quad (\text{C.4})$$

where α and β are arbitrary constants. The case of $r_1 = r_2$ can be eliminated because the resulting solution $x_0 = x_2 = \dots = x_L = 0$ is trivial. Hence we have $x_j = \alpha r_1^j + \beta r_2^j$. Plugging it into the boundary condition $x_0 = x_L = 0$ we obtain

$$\alpha + \beta = 0, \quad (\text{C.5a})$$

$$\alpha r_1^L + \beta r_2^L = 0. \quad (\text{C.5b})$$

From the above equations we can obtain $r_1 = r_2 \exp(i2\pi k/L)$ for $k = 1, 2, \dots, L - 1$. Meanwhile, we can obtain from the Eq. (C.3) that

$$r_1 r_2 = 1, \quad (\text{C.6a})$$

$$r_1 + r_2 = 2 - \lambda. \quad (\text{C.6b})$$

Therefore, we can solve $r_1 = \exp(i\pi k/L)$ and $r_2 = \exp(-i\pi k/L)$. The eigenvalues of

\mathbf{A} can be written as

$$\lambda_k = 4 \sin\left(\frac{k\pi}{2L}\right), \quad k = 1, 2, \dots, L-1. \quad (\text{C.7})$$

The corresponding normalized eigenvectors are

$$\mathbf{x}_k = \begin{pmatrix} \sqrt{\frac{2}{L}} \sin\left(\frac{k\pi}{L}\right) \\ \sqrt{\frac{2}{L}} \sin\left(\frac{2k\pi}{L}\right) \\ \sqrt{\frac{2}{L}} \sin\left(\frac{3k\pi}{L}\right) \\ \vdots \\ \sqrt{\frac{2}{L}} \sin\left(\frac{(L-1)k\pi}{L}\right) \end{pmatrix}. \quad (\text{C.8})$$

Appendix D

Derivation of the exclusion condition

To derive the exclusion condition, which might be confusing at the first sight, we use the example of two-particle system and then generalize it to the N particle case. Firstly, let us rewrite the master equation of the two particle system as:

$$\begin{aligned} \frac{dP(x_1, x_2; t)}{dt} = & \alpha P(x_1 - 1, x_2; t) + \beta P(x_1 + 1, x_2; t) \\ & + \alpha P(x_1, x_2 - 1; t) + \beta P(x_1, x_2 + 1; t) \\ & - 2(\alpha + \beta)P(x_1, x_2; t) \end{aligned} \quad (\text{D.1})$$

We assume that the above equation is valid for the whole space. However, this is actually not true when these two particles are sitting on the neighboring sites. Let us now consider this special case separately, remembering that $x_2 = x_1 + 1$. The master equation of this special case can be written as

$$\begin{aligned} \frac{dP(x_1, x_2; t)}{dt} = & \alpha P(x_1 - 1, x_2; t) + \beta P(x_1, x_2 + 1; t) \\ & - (\alpha + \beta)P(x_1, x_2; t) \end{aligned} \quad (\text{D.2})$$

Now, we can do a subtraction, i.e. (D.1) $-$ (D.2), obtain

$$\alpha P(x_1, x_2 - 1; t) + \beta P(x_1 + 1, x_2; t) = (\alpha + \beta)P(x_1, x_2; t) \quad (\text{D.3})$$

Denoting $x := x_1$ and plugging in $x_2 = x_1 + 1 = x + 1$ in the above equation, we finally arrive at

$$\alpha P(x, x; t) + \beta P(x + 1, x + 1; t) = (\alpha + \beta)P(x, x + 1; t) \quad (\text{D.4})$$

In summary, the sole master equation Eq. (D.1) does not contain the exclusion cases. In order to represent the exclusive setting, we assume Eq. (D.1) is valid for the whole space, and then apply an additional condition (Eq. (D.4)) on it. In the continuous space, the terms in Eq. D.4 is equivalent to the partial derivative of the probability density function at the collision boundary $x_1 = x_2$.

In a similar way, we can derive the exclusion condition for $N > 2$. Here we take the

example of $N = 3$ for illustration purpose. The master equation can be written as

$$\begin{aligned} \frac{dP(x_1, x_2, x_3; t)}{dt} = & \alpha P(x_1 - 1, x_2, x_3; t) + \beta P(x_1 + 1, x_2, x_3; t) \\ & + \alpha P(x_1, x_2 - 1, x_3; t) + \beta P(x_1, x_2 + 1, x_3; t) \\ & + \alpha P(x_1, x_2, x_3 - 1; t) + \beta P(x_1, x_2, x_3 + 1; t) \\ & - 3(\alpha + \beta)P(x_1, x_2, x_3; t). \end{aligned} \quad (\text{D.5})$$

The two body exclusion conditions can be derived exactly the same way as above. The results can be written as

$$\begin{aligned} \alpha P(x, x, x_3; t) + \beta P(x + 1, x + 1, x_3; t) &= (\alpha + \beta)P(x, x + 1, x_3; t), \\ \alpha P(x_1, x, x; t) + \beta P(x_1, x + 1, x + 1; t) &= (\alpha + \beta)P(x_1, x, x + 1; t). \end{aligned} \quad (\text{D.6})$$

Now, let us consider the three body collision, namely, when the three particles are sitting on three consecutive sites. The special master equation for this case can be written as

$$\begin{aligned} \frac{dP(x_1, x_2, x_3; t)}{dt} = & \alpha P(x_1 - 1, x_2, x_3; t) + \beta P(x_1, x_2, x_3 + 1; t) \\ & - (\alpha + \beta)P(x_1, x_2, x_3; t). \end{aligned} \quad (\text{D.7})$$

Subtracting Eq. (D.5) from Eq. (D.7) and taking $x_3 = x_2 + 1 = x_1 + 2 = x + 2$, we get

$$\begin{aligned} \alpha P(x, x + 1, x + 1; t) + \beta P(x, x + 2, x + 2; t) + \\ \alpha P(x, x, x + 2; t) + \beta P(x + 1, x + 1, x + 2; t) = 2(\alpha + \beta)P(x, x + 1, x + 2; t). \end{aligned} \quad (\text{D.8})$$

We immediately find that Eq. (D.8) can be recovered by adding up the two equations in Eq. (D.6). So it is not a new constraint. Actually, one can check in the same way that all the N body collision can be reduced to the summation of two body collisions for $N > 2$. Fundamentally, this is the feature guarantees that the ASEP system is integrable.

Appendix E

Bethe equations of the periodic ASEP

The ASEP model with periodic boundaries is the simplest model that was solved long ago [122, 138]. The master equation and exclusion condition of periodic ASEP are the same as the case of reflecting ASEP, shown in Eq. (4.63) and Eq. (4.65). The periodic boundary conditions can be written as

$$\Psi(x_1, x_2, \dots, x_{N-1}, x_N) = \Psi(x_2, x_3, \dots, x_N, x_1 + L). \quad (\text{E.1})$$

The Bethe ansatz of the periodic ASEP is constructed by the standard plane wave functions, which can be written as

$$\Psi(x_1, x_2, \dots, x_N) = \sum_{\sigma \in S_N} A_\sigma \prod_{n=1}^N \exp[ip_n x_{\sigma(n)}], \quad (\text{E.2})$$

where S_N is the group of N -permutation, and A_σ is the amplitude of the waves. p_n is the wave vectors and $x_{\sigma(n)}$ is the position of the $\sigma(n)^{\text{th}}$ particle.

By applying the exclusion condition Eq. (4.65) and the periodic boundary condition Eq. (E.1), one can derive the following set of Bethe equations

$$e^{ip_n L} = (-1)^{N-1} \prod_{m \neq n}^N \frac{a(p_n, p_m)}{a(p_m, p_n)}, \quad (\text{E.3})$$

where $a(p, p') = \sqrt{\alpha\beta} e^{i(p+p')} - (\alpha + \beta) e^{ip} + \sqrt{\alpha\beta}$.

By solving the Bethe equations, the wave vectors p_n can be obtained. Then the eigenvalues of the system can be calculated as

$$\Lambda = \sum_{n=1}^N \left[-(\alpha + \beta) + 2\sqrt{\alpha\beta} \cos(p_n) \right]. \quad (\text{E.4})$$

Appendix F

Single-file diffusion with reflecting boundaries

Single-file diffusion is the continuous limit of the discrete ASEP model. The connection from ASEP can be shown by transferring the hopping rate α , β to the diffusivity of particle D and drifting velocity μ :

$$D = \frac{1}{2}(\alpha + \beta), \quad (\text{F.1a})$$

$$\mu = \beta - \alpha. \quad (\text{F.1b})$$

The dynamical equation of the single-file particle system can be describe by the Fokker-Planck Equation

$$\begin{aligned} \frac{\partial p(\mathbf{x}, t|\mathbf{x}_0)}{\partial t} = & D \left(\frac{\partial^2}{\partial x_1^2} + \frac{\partial^2}{\partial x_2^2} + \cdots + \frac{\partial^2}{\partial x_N^2} \right) p(\mathbf{x}, t|\mathbf{x}_0), \\ & - \mu \left(\frac{\partial}{\partial x_1} + \frac{\partial}{\partial x_2} + \cdots + \frac{\partial}{\partial x_N} \right) p(\mathbf{x}, t|\mathbf{x}_0), \end{aligned} \quad (\text{F.2})$$

where $\mathbf{x} = (x_1, x_2, \cdots, x_N)^T$ is the vector that denotes the position of each particle and \mathbf{x}_0 is the initial position of particles. The reflecting boundaries of the ASEP system can be rewritten as

$$\left(D \frac{\partial}{\partial x_1} p(\mathbf{x}, t|\mathbf{x}_0) - \mu p(\mathbf{x}, t|\mathbf{x}_0) \right) \Big|_{x_1=0} = 0, \quad (\text{F.3a})$$

$$\left(D \frac{\partial}{\partial x_N} p(\mathbf{x}, t|\mathbf{x}_0) - \mu p(\mathbf{x}, t|\mathbf{x}_0) \right) \Big|_{x_N=L} = 0, \quad (\text{F.3b})$$

where $L = 2N$ in our case. Furthermore, we note that the exclusive condition which means the particle can not overtake each other can be formulated as

$$\left(\frac{\partial}{\partial x_{i+1}} p(\mathbf{x}, t|\mathbf{x}_0) - \frac{\partial}{\partial x_i} p(\mathbf{x}, t|\mathbf{x}_0) \right) \Big|_{x_i=x_{i+1}} = 0. \quad (\text{F.4})$$

Finally, the initial condition we assumed here is

$$p(\mathbf{x}, 0|\mathbf{x}_0) = \delta(x_1 - x_{1,0})\delta(x_2 - x_{2,0}) \cdots \delta(x_N - x_{N,0}). \quad (\text{F.5})$$

The solution of Eq. (F.2) together with Eq. (F.3),(F.4),(F.5) can be found by the continuous version of generalised coordinate Bethe Ansatz. We assume the solution of $p(\mathbf{x}, t|\mathbf{x}_0)$ can be written in the following form

$$p(\mathbf{x}, t|\mathbf{x}_0) = \sum_{\sigma \in S_N} \psi(x_1, x_{\sigma(1)}; t)\psi(x_2, x_{\sigma(2)}; t) \cdots \psi(x_N, x_{\sigma(N)}; t), \quad (\text{F.6})$$

where σ is a N -permutation of $x_{i,0}$. This means the expanded form of Eq. (F.6) reads

$$\begin{aligned} p(\mathbf{x}, t|\mathbf{x}_0) = & \psi(x_1, x_{1,0}; t)\psi(x_2, x_{2,0}; t) \cdots \psi(x_N, x_{N,0}; t) + \\ & \psi(x_1, x_{2,0}; t)\psi(x_2, x_{1,0}; t) \cdots \psi(x_N, x_{N,0}; t) + \\ & \text{all other permutations of } \{x_{1,0}, x_{2,0}, \cdots, x_{N,0}\}. \end{aligned} \quad (\text{F.7})$$

Now, it is important to find out the correct $\psi(x_i, x_{\sigma(i)}; t)$. We show here that $\psi(x_i, x_{\sigma(i)}; t)$ is simply the form of one single Brownian particle with a drifting velocity μ and diffusivity D in the reflecting box of size L , as indicated by the reflecting ASEP model. However, before diving into the derivation, let us explain the intuition why this method works. The reason might be rooting from the reflecting boundaries of the system. Because of the reflecting boundaries, the response of particles in the middle or in the periphery is exactly the same, i.e. reflecting. This leads to a factorized form of the N -particle PDF, i.e. Eq. (F.6). The conjecture is that Eq. (F.6) is the solution of the 1D N -particle system as long as the boundary is reflecting, even if the external force field is much more complex than the constant one. We give a proof next.

Here, we show that Eq. (F.6) is indeed the solution of the reflecting single file diffusion problem. It is actually quite simple and straightforward. We denote $\psi(x_i, x_{j,0}; t)$ as the solution of single particle in the box so that

$$\frac{\partial \psi(x_i, x_{j,0}; t)}{\partial t} = D \frac{\partial^2}{\partial x_i^2} \psi(x_i, x_{j,0}; t) - \mu \frac{\partial}{\partial x_i} \psi(x_i, x_{j,0}; t); \quad (\text{F.8a})$$

$$\left(D \frac{\partial}{\partial x_i} \psi(x_i, x_{j,0}; t) - \mu \psi(x_i, x_{j,0}; t) \right) \Big|_{x_i=0} = 0; \quad (\text{F.8b})$$

$$\left(D \frac{\partial}{\partial x_i} \psi(x_i, x_{j,0}; t) - \mu \psi(x_i, x_{j,0}; t) \right) \Big|_{x_i=L} = 0; \quad (\text{F.8c})$$

$$\psi(x_i, x_{j,0}; 0) = \delta(x_i - x_{j,0}). \quad (\text{F.8d})$$

Let us first check that Eq. (F.6) satisfies the Fokker-Planck equation. Substituting

Eq. (F.6) into Eq. (F.2) we obtain

$$\begin{aligned} \text{lhs} &= \sum_{\sigma \in S_N} \sum_{i=1}^N \frac{\partial \psi(x_i, x_{\sigma(i)}; t)}{\partial t} \prod_{j \neq i} \psi(x_j, x_{\sigma(j)}; t), \\ \text{rhs} &= \sum_{\sigma \in S_N} \sum_{i=1}^N \left(D \frac{\partial^2 \psi(x_i, x_{\sigma(i)}; t)}{\partial x_i^2} - \mu \frac{\partial \psi(x_i, x_{\sigma(i)}; t)}{\partial x_i} \right) \prod_{j \neq i} \psi(x_j, x_{\sigma(j)}; t). \end{aligned}$$

It is obvious that $\text{lhs} = \text{rhs}$ because of Eq. (F.8a). Other permutation terms of Eq. (F.6) can be proved in the same way.

Next, we show that the reflecting boundary conditions are satisfied. Plugging Eq. (F.6) into Eq. (F.3), we obtain

$$\begin{aligned} & \left(D \frac{\partial}{\partial x_1} p(\mathbf{x}, t | \mathbf{x}_0) - \mu p(\mathbf{x}, t | \mathbf{x}_0) \right) \Big|_{x_1=0} \\ &= \sum_{\sigma \in S_N} \left(D \frac{\partial \psi(x_1, x_{\sigma(1)}; t)}{\partial x_1} - \mu \psi(x_1, x_{\sigma(1)}; t) \right) \prod_{j \neq 1} \psi(x_j, x_{\sigma(j)}; t) \Big|_{x_1=0} = 0. \end{aligned}$$

Eq. (F.8b) is utilized in the last step. Similarly, the boundary condition at $x_N = L$ is also satisfied because of Eq. (F.8c).

We then show that the exclusive condition Eq. (F.4) is also fulfilled. We take a pair of permutation terms that we can always find in the ansatz of Eq. (F.6),

$$\begin{aligned} \phi &= \psi(x_i, x_{m,0}; t) \psi(x_{i+1}, x_{n,0}; t) \prod_{j \neq i, i+1} \psi(x_j, x_{\sigma(j)}; t) \\ &+ \psi(x_i, x_{n,0}; t) \psi(x_{i+1}, x_{m,0}; t) \prod_{j \neq i, i+1} \psi(x_j, x_{\sigma(j)}; t). \end{aligned}$$

It is easy to verify that

$$\begin{aligned} \left(\frac{\partial \phi}{\partial x_{i+1}} - \frac{\partial \phi}{\partial x_i} \right) \Big|_{x_i=x_{i+1}} &= \left(\frac{\partial \psi(x_{i+1}, x_{m,0}; t)}{\partial x_{i+1}} \psi(x_i, x_{n,0}; t) + \frac{\partial \psi(x_{i+1}, x_{n,0}; t)}{\partial x_{i+1}} \psi(x_i, x_{m,0}; t) \right. \\ &\quad \left. - \frac{\partial \psi(x_i, x_{m,0}; t)}{\partial x_i} \psi(x_{i+1}, x_{n,0}; t) - \frac{\partial \psi(x_i, x_{n,0}; t)}{\partial x_i} \psi(x_{i+1}, x_{m,0}; t) \right) \\ &\quad \times \prod_{j \neq i, i+1} \psi(x_j, x_{\sigma(j)}; t) \Big|_{x_i=x_{i+1}} \\ &= 0. \end{aligned}$$

Because $p(\mathbf{x}, t | \mathbf{x}_0)$ can be written as the summation of ϕ , the exclusive condition

Eq. (F.4) is proved.

Finally, we come to the initial condition. Simply plugging Eq. (F.8d) into the solution Eq. (F.6) we get

$$\begin{aligned} p(\mathbf{x}, 0|\mathbf{x}_0) = & \delta(x_1 - x_{1,0})\delta(x_2 - x_{2,0}) \cdots \delta(x_N - x_{N,0}) \\ & + \delta(x_1 - x_{2,0})\delta(x_2 - x_{1,0}) \cdots \delta(x_N - x_{N,0}) \\ & \text{all other permutations of } \{x_{1,0}, x_{2,0}, \cdots, x_{N,0}\}. \end{aligned}$$

All the other terms vanish except for the first in the above equation because by definition we have $x_1 < x_2 < \cdots < x_N$ and $x_{1,0} < x_{2,0} < \cdots < x_{N,0}$. We thus proved the initial condition Eq. (F.5). Finally, we have proved that Eq. (F.6) with Eq. (F.8) is the solution of our problem. Notice that this procedure of proof is still valid in the case where external force field is more complex than a constant field.

Now let us come back to the solution Eq. (F.6). The close form solution of our problem can be written down if we know the exact form of $\psi(x_i, x_{j,0}; t)$. Luckily, $\psi(x_i, x_{j,0}; t)$ is known from the work of Linetsky [176]. In our notation, $\psi(x_i, x_{j,0}; t)$ can be written as

$$\psi(x_i, x_{j,0}; t) = \psi_0(x_i) + \sum_{n=1}^{\infty} \exp(-\lambda_n t) \varphi_n(x_i, x_{j,0}), \quad (\text{F.9})$$

where $\psi_0(x_i)$ is stationary measure that does not depend on time and the initial condition. λ_n is the eigenvalue related to n^{th} relaxation mode, $\varphi_n(x_i, x_{j,0})$ is the function related to the initial condition. These functions are summarized as follows:

$$\psi_0(x_i) = \begin{cases} \frac{1}{L} & \text{for } \mu = 0, \\ \frac{\mu}{D} \frac{\exp(\frac{\mu x_i}{D})}{\exp(\frac{\mu L}{D}) - 1} & \text{for } \mu \neq 0. \end{cases} \quad (\text{F.10a})$$

$$\lambda_n = \frac{\mu^2}{4D} + \frac{Dn^2\pi^2}{L^2}; \quad (\text{F.10b})$$

$$\varphi_n(x_i, x_{j,0}) = \frac{D\pi^2 \exp(\frac{\mu}{2D}(x_i - x_{j,0}))}{2\lambda_n L} X_n(x_i) X_n(x_{j,0}); \quad (\text{F.10c})$$

$$X_n(x) = \frac{2n}{L} \cos\left(\frac{n\pi x}{L}\right) + \frac{\mu}{D\pi} \sin\left(\frac{n\pi x}{L}\right). \quad (\text{F.10d})$$

Plugging Eq. (F.9) and (F.10) into Eq. (F.6), we get the close form of N -particle solution. However, it is so lengthy and not clean enough for us to understand the physics. Here, we are mainly interested in the stationary state and the longest relaxation mode. So we keep only these two terms after the substitution to get

$$p(\mathbf{x}, t|\mathbf{x}_0) = p_0(\mathbf{x}) + p_1(\mathbf{x}, t|\mathbf{x}_0) + p_H(\mathbf{x}, t|\mathbf{x}_0). \quad (\text{F.11})$$

where p_H is the summation of all higher mode terms $n > 1$, p_0 and p_1 are stationary mode and longest relaxation mode, respectively, which can be written as

$$p_0(\mathbf{x}) = N! \psi_0(x_1) \prod_{i=1}^{N-1} \psi_0(x_{i+1}) \Theta(x_{i+1} - x_i); \quad (\text{F.12a})$$

$$p_1(\mathbf{x}, t | \mathbf{x}_0) = A_1(\mathbf{x}, \mathbf{x}_0) \exp(-\lambda_1 t); \quad (\text{F.12b})$$

$$A_1(\mathbf{x}, \mathbf{x}_0) = (N-1)! \sum_{i=1}^N \psi_0(x_i) \sum_{j \neq i}^N \sum_{k=1}^N \varphi_1(x_j, x_{k,0}). \quad (\text{F.12c})$$

Here, $\Theta(x)$ is the Heaviside step function and A_1 is the amplitude of the longest relaxation mode which only depends on the position of particles. We can see clearly from here that the second largest eigenvalue of the N -particle system is λ_1 , which is exactly the second largest eigenvalue of one particle system.

Appendix G

The blob theory of pinned polymer loop

We discuss here the blob theory of a pinned polymer loop. The polymer is supposed to be an ideal chain model, which means the typical size of the polymer R scales with the number of monomers L as $R \sim L^{1/2}$.

The blob theory claims that the pulled polymer is composed by a succession of independent blobs with the size of the blob

$$R_{blob} = \frac{k_B T}{f}, \quad (\text{G.1})$$

where f is the magnitude of the *local* pulling force, and R_{blob} is the typical size of the blob which can be measured by either the end to end distance or the gyration radius. We emphasize here that all constant pre-factors are ignored in this calculation. Then the number of monomers in one blob can be estimated as

$$L_{blob} = \left(\frac{k_B T}{f a} \right)^2, \quad (\text{G.2})$$

where a is size of one monomer. The total extension of the polymer chain along the force direction can be written as

$$z = \frac{L}{L_{blob}} R_{blob} = \frac{f a}{k_B T} L a. \quad (\text{G.3})$$

From the above equation, we obtain the local deformation of the polymer dz/dl , which can be written as

$$\frac{dz}{dl} = \frac{f a}{k_B T} a. \quad (\text{G.4})$$

Notice that for the pinned chain in an external force field, the local force f is accumulated by the tension from the non-pinned end. Namely, we have $f \sim Fz/a$, where

F is the strength of the external force field. Thus we arrive at

$$z(l) = a \left(\frac{k_B T}{F a} \right)^{\frac{1}{2}} \exp \left(\frac{F a}{k_B T} l \right) = a \tilde{T}^{\frac{1}{2}} \exp \left(\frac{l}{\tilde{T}} \right). \quad (\text{G.5})$$

We purposefully write it in this form which makes the comparison to our theory easier.

Now we discuss the different regimes of the steady state. The first regime is the unperturbed regime. In this regime, the external force field is weak, and the configuration of the polymer is nearly coiled. The boundary of this regime can be estimated by

$$k_B T = f R_0 = \frac{R_0}{a} F R_0 = F L a. \quad (\text{G.6})$$

From Eq. (G.6), we can obtain the critical dimensionless temperature $\tilde{T}_{c1} = L$.

The second regime is characterized by a series of blobs with increasing size, which is called the trumpet regime. The smallest blob is the one right next to the pinned point. Consequently, the smallest possible size of a blob is a . We have

$$k_B T = f a = F L_z, \quad (\text{G.7})$$

where $L_z = z(L)$ can be calculated by Eq. (G.5). By solving the above equation, we can obtain the boundary of the trumpet regime as $\sqrt{\tilde{T}} = \exp \frac{L}{\tilde{T}}$. Thus we have $\tilde{T}_{c2} = \frac{2L}{\text{LambertW}(2L)}$. Here $\text{LambertW}(x)$ is a special function that denotes the inverse function of $f(x) = x \exp(x)$. In the case of $L \in [100, 1000]$, we have $\tilde{T}_{c2} \approx L/3$.

The next regime is called the stem-flower regime, where the part of polymer near to the pinned point is almost stretched while the part far from the pinned point is still composed by blobs. Denoting the extension of the ‘‘flower’’ part as z_f and number of monomers in the ‘‘flower’’ as l_f , we have

$$k_B T = f a = F z_f. \quad (\text{G.8})$$

Again, we can calculate z_f by Eq. (G.5). Thus we have

$$z_f = \frac{\tilde{T}}{\tilde{T}_{c2}} L_z = \sqrt{\tilde{T}} \exp \left(\frac{l_f}{\tilde{T}} \right) a; \quad (\text{G.9a})$$

$$l_f = \tilde{T} \left(\frac{L}{\tilde{T}_{c2}} + \frac{1}{2} \ln \tilde{T} - \frac{1}{2} \ln \tilde{T}_{c2} \right). \quad (\text{G.9b})$$

By further increasing the external force field, we can finally arrive at the fully stretched regime where the whole polymer is stretched. The critical \tilde{T}_{c3} can be calculated from Eq. (G.9) by setting $l_f = 1$. Interestingly, we can obtain $\tilde{T}_{c3} = \frac{2}{\text{LambertW}(2)} \approx 2.35$ which is independent of the system size.

Finally, let us discuss the impact of the looping structure. In the ideal chain model,

there is no excluded volume effect. The pinned polymer loop is the same as the pinned polymer chain except for that a factor of $1/2$ has to be multiplied to L . In the scaling discussion above, this pre-factor is negligible.

Bibliography

- [1] G. Lawler and V. Limic. *Random Walk: A Modern Introduction*. Cambridge University Press, 2010.
- [2] S. Redner. *A Guide to First-Passage Processes*. Cambridge University Press, 2001.
- [3] C. T. MacDonald, J. H. Gibbs, and A. C. Pipkin. Kinetics of biopolymerization. *Biopolymers*, 6:1–25, 1968.
- [4] P. C. Bressloff and J. M. Newby. Stochastic models of intracellular transport. *Rev. Mod. Phys.*, 85:135–196, 2013.
- [5] T. Chou, K. Mallick, and R. K. P. Zia. Non-equilibrium statistical mechanics: from a paradigmatic model to biological transport. *Rep. Prog. Phys.*, 74:116601, 2011.
- [6] P. Bovet and S. Benhamou. Spatial analysis of animals' movements using a correlated random walk model. *J. Theor. Biol.*, 131:419–433, 1988.
- [7] F. Bartumeus, M. G. E. da Luz, G. M. Viswanathan, and J. Catalan. Animal search strategies: a quantitative random-walk analysis. *Ecology*, 86:3078–3087, 2005.
- [8] M. A. Lewis, P. K. Maini, and S. V. Petrovskii. *Dispersal, Individual Movement and Spatial Ecology: A Mathematical Perspective*. Lecture Notes in Mathematics. Springer Berlin Heidelberg, 2013.
- [9] D. Patterson. Molecular genetic analysis of Down syndrome. *Hum. Genet.*, 126:195–214, 2009.
- [10] R. Koszul and N. Kleckner. Dynamic chromosome movements during meiosis: a way to eliminate unwanted connections? *Trends Cell Biol.*, 19:716–724, 2009.
- [11] M. R. Chacón, P. Delivani, and I. M. Tolić. Meiotic nuclear oscillations are necessary to avoid excessive chromosome associations. *Cell Rep.*, 17:1632–1645, 2016.
- [12] D. Ding, A. Yamamoto, T. Haraguchi, and Y. Hiraoka. Dynamics of homologous chromosome pairing during meiotic prophase in fission yeast. *Dev. Cell*, 6:329–341, 2004.

- [13] Y. Chikashige, D. Ding, H. Funabiki, T. Haraguchi, S. Mashiko, M. Yanagida, and Y. Hiraoka. Telomere-led premeiotic chromosome movement in fission yeast. *Science*, 264:270–273, 1994.
- [14] S. K. Vogel, N. Pavin, N. Maghelli, F. Jülicher, and I. M. Tolić-Nørrelykke. Self-organization of dynein motors generates meiotic nuclear oscillations. *PLoS Biol.*, 7:e1000087, 2009.
- [15] H. Shibuya, A. Morimoto, and Y. Watanabe. The dissection of meiotic chromosome movement in mice using an in vivo electroporation technique. *PLoS Genet.*, 10:e1004821, 2014.
- [16] A. Yamamoto, C. Tsutsumi, H. Kojima, K. Oiwa, and Y. Hiraoka. Dynamic behavior of microtubules during dynein-dependent nuclear migrations of meiotic prophase in fission yeast. *Mol. Biol. Cell*, 12:3933–3946, 2001.
- [17] J. L. Gerton and R. S. Hawley. Homologous chromosome interactions in meiosis: diversity amidst conservation. *Nat. Rev. Genet.*, 6:477–487, 2005.
- [18] P. de Gennes. *Scaling concepts in polymer physics*. Cornell University Press, 1979.
- [19] M. Doi and S. F. Edwards. *The theory of polymer dynamics*. Oxford University Press, 1988.
- [20] Y. Lin, D. Frömberg, W. Huang, P. Delivani, M. Chacón, I. M. Tolić, F. Jülicher, and V. Zaburdaev. Pulled polymer loops as a model for the alignment of meiotic chromosomes. *Phys. Rev. Lett.*, 115:208102, 2015.
- [21] S. L. Forsburg. Overview of *Schizosaccharomyces pombe*. *Curr. Protoc. Mol. Biol.*, 13:13–14, 2003.
- [22] P. A. Fantes and C. S. Hoffman. A brief history of *Schizosaccharomyces pombe* research: a perspective over the past 70 years. *Genetics*, 203:621–629, 2016.
- [23] D. O. Morgan. *The cell cycle: principles of control*. Primers in Biology. OUP/New Science Press, 2007.
- [24] C. S. Hoffman, V. Wood, and P. A. Fantes. An ancient yeast for young geneticists: a primer on the *Schizosaccharomyces pombe* model system. *Genetics*, 201:403–423, 2015.
- [25] V. Wood, R. Gwilliam, M.-A. Rajandream, et al. The genome sequence of *Schizosaccharomyces pombe*. *Nature*, 415:871–880, 2002.
- [26] M. Coelho, A. Dereli, A. Haese, S. Kühn, L. Malinowska, M. E. DeSantis, J. Shorter, S. Alberti, T. Gross, and I. M. Tolić-Nørrelykke. Fission yeast does not age under favorable conditions, but does so after stress. *Curr. Biol.*, 23:1844–1852, 2013.

- [27] S. Freeman. *Biological Science*. Pearson/Benjamin Cummings, 2008.
- [28] M. Villeneuve and K. J. Hillers. Whence meiosis? *Cell*, 106:647–650, 2001.
- [29] "Meiosis." *Wikipedia: The Free Encyclopedia*. Wikimedia Foundation, Inc. 22 July 2004. Web. 1 Apr. 2017.
- [30] D. M. Richards, E. Greer, A. C. Martin, G. Moore, P. J. Shaw, and M. Howard. Quantitative Dynamics of Telomere Bouquet Formation. *PLoS Comput. Biol.*, 8:e1002812, 2012.
- [31] L. Davis and G. R. Smith. Meiotic recombination and chromosome segregation in *Schizosaccharomyces pombe*. *Proc. Natl. Acad. Sci.*, 98:8395–8402, 2001.
- [32] O. Niwa, M. Shimanuki, and F. Miki. Telomere-led bouquet formation facilitates homologous chromosome pairing and restricts ectopic interaction in fission yeast meiosis. *EMBO J.*, 19:3831–3840, 2000.
- [33] D. Ding, Y. Chikashige, T. Haraguchi, and Y. Hiraoka. Oscillatory nuclear movement in fission yeast meiotic prophase is driven by astral microtubules, as revealed by continuous observation of chromosomes and microtubules in living cells. *J. Cell Sci.*, 111:701–712, 1998.
- [34] J. L. Wells, D. W. Pryce, and R. J. McFarlane. Homologous chromosome pairing in *Schizosaccharomyces pombe*. *Yeast*, 23:977–989, 2006.
- [35] H. Asakawa, T. Haraguchi, and Y. Hiraoka. Reconstruction of the kinetochore: a prelude to meiosis. *Cell Div.*, 2:17, 2007.
- [36] R. Egel. *The Molecular Biology of Schizosaccharomyces pombe: Genetics, Genomics and Beyond*. Springer, 2004.
- [37] D. Ding, N. Sakurai, Y. Katou, T. Itoh, K. Shirahige, T. Haraguchi, and Y. Hiraoka. Meiotic cohesins modulate chromosome compaction during meiotic prophase in fission yeast. *J. Cell Biol.*, 174:499–508, 2006.
- [38] J. Langowski. Polymer chain models of DNA and chromatin. *Eur. Phys. J. E*, 19:241–249, 2006.
- [39] W. F. Marshall, J. F. Marko, D. A. Agard, and J. W. Sedat. Chromosome elasticity and mitotic polar ejection force measured in living *Drosophila* embryos by four-dimensional microscopy-based motion analysis. *Curr. Biol.*, 11:569–578, 2001.
- [40] I. Kalinina, A. Nandi, P. Delivani, M. R. Chacón, A. H. Klemm, D. R. Johnson, A. Krull, B. Lindner, N. Pavin, and I. M. Tolić-Nørrelykke. Pivoting of microtubules around the spindle pole accelerates kinetochore capture. *Nat. Cell Biol.*, 15:82–87, 2012.

- [41] H. Wong, J. Arbona, and C. Zimmer. How to build a yeast nucleus. *Nucleus*, 4:361–366, 2013.
- [42] D. R. Tree, A. Muralidhar, P. S. Doyle, and K. D. Dorfman. Is dna a good model polymer. *Macromolecules*, 46:8369–8382, 2013.
- [43] J. D. Halverson, J. Smrek, K. Kremer, and A. Y. Grosberg. From a melt of rings to chromosome territories: the role of topological constraints in genome folding. *Rep. Prog. Phys.*, 77:022601, 2014.
- [44] S. Jun and A. Wright. Entropy as the driver of chromosome segregation. *Nat. Rev. Microbiol.*, 8:600–607, 2010.
- [45] P. G. De Gennes. Coil-stretch transition of dilute flexible polymers under ultra-high velocity gradients. *J. Chem. Phys.*, 60:5030–5042, 1974.
- [46] D. Richter, S. Gooßen, and A. Wischnewski. Celebrating soft matter’s 10th anniversary: topology matters: structure and dynamics of ring polymers. *Soft Matter*, 11:8535–8549, 2015.
- [47] H. A. Kramers. The behavior of macromolecules in inhomogeneous flow. *J. Chem. Phys.*, 14:415–424, 1946.
- [48] B. H. Zimm and W. H. Stockmayer. The dimensions of chain molecules containing branches and rings. *J. Chem. Phys.*, 17:1301–1314, 1949.
- [49] E. F. Casassa. Some statistical properties of flexible ring polymers. *J. Polym. Sci. Part A*, 3:605–614, 1965.
- [50] W. Burchard and M. Schmidt. Static and dynamic structure factors calculated for flexible ring macromolecules. *Polymer*, 21:745–749, 1980.
- [51] A. Baumgörtner. Statistics of self-avoiding ring polymers. *J. Chem. Phys.*, 76:4275, 1982.
- [52] M. E. Cates and J. M. Deutsch. Conjectures on the statistics of ring polymers. *J. Phys.*, 47:2121–2128, 1986.
- [53] S. P. Obukhov, M. Rubinstein, and T. Duke. Dynamics of a ring polymer in a gel. *Phys. Rev. Lett.*, 73:1263–1266, 1994.
- [54] Wilfried Carl. Configurational and rheological properties of cyclic polymers. *J. Chem. Soc. Faraday Trans.*, 91:2525–2530, 1995.
- [55] W. Carl. Some aspects of theory and simulations of polymers in steady flows. *Macromol. Theory Simul.*, 5:1–27, 1996.
- [56] S. Panyukov and Y. Rabin. Fluctuating elastic rings: Statics and dynamics. *Phys. Rev. E*, 64:011909, 2001.

- [57] D. Mukherji, G. Bartels, and M. H. Müser. Scaling laws of single polymer dynamics near attractive surfaces. *Phys. Rev. Lett.*, 100:1–4, 2008.
- [58] T. Sakaue. Ring polymers in melts and solutions: scaling and crossover. *Phys. Rev. Lett.*, 106:1–4, 2011.
- [59] T. Sakaue. Statistics and geometrical picture of ring polymer melts and solutions. *Phys. Rev. E*, 85:021806, feb 2012.
- [60] J. Kim, Y. Yang, and W. Lee. Self-consistent field theory of gaussian ring polymers. *Macromolecules*, 45:3263–3269, 2012.
- [61] S. Y. Reigh and D. Y. Yoon. Concentration dependence of ring polymer conformations from monte carlo simulations. *ACS Macro Lett.*, 2:296–300, 2013.
- [62] P. S. Lang, B. Obermayer, and E. Frey. Dynamics of a semiflexible polymer or polymer ring in shear flow. *Phys. Rev. E*, 89:022606, 2014.
- [63] A. Rosa and R. Everaers. Structure and dynamics of interphase chromosomes. *PLoS Comput. Biol.*, 4:e1000153, 2008.
- [64] A. Rosa and R. Everaers. Ring polymers in the melt state: the physics of crumpling. *Phys. Rev. Lett.*, 112:118302, 2014.
- [65] J. Dorier and A. Stasiak. Topological origins of chromosomal territories. *Nucleic Acids Res.*, 37:6316–6322, 2009.
- [66] R. K. Sachs, G. Engh, B. Trask, H. Yokota, and J. E. Hearst. A random-walk/giant-loop model for interphase chromosomes. *Proc. Natl. Acad. Sci.*, 92:2710–2714, 1995.
- [67] J. F. Marko. Linking topology of tethered polymer rings with applications to chromosome segregation and estimation of the knotting length. *Phys. Rev. E*, 79:051905, 2009.
- [68] A. Rosa, N. B. Becker, and R. Everaers. Looping probabilities in model interphase chromosomes. *Biophys. J.*, 98:2410–2419, 2010.
- [69] Y. Zhang and D. W. Heermann. Loops determine the mechanical properties of mitotic chromosomes. *PLoS One*, 6:e29225, 2011.
- [70] H. Wong, H. Marie-Nelly, S. Herbert, P. Carrivain, H. Blanc, R. Koszul, E. Fabre, and C. Zimmer. A predictive computational model of the dynamic 3d interphase yeast nucleus. *Curr. Biol.*, 22:1881–1890, 2012.
- [71] J. Dekker, M. Marti-Renom, and L. Mirny. Exploring the three-dimensional organization of genomes: interpreting chromatin interaction data. *Nat. Rev. Genet.*, 14:390–403, 2013.

- [72] L. Giorgetti, R. Galupa, E. Nora, T. Piolot, F. Lam, J. Dekker, G. Tiana, and E. Heard. Predictive polymer modeling reveals coupled fluctuations in chromosome conformation and transcription. *Cell*, 157:950–63, 2014.
- [73] B. Youngren, H. Nielsen, S. Jun, and S. Austin. The multifork *Escherichia coli* chromosome is a self-duplicating and self-segregating thermodynamic ring polymer. *Genes Dev.*, 28:71–84, 2014.
- [74] M. Fritsche and D. W. Heermann. Confinement driven spatial organization of semiflexible ring polymers: Implications for biopolymer packaging. *Soft Matter*, 7:6906, 2011.
- [75] B. Ha and Y. Jung. Polymers under confinement: single polymers, how they interact, and as model chromosomes. *Soft Matter*, 11:2333–2352, 2015.
- [76] S. F. Tead, E. J. Kramer, G. Hadziioannou, M. Antonietti, H. Sillescu, P. Lutz, and C. Strazielle. Polymer topology and diffusion: a comparison of diffusion in linear and cyclic macromolecules. *Macromolecules*, 25:3942–3947, 1992.
- [77] M. Kapnistos, M. Lang, D. Vlassopoulos, W. Pyckhout-Hintzen, D. Richter, D. Cho, T. Chang, and M. Rubinstein. Unexpected power-law stress relaxation of entangled ring polymers. *Nat. Mater.*, 7:997–1002, 2008.
- [78] A. Brás et al. Structure and dynamics of polymer rings by neutron scattering: breakdown of the Rouse model. *Soft Matter*, 7:11169, 2011.
- [79] G. Witz, K. Rechendorff, J. Adamcik, and G. Dietler. Conformation of circular DNA in two dimensions. *Phys. Rev. Lett.*, 101:3–6, 2008.
- [80] G. Witz, K. Rechendorff, J. Adamcik, and G. Dietler. Conformation of ring polymers in 2D constrained environments. *Phys. Rev. Lett.*, 106:2–5, 2011.
- [81] S. Gooßen, A. Brás, M. Krutyeva, M. Sharp, P. Falus, A. Feoktystov, U. Gasser, W. Pyckhout-Hintzen, A. Wischniewski, and D. Richter. Molecular scale dynamics of large ring polymers. *Phys. Rev. Lett.*, 113:168302, 2014.
- [82] S. Gooßen, M. Krutyeva, M. Sharp, A. Feoktystov, J. Allgaier, W. Pyckhout-Hintzen, A. Wischniewski, and D. Richter. Sensing polymer chain dynamics through ring topology: a neutron spin echo study. *Phys. Rev. Lett.*, 115:148302, 2015.
- [83] M. Bishop and J. Michels. The shape of ring polymers. *J. Chem. Phys.*, 82:1059–1061, 1985.
- [84] O. Jagodzinski, E. Eisenriegler, and K. Kremer. Universal shape properties of open and closed polymer chains: renormalization group analysis and Monte Carlo experiments. *J. Phys. I Fr.*, 2:2243–2279, 1992.
- [85] K. Alim and E. Frey. Shapes of semiflexible polymer rings. *Phys. Rev. Lett.*, 99:1–4, 2007.

-
- [86] P. Reiss, M. Fritsche, and D. W. Heermann. Looped star polymers show conformational transition from spherical to flat toroidal shapes. *Phys. Rev. E*, 84:051910, 2011.
- [87] J. Michels and F. Wiegel. Probability of knots in a polymer ring. *Phys. Lett. A*, 90:381–384, 1982.
- [88] K. Koniaris and M. Muthukumar. Knottedness in ring polymers. *Phys. Rev. Lett.*, 66:2211–2214, 1991.
- [89] K. Koniaris and M. Muthukumar. Self-entanglement in ring polymers. *J. Chem. Phys.*, 95:2873, 1991.
- [90] A. Grosberg, A. Feigel, and Y. Rabin. Flory-type theory of a knotted ring polymer. *Phys. Rev. E*, 54:6618–6622, 1996.
- [91] M. K. Shimamura and T. Deguchi. Gyration radius of a circular polymer under a topological constraint with excluded volume. *Phys. Rev. E*, 64:020801, 2001.
- [92] E. Orlandini, A. L. Stella, and C. Vanderzande. Polymer θ -point as a knot delocalization transition. *Phys. Rev. E*, 68:031804, sep 2003.
- [93] L. Tubiana, E. Orlandini, and C. Micheletti. Multiscale entanglement in ring polymers under spherical confinement. *Phys. Rev. Lett.*, 107:1–4, 2011.
- [94] E. Uehara and T. Deguchi. Statistical and hydrodynamic properties of double-ring polymers with a fixed linking number between twin rings. *J. Chem. Phys.*, 140, 2014.
- [95] B. Li, Z. Sun, and L. An. Effects of topology on the adsorption of singly tethered ring polymers to attractive surfaces. *J. Chem. Phys.*, 143:024908, 2015.
- [96] P. Pincus. Excluded volume effects and stretched polymer chains. *Macromolecules*, 9:386–388, 1976.
- [97] P. Pincus. Dynamics of stretched polymer chains. *Macromolecules*, 10:210–213, 1977.
- [98] F. Brochard-Wyart. Deformations of one tethered chain in strong flows. *Europhys. Lett.*, 23:105–111, 1993.
- [99] F. Brochard-Wyart, H. Hervet, and P. Pincus. Unwinding of polymer chains under forces or flows. *Europhys. Lett.*, 26:511–516, 1994.
- [100] F. Brochard-Wyart. Polymer chains under strong flows: stems and flowers. *Europhys. Lett.*, 30:387–392, 1995.
- [101] A. Adjarej, F. Brochard-Wyart, and P. G. de Gennes. Drag on a tethered chain in a polymer melt. *J. Phys. II Fr.*, 5:491, 1995.

-
- [102] T. Perkins, D. Smith, R. Larson, and S. Chu. Stretching of a single tethered polymer in a uniform flow. *Science*, 268:83–87, 1995.
- [103] T. Perkins, D. Smith, and S. Chu. Direct observation of tube-like motion of a single polymer chain. *Science*, 264:819–822, 1994.
- [104] T. Perkins, Quake, D. Smith, and S. Chu. Relaxation of a single DNA molecule observed by optical microscopy. *Science*, 264:822–826, 1994.
- [105] D. Wirtz. Direct measurement of the transport-properties of a single DNA molecule. *Phys. Rev. Lett.*, 75:2436–2439, 1995.
- [106] R. Rzehak, D. Kienle, T. Kawakatsu, and W. Zimmermann. Partial draining of a tethered polymer in flow. *Europhys. Lett.*, 46:821–826, 1999.
- [107] R. G. Larson, H. Hu, D. E. Smith, and S. Chu. Brownian dynamics simulations of a DNA molecule in an extensional flow field. *J. Rheol.*, 43:267, 1999.
- [108] P. S. Doyle, B. Ladoux, and J. L. Viovy. Dynamics of a tethered polymer in shear flow. *Phys. Rev. Lett.*, 84:4769–4772, 2000.
- [109] B. Ladoux and P. S. Doyle. Stretching tethered DNA chains in shear flow. *Europhys. Lett.*, 52:511–517, 2000.
- [110] K. L. Sebastian. Pulling a polymer out of a potential well and the mechanical unzipping of DNA. *Phys. Rev. E*, 62:1128–1132, 2000.
- [111] Y. Cui and C. Bustamante. Pulling a single chromatin fiber reveals the forces that maintain its higher-order structure. *Proc. Natl. Acad. Sci.*, 97:127–132, 2000.
- [112] R. Rzehak. Conformational fluctuations of a tethered polymer in uniform flow. *Eur. Phys. J. E*, 11:335–348, 2003.
- [113] A. Mohan and P. S. Doyle. Unraveling of a tethered polymer chain in uniform solvent flow. *Macromolecules*, 40:4301–4312, 2007.
- [114] C. E. Sing and A. Alexander-Katz. Theory of tethered polymers in shear flow: The strong stretching limit. *Macromolecules*, 44:9020–9028, 2011.
- [115] T. Sakaue, T. Saito, and H. Wada. Dragging a polymer in a viscous fluid: Steady state and transient. *Phys. Rev. E*, 86:011804, 2012.
- [116] A. Varghese, S. Vemparala, and R. Rajesh. Force fluctuations in stretching a tethered polymer. *Phys. Rev. E*, 88:022134, 2013.
- [117] L. Dai and P. S. Doyle. Comparisons of a polymer in confinement versus applied force. *Macromolecules*, 46:6336–6344, 2013.
- [118] C. Bechinger et al. Active Particles in Complex and Crowded Environments. *Rev. Mod. Phys.*, 88:045006, 2016.

-
- [119] K. Huang *Statistical Mechanics*. John Wiley & Sons, 1987.
- [120] D. Chandler, *Introduction to Modern Statistical Mechanics* Oxford University Press, 1987.
- [121] B. Derrida. An exactly soluble non-equilibrium system: The asymmetric simple exclusion process. *Phys. Rep.*, 301:65–83, 1998.
- [122] K. Mallick. Some exact results for the exclusion process. *J. Stat. Mech. Theor. Exp.*, 2011:P01024, 2011.
- [123] F. Spitzer. Interaction of Markov processes. *Adv. Math.*, 5:246–290, 1970.
- [124] E. P. Hsu and S. R. S. Varadhan. *Probability Theory and Applications*. IAS/Park City mathematics series. American Mathematical Soc., 1999.
- [125] A. Schadschneider, D. Chowdhury, and K. Nishinari. *Stochastic Transport in Complex Systems: From Molecules to Vehicles*. Elsevier Science, 2010.
- [126] M. T. Batchelor. The Bethe ansatz after 75 years. *Phys. Today*, 60:36–40, 2007.
- [127] D. G. Levitt. Dynamics of a Single-File Pore: Non-Fickian Behavior. *Phys. Rev. A*, 8:3050–3054, 1973.
- [128] E. Barkai and R. Silbey. Theory of single file diffusion in a force field. *Phys. Rev. Lett.*, 102:050602, 2009.
- [129] V. Kukla et al. NMR studies of single-file diffusion in unidimensional channel zeolites *Science*, 272:5262, 1996.
- [130] Q. Wei, C. Bechinger and P. Leiderer. Single-file diffusion of colloids in one-dimensional channels *Science*, 287:5453, 2000.
- [131] C. Lutz, M. Kollmann and C. Bechinger. Single-file diffusion of colloids in one-dimensional channels *Phys. Rev. Lett.*, 93:026001, 2004.
- [132] A. Das et al. Single-file diffusion of confined water inside SWNTs: an NMR study *ACS Nano*, 4:1687–1695, 2010.
- [133] N. Crampe, E. Ragoucy, and M. Vanicat. Integrable approach to simple exclusion processes with boundaries. *J. Stat. Mech. Theory Exp.*, 2014:P11032, 2014.
- [134] J. Krug. Boundary-induced phase transitions in driven diffusive systems. *Phys. Rev. Lett.*, 67:1882–1885, 1991.
- [135] J. de Gier and F. H. L. Essler. Bethe ansatz solution of the asymmetric exclusion process with open boundaries. *Phys. Rev. Lett.*, 95:240601, 2005.
- [136] T. Sasamoto and H. Spohn. One-dimensional kardar-parisi-zhang equation: an exact solution and its universality. *Phys. Rev. Lett.*, 104:230602, 2010.

-
- [137] S. Sandow and G. Schütz. On $U_q[SU(2)]$ -symmetric driven diffusion. *Europhys. Lett.*, 26:7–12, 1994.
- [138] H. Bethe. Zur Theorie der Metalle. *Zeitschrift für Phys.*, 71:205–226, 1931.
- [139] E. H. Lieb. Exact analysis of an interacting bose gas. ii. the excitation spectrum. *Phys. Rev.*, 130:1616–1624, 1963.
- [140] E. H. Lieb and W. Liniger. Exact analysis of an interacting bose gas. i. the general solution and the ground state. *Phys. Rev.*, 130:1605–1616, 1963.
- [141] E. H. Lieb. Exact solution of the problem of the entropy of two-dimensional ice. *Phys. Rev. Lett.*, 18:692–694, 1967.
- [142] E. H. Lieb. Exact solution of the problem of the F model of an antifer-roelectric. *Phys. Rev. Lett.*, 18:1046–1048, 1967.
- [143] E. H. Lieb. Exact solution of the two-dimensional Slater KDP model of a ferroelectric. *Phys. Rev. Lett.*, 19:108–110, 1967.
- [144] C. N. Yang. Some exact results for the many-body problem in one dimension with repulsive delta-function interaction. *Phys. Rev. Lett.*, 19:1312–1315, 1967.
- [145] R. J. Baxter. Partition function of the Eight-Vertex lattice model. *Ann. Phys.*, 70:193–228, 1972.
- [146] T. M. Liggett. *Stochastic interacting systems: contact, voter and exclusion processes*, Springer, 1999.
- [147] G. Schütz. Exactly solvable models for many-body systems far from equilibrium. *Phase transitions and critical phenomena vol. 19*, Academic Press, 2001.
- [148] O. Golinelli and K. Mallick. The asymmetric simple exclusion process: an integrable model for non-equilibrium statistical mechanics. *J. Phys. A. Math. Gen.*, 39:12679–12705, 2006.
- [149] M. Pasquali and D. C. Morse. An efficient algorithm for metric correction forces in simulations of linear polymers with constrained bond lengths. *J. Chem. Phys.*, 116:1834, 2002.
- [150] M. Somasi, B. Khomami, N. J. Woo, J. S. Hur, and E. Shaqfeh. Brownian dynamics simulations of bead-rod and bead-spring chains: numerical algorithms and coarse-graining issues. *J. Nonnewton. Fluid Mech.*, 108:227–255, 2002.
- [151] C. Cruz, F. Chinesta, and G. Régnier. Review on the brownian dynamics simulation of bead-rod-spring models encountered in computational rheology. *Arch. Comput. Methods Eng.*, 19:227–259, 2012.
- [152] N. G. van Kampen. Statistical mechanics of trimers. *Appl. Sci. Res.*, 37:67–75, 1981.

- [153] N. G. van Kampen. Constraints. *Am. J. Phys.*, 52:419, 1984.
- [154] M. Fixman. Classical statistical mechanics of constraints: a theorem and application to polymers. *Proc. Natl. Acad. Sci.*, 71:3050–3053, 1974.
- [155] T. W. Liu. Flexible polymer chain dynamics and rheological properties in steady flows. *J. Chem. Phys.*, 90:5826, 1989.
- [156] R. L. Honeycutt. Stochastic Runge-Kutta algorithms. I. White noise. *Phys. Rev. A*, 45:600–603, 1992.
- [157] K. Binder. *Monte Carlo and Molecular Dynamics simulations in polymers science*. Oxford University Press, 1995.
- [158] D. Meimaroglou and C. Kiparissides. Review of Monte Carlo methods for the prediction of distributed molecular and morphological polymer properties. *Ind. Eng. Chem. Res.*, 53:8963–8979, 2013.
- [159] H. P. Hsu and P. Grassberger. A Review of Monte Carlo Simulations of Polymers with PERM. *J. Stat. Phys.*, 144:597–637, 2011.
- [160] W. Feller. *An introduction to probability theory and its applications*. Wiley India Pvt. Limited, 2 edition, 2008.
- [161] K. B. Athreya and S. N. Lahiri. *Measure Theory and Probability Theory*. Springer, 2006.
- [162] G. E. Andrews. *The Theory of Partitions*. Cambridge University Press, 1998.
- [163] J. Tsai and B. D. McKee. Homologous pairing and the role of pairing centers in meiosis. *J. Cell Sci.*, 124:1955–1963, 2011.
- [164] V. Blavatska and W. Janke. Shape anisotropy of polymers in disordered environment. *J. Chem. Phys.*, 133:1–7, 2010.
- [165] S. Katz, J. L. Lebowitz, and H. Spohn. Phase transitions in stationary nonequilibrium states of model lattice systems. *Phys. Rev. B*, 28, 1655, 1983.
- [166] C. D. Meyer. *Matrix analysis and applied linear algebra*. Society for industrial and applied mathematics, 2000.
- [167] S. Toba, T. M. Watanabe, L. Y. Okimoto, Y. Toyoshima, and H. Higuchi. Overlapping hand-over-hand mechanism of single molecular motility of cytoplasmic dynein. *Proc. Natl. Acad. Sci.*, 103:5741–5745, 2006.
- [168] A. Gennerich, A. P. Carter, S. L. Reck-Peterson, and R. D. Vale. Force-induced bidirectional stepping of cytoplasmic dynein. *Cell*, 131:952–965, 2007.
- [169] V. Ananthanarayanan, M. Schattat, S. K. Vogel, A. Krull, N. Pavin, and I. M. Tolić-Nørrelykke. Dynein motion switches from diffusive to directed upon cortical anchoring. *Cell*, 153:1526–1536, 2013.

-
- [170] D. P. Devos, R. Gräf, and M. C. Field. Evolution of the nucleus *Curr. Opin. Cell Biol.*, 28: 8–15, 2014.
- [171] H. Asakawa, H. J. Yang, Y. Hiraoka, and T. Haraguchi. Virtual nuclear envelope breakdown and its regulators in fission yeast meiosis *Front. Cell Dev. Biol.*, 4:5–12, 2016.
- [172] P. Cluzel, A. Lebrun, C. Heller, R. Lavery, J. L. Viovy, D. Chatenay, and F. O. Caron. DNA: an extensible molecule. *Science*, 271:792–794, 1996.
- [173] S. Manneville, P. Cluzel, J. Viovy, D. Chatenay, and F. Caron. Evidence for the universal scaling behaviour of a freely relaxing DNA molecule. *Europhys. Lett.*, 36:413–418, 1996.
- [174] C. Labbé and H. Lacoïn. Cutoff phenomenon for the asymmetric simple exclusion process and the biased card shuffling. arXiv:1610.07383 (2016).
- [175] D. T. Gillespie. A general method for numerically simulating the stochastic time evolution of coupled chemical reactions. *J. Comput. Phys.*, 22:403–434, 1976.
- [176] V. Linetsky. On the transition densities for reflected diffusions. *Adv. Appl. Probab.*, 37:435–460, 2005.

Versicherung

Hiermit versichere ich, dass ich die vorliegende Arbeit ohne unzulässige Hilfe Dritter und ohne Benutzung anderer als der angegebenen Hilfsmittel angefertigt habe; die aus fremden Quellen direkt oder indirekt übernommenen Gedanken sind als solche kenntlich gemacht. Die Arbeit wurde bisher weder im Inland noch im Ausland in gleicher oder ähnlicher Form einer anderen Prüfungsbehörde vorgelegt.

Diese Arbeit wurde unter der wissenschaftlichen Betreuung durch Prof. Dr. Frank Jülicher und Dr. Vasily Zaburdaev am Max-Planck-Institut für Physik komplexer Systeme in Dresden angefertigt.

Ich erkläre hiermit, dass keine früheren erfolglosen Promotionsverfahren stattgefunden haben. Ich erkenne die Promotionsordnung der Fakultät für Mathematik und Naturwissenschaften der Technische Universität Dresden an.

.....

Dresden, der 29. September 2017, Wenwen Huang